KUNGL TEKNISKA HÖGSKOLAN

ISSN 1403-1701 Kärnkraftsäkerhet 8
TRITA EKS.Avhandling
ISRN KTH/NPS/CSC-0011-SE

INVESTIGATIONS ON MELT SPREADING AND COOLABILITY IN A LWR SEVERE ACCIDENT

Doctoral Thesis

by

Maxim J. Konovalikhin

November, 2001

Royal Institute of Technology
Stockholm, Sweden

KUNGL TEKNISKA HÖGSKOLAN
Royal Institute of Technology
Ecole Royale Polytechnique
Kgl. Technische Hochschule

Postadress:	S-100 44 STOCKHOLM
	Drottning Kristinas väg. 33A
Telephone:	08-790 9251 (National)
	+46 8-790 9251 (International)
Fax:	08-790 9197 (National)
	+46 8-790 9197 (International)
URL:	http://www.egi.kth.se/nps/
Email:	maxim@ne.kth.se

Royal Institute of Technology
100 44 STOCKHOLM
May 2001

Abstract

Severe accidents in light water reactors have been the focal point of the nuclear reactor safety research after the two well known accidents: TMI-2 (USA, 1979) and Chernobyl (USSR, 1986). In the current experiments on the safety of a nuclear power plant (NPP) design, specific attention has to be paid to the consequences of hypothetical severe accident management (SAM) strategies and the new designs have incorporated new design measures (e.g. core catchers) for management of such accidents. The safety margin provided by such accident management strategies and the new design measures have to be, at a minimum, conceptually evaluated. At the same time, it is important to ascertain that the additional measures and accident management are within an envelope which does not drastically reduce the economic competitiveness of the proposed new designs. The ex-vessel core melt spreading, cooling and stabilization is proposed for the European Pressurized Reactor (EPR) plant containment design. Clearly, in the postulated event of a severe accident, the retention and coolability of the decay-heated core debris is essential so that the containment integrity is maintained and the risk of radioactivity releases is eliminated.

The focus of this thesis research is on the assessment of the core melt spreading characteristics and its coolability. The research approach is to perform experiments with various simulant materials, at different scales, different conditions and with variation of controlling parameters affecting spreading and coolability processes. Complementing the experiments and with the insights gained from the experiments the processes are analyzed at different level of detail and complexity in order to understand the physics, to rationalize experimental results and to develop and validate models.

In the first chapter, after a brief introduction, a review of the status of the knowledge of relevant physical phenomena is performed. Additionaly, a review

of previous and current experimental projects is conducted, and major findings are outlined.

The first part of the second chapter deals with a selected review of experiments, methodologies and analyses on melt spreading process in order to identify and systemize the phenomena and parameters of importance.

The second part of the second chapter describes an innovative scaling rationale for melt spreading with solidification, developed at the Royal Institute of Technology. First, the rationale and scaling methodology for one-dimensional spreading process was developed. Later, the method was extended to cover melt spreading in a two-dimensional channel with a fixed opening angle. Finally, the analysis method was advanced to analyze melt spreading into an open spreading area.

The scaling method was then employed to analyze experimental data obtained from simulant and prototypic material melt spreading experiments. The results of those analyses can be seen in the third part of the second chapter. They allowed determination of constants and verification of assumptions utilized in deriving length and time scales. With this, the scaling rationale was found to possess predictive capability and, therefore, has been proposed to serve as a model for the quantification of melt spreading characteristics. Further, extensive validation of the model as a superior and predictive assessement method. This part also deals with the experimental investigations of the melt spreading phenomena performed at RIT. Three test series were conducted with low, intermediate and high temperature melts under different experimental conditions. The presence of coolant (water) in 'wet' spreading experiments was found to significantly affect the shape of the debris. The increase in viscosity with non-eutectic binary salt mixtures ($NaNO_3 - KNO_3$) was found to decrease the final spreading area compare to that for the eutectics. Binary oxide mixture ($CaO - B_2O_3$) was employed as melt simulant in one- and two-dimensional high temperature spreading tests, which were performed in the SPREAD experimental facility.

The last part of the second chapter presents the results of the assessement of core melt spreading characteristics in the EPR melt retention device. Results of the assessement employing three assumptions (one-dimensional inviscid, one-dimensional viscid and two-dimensional viscid open channel flow models) are shown in this part. The results indicate the very high efficiency of spreading into

an open area. Even in case, when the melt viscosity becomes large due either to the melt mixing with concrete or to the decrease its temperature, the spreading efficiency remains high. As a result, the core melt is predicted to spread over the whole spreading area provided in the EPR melt retention device.

Experimental and analytical investigations of the ex-vessel melt re-spreading phenomena is the topic of the third chapter. The relevant physical processes are described by a computer code MVITA (Melt Vessel Interactions - Thermal Analysis), which takes into account the dynamics of phase change and natural convection heat transfer inside a decay-heated melt volume surrounded by crusts. An experimental program named RESCO (RE-Spreading and COolability) was conducted using both, eutectic and non-eutectic binary salt mixtures ($NaNO_3 - KNO_3$) as simulant for corium melts. Good agreement between calculated results and the experimental data was obtained.

The fourth chapter of the dissertation is devoted to the problem of ex-vessel debris bed coolability, in particular, coolability and quenching of a particulate corium debris bed by water. A number of experiments were performed in the POMECO (POrous MEdia COolability) facility to measure the dry out heat flux in a self-heated bed. A mathematical model for the description of flow of a compressible fluid (steam) through the volumetrically heated porous bed with particular consideration of the local non-thermal equilibrium was formulated and solved numerically using the split step method. It was shown that an initial thermodynamic perturbation which, if it grows, may lead to the temperature escalation at a specific location in the beds, thereby predicting the location of the dry out heat flux. The model was validated against the data obtained from the POMECO facility. Quenching experiments were also performed in the POMECO facility and an integral model was developed as a prediction tool. This model was validated against the data obtained. An innovative aspect of the particulate debris bed dry out and quenching experiments in the POMECO facility was the introduction of downcomer in the bed which enabled the water overlayer to supply water to the bottom of the debris bed where it would flow co-current with the steam produced. It was found the provision of downcomers enhanced the magnitude of dry out heat flux several times and increased the bed quench rate by one to two orders of magnitude.

Keywords: *light water reactor, severe accident, corium spreading, debris coolability, heat transfer, solidification, remelting, crust break-up, natural convection, phase change, mushy zone, dryout, quenching.*

Preface

Research results, presented in the present thesis, were obtained by the author during the period between 1996 and 2001. The work was performed at the Nuclear Power Safety Division of Royal Institute of Technology (KTH). The results of these research activities have been summarized and described in the following publications:

1. B.R. Sehgal, T.N. Dinh, J.A. Green, **M.J. Konovalikhin**, D. Paladino, W.H. Leung, A.A. Gubaidu-llin, "Experimental Investigation of Melt Spreading in One-Dimensional Channel", RIT/NPS Report EU-CSC-1D1-97, 86p., August, 1997

2. B.R. Sehgal, T.N. Dinh, **M.J. Konovalikhin**, D. Paladino, J.A. Green, V.A. Bui, W.H. Leung, A.A. Gubaidullin, A.T. Dinh, "Experimental Investigations of Melt Spreading and Scaling Analysis", published in JAERI Proceedings "Severe Accident Research in Japan - SARJ-97", Yokohama, Japan, October 6-8, 1997

3. T.N. Dinh, **M.J. Konovalikhin**, D. Paladino, J.A. Green, A. Gubaidulin, B.R. Sehgal, "Experimental Simulation of Core Melt Spreading on a LWR Containment Floor in a Severe Accident", ICONE-6, San Diego, USA, May, !998

4. B.R. Sehgal, T.N. Dinh, **M.J. Konovalikhin**, D. Paladino, A.A. Gubaidullin, "Experimental Investigations on Melt Spreading in One and Two Dimensions", RIT/NPS Report EU-CSC-2D1-98, December, 1998

5. **M.J. Konovalikhin**, T.N. Dinh, B.R. Sehgal, "Experimental Simulation of Core Melt Spreading in Two Dimensions", NURETH-9, San Francisco, USA, October, 1999

6. **M.J. Konovalikhin**, T.N. Dinh, R.R. Nourgaliev, B.R. Sehgal and M. Fischer, ”The Scaling Model of Core Melt Spreading: Validation, Refinement and Reactor Applications”, OECD Workshop on Ex-Vessel Debris Coolability, Karlsruhe, Germany, 15-18 November, 1999

7. Z.L. Yang, **M.J. Konovalikhin**, G.J. Li and B.R. Sehgal, ”Experimental Investigation on Dryout Heat Flux of Particle Debris Bed with a Downcomer”, OECD Workshop on Ex-Vessel Debris Coolability, Karlsruhe, Germany, 15-18 November, 1999

8. B.R Sehgal, Z.L. Yang, T.N. Dinh, R.R. Nourgaliev, V.A. Bui, H. Ó. Haraldsson, H.X. Li, **M. Konovalikhin**, D. Paladino and W.H. Leung ”Investigation on Melt-Structure-Water Interactions (MSWI) during Severe Accidents”, SKI report 99:42, 1999, (ISSN 1104-1374)

9. **M.J. Konovalikhin**, S.A. Theerthan and B.R. Sehgal, ”Experimental Investigation on Re-Spreading Phenomena”, ICONE-8, Baltimore, USA, April, 2000

10. **M.J. Konovalikhin**, Z.L. Yang, M. Amjad and B.R. Sehgal, ”On Dryout Heat Flux of s Particle Debris Bed with a Downcomer”, ICONE-8, Baltimore, USA, April, 2000

11. T.N. Dinh, **M.J. Konovalikhin** and B.R. Sehgal, ”Core Melt Spreading on a Reactor Containment Floor”, Intern J. ”Progress in Nuclear Energy”, Vol. 36, No. 4, Pergamon Press, 2000

12. Z.L. Yang, **M.J. Konovalikhin**, M. Amjad and B.R. Sehgal, ”Enhancement of Dryout Heat Flux in a Particle Debris Bed with a Downcomer”, 5th International Symposium on Heat Transfer, Beijing, China, 2000

13. B.R Sehgal, Z.L. Yang, H.Ó. Haraldsson, R.R. Nourgaliev, **M.J. Konovalikhin**, D. Paladino, A.A. Gubaidullin, G. Kolb and A. Theerthan ”Phenomenological Studies on Melt-Structure-Water Interactions (MSWI) during Severe Accidents”, SKI report 00:31, . 2000, (ISSN 1104-1374)

14. B.R Sehgal, **M.J. Konovalikhin**, I.V. Kazachkov, D. Paladino, A. Theerthan, ”Coolability of Melt Pools and Debris Beds with Bottom Coolant Injection”, The Second Japanese-European Two-Phase Flow Group Meeting, Tsukuba, Japan, September 25-29, 2000

15. **M.J. Konovalikhin** and B.R Sehgal, ”Investigation of Volumetrically Heated Debris Bed Quenching”, ICONE-9, Nice, France, April 8-12, 2001

16. **M.J. Konovalikhin**, I.V. Kazachkov and B.R Sehgal, ”Dryout Heat Flux in a Low Porosity Volumetrically Heated Particle Bed”, 4^{th} International Conference on Multiphase Flows (ICMF-4), New Orleans, LA, USA, May , 2001

17. B.R Sehgal, **M.J. Konovalikhin**, Z.L. Yang, I.V. Kazachkov, M. Amjad, G.J. Li, ”Experimental Investigations on Porous Media Coolability”, RIT report, EU-ECOSTAR1-0110-SE, 2001

18. B.R Sehgal, **M.J. Konovalikhin**, D. Paladino, A. Theerthan, ”Melt Pool and Debris Coolability Experiments and Modeling”, European Two-Phase Flow Meeting, Aveiro, Portugal, June 18-20, 2001

Contents

Nomenclature

Arabic

A	Area, m^2
C_{pm}	Specific heat of melt, J/kg· K
D	Width of the channel, m
g	Acceleration due to gravity, 9.8 m/s^2
G	Flow rate, m^3/s
h	Heat transfer coefficient, $W/(m^2.K)$
H	Height of fluid layer, m
Nu	Nusselt number, $Nu = h \cdot \delta / \kappa$
p	Pressure, Pa
Pr	Prandtl number, $Pr = \nu / \alpha$
Ra	Rayleigh number
Re	Reynolds number, $Re = \rho U \delta / \mu$
q	Volumetric heat generation rate, W/m^3
q_v	Heat flux, W/m^2
U	Velocity, m/s
V	Volume of melt, m^3
t	Time, s
T	Temperature, K
Z	Distance, m
Da	Darcy number, $Da = K / H^2$
Gr	Grasshoff number, $\frac{g \beta \Delta T H^3}{\nu^2}$
Fo	Fourier number, $Fo = a \cdot t / H^2$
H_{fus}	Latent heat of fusion, J/kg
K	permeability coeffcient, m^2
k	thermal conductivity, $W/m \cdot K$
a	thermal diffusivity, m^2/s
R	universal gas constant, $m^3 \cdot Pa/mol \cdot K$

u	horizontal velocity component, m/s
w	vertical velocity component, m/s
x	horizontal coordinate, m
z	vertical coordinate, m
d	diameter, m
G	mass flow rate, kg/s
H_{fg}	heat of vaporization, J/Kg
W	thermal power, W
q"	heat flux, W/m^2

Greek

β	Thermal expansion coefficient, 1/K
δ	Thickness, m
μ	Dynamic viscosity, Pa.s
ν	Kinematic viscosity, m^2/s
ρ	Density, kg/m^3
σ	Surface tension, N/m
τ	Time scale, s
$\mathcal{L}$	Dimensionless length scale, -
$\mathcal{N}$	Viscosity number (dimensionless), -
$\mathcal{T}$	Dimensionless time scale, -
ΔT	Temperature difference, K
α	Porosity

Subscript

cap	capillary
conv	convection, hydrodynamic
dis	discharge
dn	downward
inert	inertia
invis	inviscid
liq	liquid, liquidus
m,melt	melt
mp	melting point
sol	solidus; solidification
sp	spreading, spread
tot	total
up	upward
v, vis	viscous

w	wall, substrate
v	vapor
sol	solid
sat	saturation
p	particle
$over$	overlayer
c	critical

Abreviations

ABB	Asea Brown Boveri
SKI	Svensk Kärnkraft Inspektorate (Swedish Nuclear Inspection)
RIT	Royal Institute of Technology
NPS	Nuclear Power Safety Division
BWR	Boiling Water Reactor
LWR	Light Water Reactor
PWR	Pressurized Water Reactor
EPR	European Pressurized Reactor
NPP	Nuclear Power Plant
RPV	Reactor Pressure Vessel
TMI	Three-Miles-Island Reactor
$MFCI$	Molten Fuel-Coolant Interactions
$MCCI$	Molten Corium-Coolant Interactions
$MVITA$	Melt Vessel Interactions Thermal Analysis
$ECCM$	Effective Conductivity-Convectivity Model

Acknowledgements

First of all I would like to thank my supervisor Professor B.R. Sehgal for providing excellent support and guidance during my graduate studies. A lot of thanks go to my advisor Adj. Associate Professor T.N. Dinh (Nam), for his endless help, stimulation and discussion during my studies. His advice really helped me to find my track towards the subject and supported my professonal growth. Next, I want to thank Dr. J.A. Green (Joe), who was always ready to induldge in fruiful discussions of different ideas and in sharing experience. Valuable comments and discussions with my collegue and office mate Dr. I.V. Kazachkov (Ivan) is greatly acknowledged, he kept on challenging me after Nam moved overseas. I feel lucky to have cooperated with Adj. Assistant Professor R.R. Nourgaliev (Robert) and Dr. V.A. Bui (Anh) on scientific subjects related to this thesis. Thanks also to all other colleagues, past and present, at the RIT/NPS, for making the RIT/NPS such a simulating place to work in: Askar, Aram, Anand, Amjad, Antanas, Gilles, Domenico, Lin, Li, Tuan, Kent, Oskar, Rolandas, Isaac, Conny, Gunnar and Jose.

I want to express my gratitude to people from the Nuclear Power Safety Department of Kurchatov Institute and from Moscow Engineering Physical Institute.

Finally, I would like to thank my family in Russia for their love, support and patience during the last five years.

The work performed in this thesis was financially supported, in the frame of the following projects:

1. *"Experiments on Melt-Structure-Water Interactions during Severe Accidents"* funded by Swedish Nuclear Power Inspectorate (SKI), Swedish

Power Companies Vattenfall, Sydkraft, Forsmark, Finnish Power Company TVO under the auspice of the APRI project;

2. *"Experiments on Melt-Structure-Water Interactions during Severe Accidents"* funded by Finnish Power Companies IVO and TVO and the Finnish National Laboratory VTT;

3. *"Experiments on Melt-Structure-Water Interactions during Severe Accidents"* funded by Swiss Nuclear Power Safety Inspectorate (HSK);

4. *"Experiments on Melt-Structure-Water Interactions during Severe Accidents"* funded by the Nordic joint Nuclear Safety Project NKS;

5. *"Corium Spreading and Coolability (CSC)"* Project funded by European Union (Fourth Framework Programme).

I would like to thank all of my sponsors for the financial support provided.

Summary of Technical Accomplishments and Contributions

	Technical Accomplishments and Contributions	*Chapters Appendices*
I. Melt Spreading		
1	An experimental program named Scaled Simulant Spreading Experiments (S3E) was performed at RIT. Experiments were conducted to investigate the impact of thermal-hydraulic conditions upon the melt spreading behavior. Three major series of experiments, involving dry spreading and spreading under coolant were performed at RIT within the S3E program. Various low and intermediate temperature melt simulants (cerrobend alloy, eutectic and non-eutectic binary salt mixtures ($NaNO_3 - KNO_3$)) were employed as working fluid in one- and two-dimensional melt spreading experiments. Series 3 included ten one- and two-dimensional experiments, in which a high-temperature binary-oxide melt ($CaO - B_2O_3$) was employed as the working fluid. Melt and coolant conditions were varied to provide different spreading regimes. An excellent data base on melt spreading was obtained.	Chapter 2, App. A, App. B

	Technical Accomplishments and Contributions	*Chapters Appendices*
I. Melt Spreading (cont.)		
2	Based on the mass and momentum conservation equations, a square-root relation was established between the dimensionless length scale (representing ratio δ_s/δ_{cap}) and the dimensionless time scale (representing ratio τ_{conv}/τ_{sold}). The square-root law was shown to be valid in both gravity-inertia and gravity-viscous regimes, employing a dimensionless viscosity number, which was analytically derived. The scaling method was then used to predict the spreading distance in one-dimensional high-temperature simulant oxidic melt spreading tests at RIT. Very good agreement between the pre-test (blind) prediction results and the data was obtained. The validation success confirmed assumptions made in deriving the model equations (e.g., η = 0.5) and justified the use of heat transfer correlations employed.	Chapter 2, App. A
3	As extension of the one-dimensional scaling methodology the scaling model for melt spreading into an open area was developed. An analysis of the data base obtained from the RIT two-dimensional simulant-material experiments was performed. It was found that the open-channel flow theory performs best in representing the convection time scale used in the scaling model. Further validation can be performed when new data on core melt spreading into open area becomes available. It was noted that melt spreading into an open area is significantly different from the one-dimensional spreading. As a result, the spread melt thickness for spreading into an open area may decrease by factors of 3 to 10, compared to that for the one-dimensional spreading process.	Chapter 2, App. B

	Technical Accomplishments and Contributions	*Chapters Appendices*
I. Melt Spreading (cont.)		
4	Extensive validation of the RIT method was performed against experimental data from KATS, COMAS, VULCANO and FARO spreading experiments. The method was found to predict, with reasonable accuracy, the spreading distance in one-dimensional spreading channels and spreading area in two-dimensional channels (COMAS EU-4, VULCANO and FARO L-26). It was also found that the spreading in two-dimensional channels bounded by the channel's side walls was essentially one-dimensional spreading. It should be noted that the RIT method was employed to perform pre-test predictions for the COMAS EU-2b melt spreading experiment. Excellent agreement between the pre-test (blind) prediction and the observed spreading distance was obtained.	Chapter 2, App. C
5	The scaling methodology was employed to predict the core melt spreading characteristics in the EPR melt retention device. Although the prototypic situation is of spreading into open area, both the scaling method for spreading into an open area and the scaling method for one-dimensional spreading were employed: the latter to provide the conservative lower bound estimate of the spreading area. The assessment was performed for two base cases: with minimum (case A) and maximum (case B) amount of sacrificial concrete slag added to the oxidic corium before spreading. The results of the assessment of core melt spreading in the EPR melt retention device showed that for the given melt delivery conditions the whole spreading area of the melt retention device can be covered by the melt uniformly with the spread melt thickness of 20 to 35 cm.	Chapter 2, App. C

	Technical Accomplishments and Contributions	*Chapters Appendices*
	II. Re-Spreading Phenomenon	
6	Experimental investigation of melt re-spreading phenomenon were performed employing the binary salt $NaNO_3 - KNO_3$ mixture at both eutectic and non-eutectic compositions. Focus was placed on obtaining data on crust re-melting, failure location, failure area development and the resulting re-spreading of the melt. It was found that the governing mechanism for respreading of a crusted melt volume is crust remelting which is driven by the internal natural circulation due to self-heating. It was found that the flowing melt quickly created a channel in the crust downwards from the original location of crust remelting.	Chapter 3, App. D
6	It was also found that the crust remelting (failure) location was always near the upper end of the vertical crust layer, irrespective of the test conditions. The fusion heat of the melt contributes significantly to the solidification (crust formation) and re-melting time scales such that the non-eutectics remelt faster. Analysis of the experiments was performed with MVITA (Melt Vessel Interactions - Thermal Analysis) code, based on the Effective Convectivity - Conductivity Method (ECCM). Experimental and calculated results are in reasonable agreement with each other.	Chapter 3, App. D

	Technical Accomplishments and Contributions	*Chapters Appendices*
	III. Porous Media Coolability	
7	Experimental and analytical investigations of the coolability of heat-generating porous beds named POMECO (POrous MEdia COolabiliy) were performed. The dryout heat flux as the limiting parameter for the steady state removal of the generated heat by boiling of the coolant was the subject of this investigation. Focus was placed on low porosity, small particle size and relatively large scale debris beds. In the debris bed downcomer(s) of different configurations were built which would channel the water from the water overlayer to the bottom of the bed and develop a two phase natural circulation flow loop, providing greater mass flow rate in the bed. A data base on the enhancement of dryout heat flux by downcomers was obtained, for low porosity uniform and stratified beds with heat addition of up to 1 MW/m^3.	Chapter 4, App. E, App. F
7	A mathematical model for the description of flow of a compressible fluid (steam) through the volumetrically heated porous bed with particular consideration of the local non-thermal equilibrium was formulated and solved numerically using the split step method. It was shown that an initial thermodynamic perturbation, if it grows, will lead to a temperature escalation at a specific location in bed thereby predicting the location of the dry out heat flux. The model was validated against the data obtained from the POMECO facility.	Chapter 4, App. E, App. F,

	Technical Accomplishments and Contributions	*Chapters Appendices*
	III. Porous Media Coolability (cont.)	
8	A number of quenching tests were performed to study experimentally the quenching process in the homogeneous and stratified low porosity particle beds, which were quenched by, both, a water overlayer, and by injection of water from the bottom, delivered through downcomers. It was observed that the water entering from the bottom of the bed dominated the quenching process. Thus the downcomers provided quenching rate one or two orders of magnitudes larger than provided by a water overlayer alone. The analysis of the experiments with a zero-dimensional integral model, which combines parameters of the process, geometry and physical properties was performed. Reasonable agreement was obtained between experimental and calculated results.	Chapter 4, App. G

Chapter 1

Introduction

In the last two decades, many investigations have been performed on the physical nature of the thermal and hydrodynamic phenomena, affecting severe accident progression. The progression of the core melt in LWR severe accidents is characterized by the interactions of the melt with in- and ex-vessel structures (see Figure 1.1).

The ex-vessel core melt stabilization has been proposed by spreading and cooling the melt in the containment of a nuclear power plant containment design. Clearly, the retention and coolability of the decay-heated core debris is very much the focal point in the proposed new and advanced designs so that, in the postulated event of a severe accident, the containment integrity is maintained and the risk of radioactivity releases is eliminated.

For the next generation of nuclear power plants severe accidents have to be taken into account in the design. In the extremely unlikely event of the reactor pressure vessel (RPV) melt-through during a severe accident, measures which stabilize the corium melt within the containment boundary, and, thus, preclude fission product release past this final barrier, need to be addressed. One method for achieving this goal is to allow the melt to spread over a large enough surface area so that only a thin melt layer is formed whose long-term melt coolability may be possible by flooding the melt layer from the top by water (see Figure 1.2).

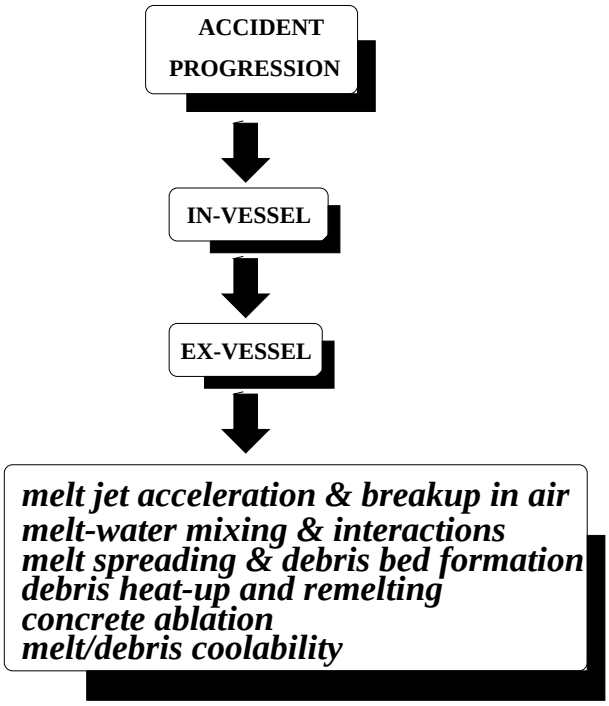

Figure 1.1: Severe accident progression and associated physical processes

1.1 Ex-vessel melt spreading

In the current design option of the European pressurized reactor (EPR), the core melt is assumed to accumulate in a retention cavity, under the reactor pressure vessel, made of special concrete. Interactions between decay-heated core melt and the concrete will result in concrete ablation and rupture of a steel gate at the cavity bottom. Thereafter, the mixture of molten corium and concrete is discharged from the retention crucible, through a short slope, to spread on a large area. The time period required for molten corium-concrete interactions (MCCI) in the intermediate crucible should ensure, relocation from the vessel, and accumulation in the crucible, of a major part of the reactor core melt, before discharge of the melt to the spreading area. In addition, the mixing of the concrete products with the core melt, decreases the melt solidus temperature considerably, thereby reducing the chances of melt freezing before full spreading. Such a strategy is called a one-shot melt release, with very high melt flow rate and sufficient superheat. The time period estimated by the designers of EPR is one hour, which appears to be smaller than what some very recent experiments

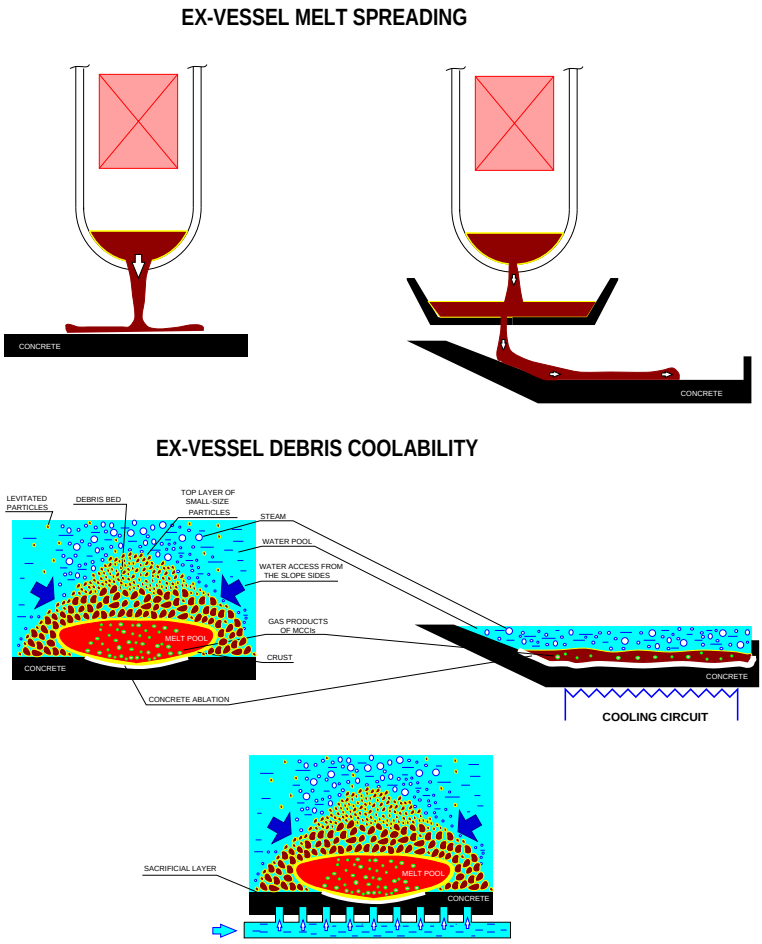

Figure 1.2: Schematic of ex-vessel melt spreading and coolability

(FOREVER, [1]) suggest. According to the worst-case scenario, prior to the core melt discharge, the total mass of homogeneous mixture of metal and oxide melts available for delivery to the spreading channel was found to vary in the range from 40 to 60 m^3. From the reactor safety perspective, it should be noted that the most important parameter for the spreading process is the terminal spread melt thickness and not its dynamics. The former is the measure of the success of spreading as an accident management strategy. In fact, the thickness of the spread core melt should be small enough to ensure the ex-vessel debris coolability.

Spreading of lava, slag flows and liquids on horizontal and inclined surfaces have long been the focus of study in volcanology and in metal, food and chemi-

cal industries. Previously, data from laboratory experiments, from observations in full-scale processes in industry and from volcanic eruptions were employed to quantify the designs of various industrial process and facilities.

Core melt spreading on a reactor containment floor, however, has a specific character, associated with

- the variety of accident scenarios and reactor designs, in which core melt spreading is assumed to occur; and
- the absence of adequate-scale experiments with variation of controlling parameters e.g. melt volume, melt materials and physical properties, melt temperature (superheat), from which observations and data derived could be directly utilized for reactor safety assessments.

The physical process of core melt spreading on a concrete floor may be further complicated by the molten corium-concrete interactions (MCCI), influence of water layer, if it is present, and other factors and phenomena (see Figure 1.3).

Within the reactor safety study programs conducted in USA, Japan, Russia, Germany, France and Sweden, a number of experimental and analytical efforts have been pursued to gain insights into the physics of core melt spreading and to develop models and/or codes which can then be validated and used for prediction and assessment. These activities will be reviewed shortly below. In general, the information available from the experiments and analyses serves as basis for assessment of risk-significant scenarios, and severe accident management schemes in which characteristics of core melt spreading have an important influence.

In general, three different approaches may be employed for purposes of safety assessments:

- Experiments-Based Approach
- Model and Code-Based Approach
- Integrated Approach

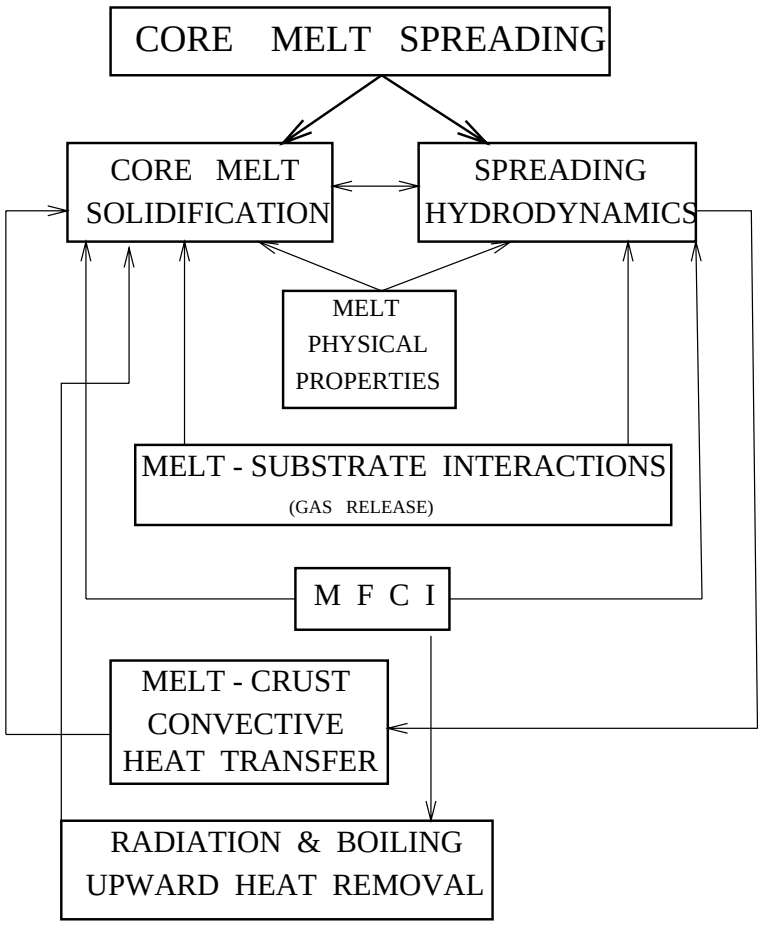

Figure 1.3: Major phenomena and inter-relations under melt spreading

The *experiment-based approach* may first appear simple, but it is limited to specific scenario and accident conditions. More importantly, scaling questions dominate in this approach. For melt spreading, scaling laws have been developed for simple hydrodynamic situations, without thermal interactions and without taking into account phase-change behavior of core melt. In some cases, the experiment-based approach is helpful (see e.g. Theofanous and Yan, 1993, [2]), if appropriate scaling rationale can be derived. Aspects of scaling for melt spreading with solidification will be discussed in Section 2.2.

A number of experiments have been performed to study the phenomenology of core melt spreading on the containment floor (SPREAD, CORINE, BNL, VULCANO, KATS, COMAS, FARO, RIT/S3E). The main objective of these

experiments was to provide data and observations for model development and validation. In particular, experimental programs conducted at JRC (FARO L-26), Siempelkamp (COMAS), RIT (S3E), CEA (VULCANO) and FZK (KATS) are related to verification of the EPR melt retention scheme. Despite their non-prototypicalities (small scales, low temperatures, simulant materials, spreading channel geometry), the experiments provided invaluable insights into the physics of core melt spreading. In the KATS experiments, it was observed that even though the various (uncoated, coated, dry, wet) concrete spreading surfaces are somewhat different from that of ceramic, the spreadability i.e. spreading length is comparable. In addition, the presence of shallow water was found to have no detectable influence on spreading for high pour rate melt discharges. In the COMAS experiments, it was observed that the spreading distances were similar in channels with steel, ceramic and concrete substrate. The oxidic core melt was found to spread very well even when the melt superheat was small (up to 50K in FARO L-26) or even zero or negative (in COMAS 5a).

Most investigators, both experimentalists and theorists, are, however, inclined to direct their work to a model and *code-based approach*. Thus, experiments provide observations and data for model development and code validation. The validated computer codes can then be employed for reactor-scale predictions. Advantages and deficiences of this approach will be discussed later.

The third approach is to perform a reactor safety assessment by integrating database and knowledge base (codes, models) and uncertainty distributions available to date. The integrated approach employs the scenario and phenomenological uncertainties and an appropriate framework to deal with them. PSA (probabilistic safety assessment), ROAAM (risk-oriented accident analysis methodology) (Theofanous, 1997, [3]) and SAPHIRA (severe accident phenomenological integral risk analysis) (Sehgal et. al., 1998, [4]) have been developed and successfully employed to address a number of safety issues.

Clearly, the integrated approach can not result in resolving an issue and in providing a defensible safety assessment until sufficient data and knowledge base on critical phenomena have been accumulated.

The current thesis (Chapter 2) includes six tasks (i) to review related methodology and data base, (ii) to develop an integral scaling methodology for predictions of spreading distances (in 1D) and areas (in 2D), (iii) to perform experiments at RIT with various simulant materials wich varying the controlling pa-

rameters and, thereby, develop a comprehensive data base which would cover the range of parameters needed for prototypical applications, (iv) to validate the integral scaling methodology against data obtained at RIT and other laboratories, (v) to validate the assessment methodology developed at RIT, and (vi) to perform a preliminary assessment of melt spreading characteristics in the EPR melt retention device. The technical approach is based on the validated integral scaling methodology developed, combined with expert judgement and engineering assessment. A quantification of the uncertainties is performed by means of an integral model developed which considers the phenomenological and scenario uncertainties. The melt flow rate, composition and physical properties for the selected scenarios, and geometrical characteristics, are obtained from the specifications provided by Siemens KWU NA-T.

1.2 Ex-vessel debris heat-up and remelting

Ex-vessel progression of a postulated severe accident involves discharge of melt from the reactor pressure vessel (RPV) onto concrete basemat of the containment. The spread-and-stopped melt may or may not cover the whole basemat area. Its layer thickness may be larger than what could be cooled effectively, resulting in it attack on and sinking in the concrete basemat. The competing process is that of melt heat up to fail the crust and the further spreading of the melt mass on the basemat. It has been found that the natural convection of the self-heated melt contained within a crust vessel will be the controlling phenomenon for crust re-melting and break-up (as seen in TMI-2 accident).

Many experimental programs have been performed around the world to study the *melt pool natural convection heat transfer* (e.g. COPO [47], ACOPO [48], UCLA [48], BALI [49], and PASPLAV [50], etc.), *and the structural behavior under high temperatures*. Recently, analytical models and numerical simulation are playing an important role in the development of the knowledge base about the relevant physical processes and phenomena. Basically, there are two reasons for it. First, severe accident physical phenomena involve extremely high temperatures, high pressures, high heat generation rates, etc., which can not be easily reproduced in a laboratory. Second, together with the great improvement in our understanding of a physics associated with severe accident phenomena and the advances of computational methods and the computer power. It is possible to employ mechanistic modeling has been employed

to investigate the complex processes, e.g. melt pool convection heat transfer. Besides mechanistic modeling, integrated models and codes have been developed and applied to study complete processes, e.g. core debris-vessel interactions (MVITA [51] and LOWHEAD [52] codes).

The magnitude of thermal attack from the melt on the bounding crust layer is affected by the thickness of this layer. The thickness of the protective crust layer is largely determined by the initial melt temperature, which is in turn, is governed by the efficiency of the heat removal from the crust outer surface. A crust layer, which bounds core melt pool, maintains a constant-temperature boundary condition for the melt pool. The crust layer may crack when it becomes too thin and unstable. For such conditions, the boundary condition of the melt pool may also change, which can affect both the convection inside and the heat removal from the pool.

The current work (Chapter 3) summarizes results of experiments and modeling efforts, directed to describe the various processes of melt-crust interactions, occuring during the severe accident progression in LWRs. This scenario has been analyzed with the use of the MVITA modeling approach.

1.3 Ex-vessel debris bed coolability

Ex-vessel debris bed could form as a result of melt deposition on the containment floor after discharge from the reactor vessel. If the containment is dry, the melt could reach it without significant change in temperature. When the containment is filled with water (as a result of the severe accident management procedure, adopted by the ABB BWRs, for instance), the melt can partly or fully fragment before reaching the containment floor, the melt temperature could decrease significantly during the melt-water interactions, and, as a result, a quenched particulate debris bed may form (see Figure 1.4).

The porosity of the debris bed formed is defined by the size distribution of the debris fragments. Coolability of such a particulate debris bed depends on the competing processes of decay heat generation and cooling. Cooling of the debris bed by water is quite efficient and, for a porous debris bed, water ingress into the porous structure of the debris bed may intensify debris cooling. If cooling is insufficient, the debris bed can heat up and remelt, which leads to the

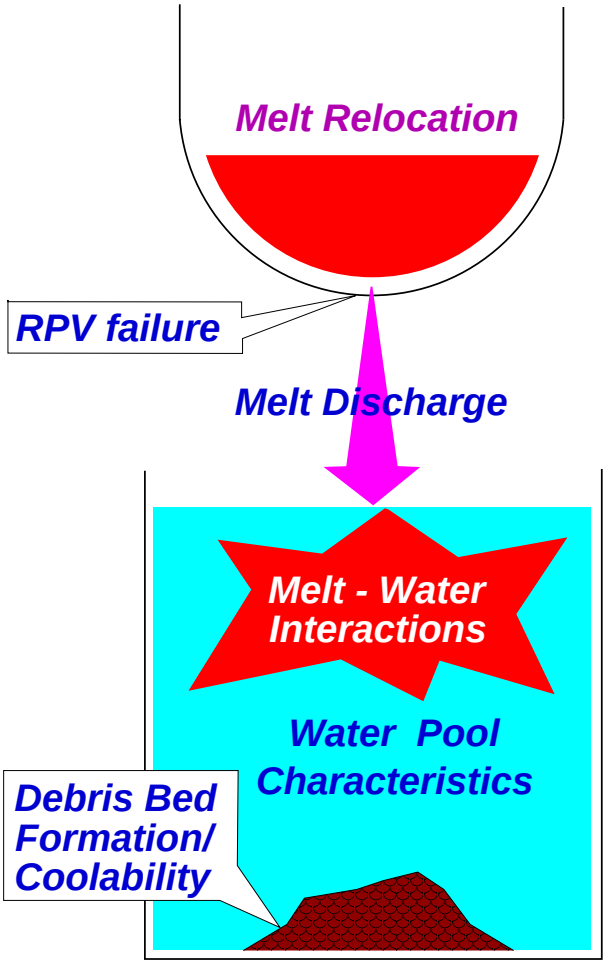

Figure 1.4: Conceptual illustration of the ex-vessel melt discharge and debris bed formation.

formation of a core melt pool on the containment floor.

Most uncertainties associated with the assessement of ex-vessel debris coolability are related to the unknown form, composition, and porosity of the initial debris bed, which are defined from the previous stages of accident progression (ex-vessel melt discharge, possible melt-water interactions, melt spreading). The melt-water interaction scenario will, most probably, produce a stratified bed, quite akin to that found in the FARO tests [63]. The small size particles will be lifted, by the steam produced, into the containment atmosphere and will later on deposit as a dense layer on top. The long-term coolability of an ex-

vessel debris bed is determined by the cooling condition around the bed. Moreover, more active way to achieve debris coolability may also be provided by top or bottom flooding and quenching of the debris bed water. The possibility of debris cooling by top flooding has been sdudied in the ACE and MACE experiments [61],[55], where it was found that cooling with a water overlayer may not be efficient for a thick debris layer, since a tough crust formed on the upper surface of the debris bed may restrict the access of the water from overlayer to the melt. Results of COMET-H experiments [82] showed that the bottom injection is an efficient mechanism providing long-term debris coolability. A similar approach was proposed by Becker [83]. Downcomer(s) built in the debris bed which would channel the water from the water overlayer to the bottom of the bed and develop a two phase natural circulation flow loop, providing greater mass flow rate in the bed.

The issue of debris bed coolability is addressed in this work (Chapter 4) where the processes of dryout heat flux in the volumetrically heated porous beds and quenching, with and without downcomers, are investigated analytically and experimentally.

1.4 Present Work

The severe accident issues considered in this dissertation form a logical sequence of melt progression investigation. The thesis consists of three technical chapters. The first one summarizes the development of integral scaling method for the assessement of melt spreading process and its validation against the experimental data. In the second technical chapter, an experimental investigation of re-spreading phenomenon is described. MVITA (Melt Vessel Interactions - Thermal Analysis) code was employed to simulate crust formation in melt pool, its break-up in remelting regime and to investigate the effect of different physical parameters on these processes.

The third chapter deals with porous media coolability, dryout heat flux and quenching process. The effect of different porosities, particle sizes and bed stratification are investigated experimentally. In particular, an innovative aspect of the experiments is the introduction of downcomers in the particulate debris to deliver water from the water overlayer to the bottom of the bed; thereby water addition to the bed from the bottom. The enhancement of dry out heat flux and

the rate of quenching were measured. The model of steam flowing through the volumetrically-heated porous media is developed and employed for analysis of temperature distribution in the porous beds and detection of dryout location. The quenching data base is analyzed by an one-dimensional integral model based on consideration of hydrodynamic flooding due to steam formation. The analysis applies for both the cases of only top flooding, and of flooding from the top and bottom by the water delivered by downcomers to the bottom.

Chapter 2

Core Melt Spreading on a Reactor Containment Floor

2.1 Introduction

2.1.1 Physical picture of core melt spreading

Spreading regimes

In this study, we consider melt spreading at macroscopic scale, i.e. liquid thicknesses larger than few thousand angströms (Leger and Joanny, 1992 [7]). In such a case, the spreading is almost independent of the wettability of the solid surface and can be described as a hydrodynamic process. Surface tension has a role in the spreading process for very low velocities.

Classical fluid dynamics and experimental observations provide a relatively clear and simple physical picture of hydrodynamic core melt spreading. Core melt may spread on a given surface until the process is terminated by melt solidification.

From the hydrodynamic point of view, the spreading is governed by gravity, inertia and viscosity. Spreading may be categorized into two distinct regimes,

namely

- gravity-inertia
- gravity-viscous

In the latter regime, viscosity plays a dominant role, while in the former, influence of the melt viscosity may be neglected. Equations of motion (Navier-Stokes equations) written for free surface flows can be employed to describe hydrodynamics of liquid spreading.

Phenomenological considerations

Fluid spreading was investigated experimentally and theoretically for cases where inertial effects may be neglected (Shikhmurzaev, 1991 [8], Kalliadasis and Chang, 1996 [9]). In general, at the end of the spreading process liquids form a thin film whose inertial effects are small and where the thickness is much smaller than the typical length scale for the variation of the velocity along the solid surface. The description of hydrodynamic motions can then be considerably simplified by using the so-called lubrication approximation (see e.g. Leger and Joanny, 1992, [7]) or numerical methods (Rahman et al., 1991 [10]).

The physical processes in the corium melt spreading applications (Weisshäupl and Bittermann, 1995 [11], Alsmeyer et al., 1995 [12], Cognet et al., 1997 [13]) motivating this study are more complex, since both gravity-inertia regime and gravity-viscous regime (Ehrhard, 1996 [15]) are involved. Moreover, solidification of liquid (melt) is another process which significantly affects the spreading dynamics (Greene et al., 1988 [16], Moody, 1989 [17], Fink and Griffiths, 1990 [18]).

The strength of the crust (solidified melt) was found to be important for describing the evolution or extrusion of viscous or plastic fluid, for example, in a magma eruption (Griffiths and Fink, 1993 [19]). We should, however, note that, at the current stage, we are not particularly interested in extended spreading typical for lava flows in a volcanic eruption event. As a result, the effects of crust mechanical strength and instability will not be considered.

Table 2.1: Classification of phenomena related to the melt spreading process.

Phenomena	Dry Spreading	Spreading under Water	
-	-	Shallow water	Deep Water
Wettability	Not considered, film thickness $\delta >> 10$ Å		
Hydrodynamics	From Gravity-Viscous to Gravity-Inertia		
Solidification	Phase change of multi-component melts		
Melt stratification	Scenario- and design-dependent		
Crust instability	Typical for lava flows		
Chemical augmentation	Significant for metal-rich melts		
Decay heat generation	Yes	Yes	Yes
Radiation heat transfer	Yes	Yes	Yes
Film boiling on upper surface	No	In first stage	Yes
Heat transfer to substratum	Yes	Yes	Yes
Gas percolation/bubbling	Yes	Yes	Yes
MFCI, melt fragmentation	No	Yes	Yes

Various physical phenomenon control the spreading of corium. Besides hydrodynamics phenomena core melt spreading will be influenced by phenomena like: melt solidification, concrete ablation, change of the melt properties due to addition of concrete decomposition products, fragmentation of melt when interacting with coolant, crust formation, porosity and permeability of solidified melt, bubble-induced mixing enhancement, film boiling, liquid melt moving on roughened surface, radiation heat transfer, stratified steam explosion, etc. Table 2.1 lists the relevant phenomena and indicates those that have been incorporated in the experiments performed and the scaling methodology developed in this study. The spreading processes for deep and shallow water layers are separated. Here the shallow water layer is defined as one in which complete evaporation of the water above the spreading melt layer occurs during the spreading process. In such a case, the upward heat transfer regime (from the melt to surrounding medium) changes significantly during the transient spreading process.

Initial conditions and enviromental considerations

The melt spreading dynamics also depends on:

(i) the initial condition of the melt:

- melt superheat
- melt physical properties and their variation with change in temperature and composition (viscosity, phase-change behavior)
- characteristics of melt supply (melt release modes and rate)
- influence of melt water interaction prior to spreading

(ii) the conditions of the floor and substrate:

- dry or wet floor
- substrate materials (ceramics, cast iron, concrete) and their properties (heat of fusion, gas generation rate etc.)
- cooling mechanisms in the substrate
- if wet floor: water height, water subcooling.

(iii) the spreading section geometry:

- length, width and form of the spreading channel (1D) and the spreading area (2D channel with fixed opening angle, 2D open angle).
- surface inclination
- melt release location (on one edge or in middle of the 1D or 2D spreading section.

In fact, different conditions of melt spreading are realized in different containment designs (EPR, ABB-Atom BWR, Mark-1 GE-BWR) and in different concepts for severe accident management.

Governing mechanisms

To summarize, two major phenomena govern the spreading processes under our consideration, viz.:

- (i) hydrodynamic motion of the spreading liquid (melt);
- (ii) solidification of melt during the spreading process.

The first process is affected by the gravitational, inertial, viscous and surface forces. When spreading of melt in another (lighter) liquid coolant, molten fuel-coolant interactions may influence the hydrodynamics spreading.

The second phenomenon is affected by heat transfer from the melt to surrounding media, i.e. downward $q"_{dn}$ and upward $q"_{up}$ heat removal rates, internal heat generation rate q_{vol} and the phase change behavior of the melt.

2.1.2 Review of melt spreading experiments

Past and current experimental programs

The objectives of the past and the current experimental programs on melt spreading are to obtain insights into the physics of the process and to provide a data base which is needed for validation of the melt-spreading models. The number of experiments is not too large, see Table 2.2. Relevant observations and data sets were obtained from BNL experiments (Green et al. 1988, [16]), SPREAD experiments (Suzuki et al., 1993, [20]), CORINE experiments (Veteau, 1994 [21]), and more recently from the experimental research programs VULCANO (Cognet and Bouchter, 1994 [22]), KATZ (Fieg et al., 1996, [23]), COMAS (Steinwarz, 1997, [24]), JRC Ispra (Magallon, 1997, [25])), RIT/S3E (Sehgal et al., 1997, [5]). Low to high temperature experiments have been performed, using both simulant and prototypic core melts as working fluids.

BNL experiments: observations and major findings

The BNL experiments were performed by Green et al. (1988) [16] in Brookhaven National Laboratory, using metallic lead as melt material. Both dry- and wet-spreading small-scale experiments were conducted to investigate the extent to which core melt may be expected to spread under gravity forces in a BWR dry-well geometry (Green et al., 1988 [16]). Results of these experiments showed that the initial melt superheat and the water-layer height, in the case of wet spreading, are the important parameters, which determine the spreading regime. As a result, total melt mass was defined as of no importance. An empirical approach was undertaken to characterize five distinct regimes of melt spreading,

Table 2.2: Experimental studies of melt spreading.

Facility	Ref.	Country	Geometry	Melt	Temperature	Others
BNL	[16]	USA	2D area	Pb	low	dry, wet
SPREAD	[20]	Japan	1D, 2D area	thermite	high	dry
CORINE	[21]	France	2D--channel	simulants	low	dry, wet
VULCANO	[22]	France	2D-channel	corium	high	dry
KATS	[23]	Germany	1D	thermite	high	dry, wet
COMAS	[24]	Germany	1D, 2D-channel	corium	high	dry
ISPRA	[25]	EU JRC	2D-channel	corium	high	dry
S3E	[5]	Sweden	1D, 2D area	simulants	low-to-high	dry, wet

ranging from hydrodynamically-limited to heat transfer-limited.

Spreading under shallow water was found to be somewhat intermediate between the case of dry-surface spreading and the case of melt spreading into a deep water pool. In particular, after an initial period complete vaporization of the water layer above the spread melt area leads to change in heat transfer regime, with significantly lower heat removal rates in the second period.

Although largely limited to melt spreading in a coolant, insights gained from these experiments were useful. For the first time, regimes limited by heat transfer and hydrodynamic were identified.

The data and the correlation based on BNL experiments are specific to the scenario of melt release (jet form) in a BWR plant. Also, the experimental scale of these tests was very small.

SPREAD experiments: observations and major findings

The SPREAD experiments were, perhaps, the first program in which high-temperature (thermite) melt was employed for spreading tests (Suzuki, 1993 [20]). Experiments were performed both, for steel one-dimensional spreading on a concrete-substrate channel and for spreading into an open area. No scaling rationale was developed or discussed.

Analysis of experimental results led to the suggestion that about 55% of heat of fusion needs to be removed from the melt (i.e. containing 55% solid fraction) to stop the spreading process. Based on a limited number of experiments, it was also suggested that melt seems to spread into an open area within a fixed angle, namely 130^o. The first finding has been confirmed by the experiments and analyses performed at the Royal Institute of Technology. The second finding was however not confirmed in the RIT experiments, which show that spreading angle is rather a function of melt flow rate and melt superheat.

CORINE experiments: observations and major findings

The CORINE experiments were performed at CEA/DRN/DTP using low temperature simulant melts flowing along a 7 m long horizontal section (angle 19^o) (Veteau and Wittmaack, 1995 [28]). Three materials were employed as melt simulant: water, glycerol and cerrotru.

From isothermal (water) tests, an analytical solution for symmetric spreading was modified and was found to describe the data obtained for the spreading-front progression. The spreading-front progresses linearly in time for a constant feeding rate. In glycerol spreading tests, the spreading front progression was found to agree well with Huppert's solution (Huppert, 1982 [32]).

The CORINE tests with solidification, using Cerrotru, showed significant effect of the initial fluid temperature. Another test performed with a hot bottom plate which prevented bottom crust formation, exhibited a notably faster leading edge progression, thereby demonstrating the retarding effect of the bottom crust (see Alsmeyer et al., 1995 [12]).

Three tests were conducted when metal melt was spread under water of dif-

ferent depth. An interesting observation was that the mean melt height appears to be close to the height of the water layer.

KATS experiments: observations and major findings

KATS experimental program performed at FZK (Karlsruhe) studied phenomena of melt spreading on a large area where ultimate cooling of the spread melt layer is provided by water from above. Main experimental parameters were melt phase (oxidic and metalic), melt flow rate, substrate condition (dry and wet), and melt superheat.

In the KATS tests (Fieg, 1996 [23]), the oxidic and metallic core melt is simulated by alumina ($\sim$ 150 kg of Al_2O_3) and iron ($\sim$ 150 kg of Fe), generated by the thermite reaction. Because of the large density difference, the two melt components (oxide and iron) separate quickly in the storage container. Through the upper gate of the storage container first a pure oxidic melt, and finally a pure iron melt is released through the lower gate.

The experimental conditions are presented in the table 2.3.

Table 2.3: Experimental conditions of KATS tests

Test	Melt composition	Type of test	Mass (kg)	T_{melt} (^oK)	$D_{channel}$ (m)
KATS 3b	iron	1D, dry	160	2450	0.2
	oxide	1D, dry	140	2450	0.4
KATS 4	iron	1D, wet	160	2450	0.2
	oxide	1D, wet	140	2450	0.4
KATS 5	oxide	1D, dry	140	2450	0.4
KATS 6	iron	1D, dry	160	1970	0.2
KATS 7	iron	1D, dry	160	2450	0.2
	oxide	1D, dry	140	2450	0.4
KATS 8	iron	2D, dry	158	2100	0.08
	oxide	2D, dry	165	2060	0.08
KATS 11,	iron	1D, dry	150	2223	0.15
12, 13	oxide	1D, dry	186	2323	0.25

KATS (dry-spreading) experiments show that the spreading characteristics are different for oxidic and metallic melts, with very high melt superheats as in KATS-5, KATS-6 and KATS-7 experiments. Researchers at FzK stated that the difference observed in oxidic-melt and metal-melt spreading is due to effects of gate opening rather than fluid properties. Initial velocity of the spreading front in KATS-7 test was as low as 0.4m/s, compared to 2-2.5 m/s in KATS-5 and KATS-6 tests. Results of KATS-5, KATS-6 and KATS-7 experiments clearly demonstrate that the melt discharge rate (and propagation velocity V_s of the spreading front) affect on the spreading length L_s (area), and as a result, the average debris-thickness δ_d.

KAST-8 test was performed on a two-dimensional area. The superheat was high and the melt volume was relatively small for the spreading area given. As a result, very high spreading efficiency was achieved, obtaining a very thin terminal spread melt layer.

KATS (wet-spreading) experiments encountered micro steam explosions (with energetics $\sim$ 0.4 kPa.s). It was found that spreading lengths in these cases are shorter than in similar dry-spreading tests. A steam explosion appears to have local character (KATS-4), which does not significantly affect the spreading characteristics. Also, as in KATS-4, only 1 cm water depth was provided, which can be evaporated in short time.

In the test series KATS-9 to KATS-13, the conditions of actual EPR core melt stabilization concept (reactor pit and spreading area covered with sacrificial concrete) were reproduced by adding $\sim$ 10 wt$\%$ SiO_2 to the alumina melt (simulating the admixture of concrete, mixed melt liquidus $\sim$ 1900^{o}C, solidus $\sim$ 1600^{o}C) and by covering the spreading surfaces (except in KATS-12) with concrete.

A series of four tests (see next table) have been performed to study one-dimensional spreading under EPR representative conditions (spreading surface epoxy-coated, dry and wet, and concrete basemat).

Except for the spreading surfaces the tests KATS 11, 12 and 13 were identical. On ceramic (KATS-12) and on uncoated concrete (KATS-13), the melts spread pretty evenly with $\sim$ 11 m and $\sim$ 7 m, length respectively. The smaller spreading length on concrete is probably due to increased heat losses suffered by the melt caused by percolating gas from the concrete erosion. On epoxy-

Test no.	Spreading surface
KATS-10	Concrete, epoxy-coated, 1 mm water
KATS-11	Concrete, epoxy-coated, dry
KATS-12	Ceramic (cordierite), dry
KATS-13	Concrete, uncoated, dry

coated concrete (KATS-10 and -11) a small fraction of the melt (several ten kg) spread, as the first meltfront, with high velocity over large distances > 10 m, whereas the bulk of the melt spread afterwards evenly over ~ 7 m, similar as on uncoated concrete. The first meltfront is probably spreading on a gas film, below the melt, caused by very high gas production during early contact of the melt with the epoxy-coating.

To summarize, although the details of the spreading process on concrete (uncoated, coated, dry, wet) are somewhat different from those on ceramic, the spreadability i.e. spreading length is comparable. In addition, it should be mentioned, that in the wet test (KATS-10) only one minor explosive interaction (involving a few kg of oxide) was observed, which had no detectable influence on spreading for the relatively high melt discharge rate.

VULCANO experiments: observations and major findings

The objective of the VULCANO experimental program is the study of low flowrate (< 1 l/s) dry spreading of core melt (Cognet, 1998 [14]). Before performing the experiment, employing UO_2, several pre-tests were needed to tune the VULCANO furnace parameters in order to control low flowrates (< 1 l/s) of oxide melts including silica without freezing.

Six pre-tests were successfully performed (Cognet, 1998 [14]). Information was obtained on the behavior of complex mixtures including refractory oxides and in one case (VE-06) iron metal. In the VE-06 test it was found that when iron represents a low percentage ($\sim 5\%$) of the mixture, it is transported by the oxidic phase. Post-test analyses revealed that no segregation occurred and iron droplets of various size were distributed throughout the spread melt.

Visual results indicate that the spreading process was not terminated by a

crust formation at the front. An explanation has been proposed, based on formation of solid particles (dendrites or globules) throughout the fluid which increases the melt viscosity. This mechanism is characteristic of melt having a large difference between the solidus and liquidus temperatures. Physico-chemical interaction between melt and the refractory substratum (zirconia bricks) was observed for about 5 mm depth in the upstream area.

The first spreading experiment with prototypical material (VULCANO VE-U1) was performed on December 2, 1997. Melt composition (45$\%_w$ UO_2, 20$\%_w$ ZrO_2, 20$\%_w$ SiO_2, 13$\%_w$ Fe_3O_4, 2$\%_w$ Fe_2O_3) is supposed to be characteristic of corium discharge from the reactor pit after ablation of the sacrificial gate (EPR configuration). All the measurement devices worked properly, so, after post-test analyses, this experiment should provide results for code validation. In this experiment, unlike pre-tests, spreading was quite efficient, hence, final spreading length was 1.2 m inducing an average spread melt thickness between 2 and 3 cm.

After cooling, spread corium exhibited high porosity due mainly to a large void layer embedded between two corium layers of about 1 cm thickness. Moreover, these two layers incorporated many cavities, those of the bottom layer were vertically elongated while those of the upper layer were essentially spherical. As for pre-tests, the phenomena which stops melt progression is not, up to now, clearly identified. In addition, there is no explanation of the high porosity which seems too large to be only due to the melt shrinkage on cooling(Cognet, 1998 [14]).

On October 22 1998, the VULCANO VE-U3 test was performed. The objective of this test was to compare the spreading and solidification of a corium melt containing a large fraction of refractory oxide against the results observed in the VE-U1 test, in which the corium melt incorporated the highest expected silica content after reactor pit gate meltthrough in EPR configuration (Cognet, 1998, [14]).

In VE-U3, the melt contained 60$\%_w$ UO_2 + 25$\%_w$ ZrO_2 + 8$\%_w$ SiO_2 + 7$\%_w$ Fe_xO_y. Although the liquidus temperature (2520^{o}K estimated by the GEMINI computer code) of this melt was higher than that of the VE-U1 melt (2250^{o}K), the solidus-liquidus temperature range was kept at the same order of magnitude (about 900^{o}K).

At the entrance of the test section, the melt temperature was only 2370^{o}K, certainly below the liquidus temperature, inducing a viscosity which limited spreading. A creeping motion of the front was observed while the melt continued to flow. The final spreading length was roughly 37 cm and the melt thickness varied from 2 cm at the front up to 7 or 8 cm in the back. As in the VE-U1 test, very clear folds formed at the surface during spreading (Cognet, 1998, [14]).

Table 2.4: Experimental conditions of VULCANO tests

Test	Type of test	Mass (kg)	T_{melt} (^{o}K)	Melt entrance width
VE-U1	2D	47	2200	0.08
VE-U3	2D	27	2370	0.08

COMAS experiments: observations and major findings

Within the COMAS experimental project performed at Siempelkamp (Germany) representative experimental investigations on the spreading behaviour of prototypic corium were conducted to provide a realistic technical basis for the development of the EPR core catcher. Main emphasis is placed on the realization of prototypic corium compositions, realistic temperature levels and large spreading masses up to 3 tones. Various substrata (concrete, ceramics and cast iron) have been selected in order to cover a broad range of material characteristics (Steinwarz, 1997).

The experimental conditions of COMAS tests are shown in the following table.

In all one-dimensional tests the channel width was 0.4 m. In COMAS 2D EU-4 test the melt entrance width was also 0.4 m. The COMAS 0, COMAS 1, COMAS R did not give results because of technical difficulties associated with core melt pouring into chills. The COMAS 5, COMAS EU-2, COMAS EU-2a were also stopped prematurily because of leakage in the melt-generation furnace In the COMAS EU-1 and EU-2 tests, core melt spread until the end of the spreading course and reflected back. The COMAS 5a, 6 and EU-1 tests

Table 2.5: Experimental conditions of COMAS tests

Test	Melt composition	Type of test	Mass (kg)	T_{melt} (^oK)
COMAS 0	Corium R	1D	1650	2323
COMAS 1	Corium R	1D	1700	2273
COMAS R	Corium R	1D	1900	2353
COMAS 5	Corium R	1D	2700	2403
COMAS 5a	Corium R	1D	1000	2173
COMAS 6	Iron	1D	530	1923
PRETEST EU-1	Iron	1D	350	2253
PRETEST EU-2	Iron	1D	560	2173
COMAS EU-1	Corium R	1D	1030	2023
COMAS EU-2	Iron+Corium R	1D	1340	2253
COMAS EU-2a	Corium R	1D	1880	2423
COMAS EU-4	Corium R	2D	1920	2323

were concurrently conducted on three substrate courses (concrete, ceramic and cast iron).

The COMAS (dry-spreading) experiments indicate that dry spreading is essentially independent of the substrate materials (concrete, ceramic based or cast iron). Indeed, intense gas and vapor release was observed in the case of concrete, but the spreading velocity and spreading length were not significantly affected.

FARO-S experiments: observations and major findings

The first spreading experiment (FARO L-26) with prototypical material (typical composition of corium discharge from the RPV (80% UO_2 + 20% ZrO_2) was carried out in the SARCOFAGO vessel. Spreading surface was a steel plate. The spreading channel had opening angle of 17^o, bounded by the channel's side walls. Preliminary results were presented by Morris (1997) [43]. In particular, an infra-red film shows melt progression, crust formation and the hot melt which flows out from beneath the crust. Though, the total mass was large (230

kg), spreading length was not more than 1.1 m resulting in a thickness up to 130 mm. This could be explained by the melt initial temperature being close to the liquidus. The mean flow rate was between 1.6 and 2 l/s. The melt spreading flow appeared to be restricted by the channel side walls.

Pre-test calculations were performed with the CORFLOW computer code and the influence of several parameters was studied: superheat, viscosity and emissivity (Wider, 1997) [44]. However, pre-test calculations predicted a much longer spreading distance than experimentally observed. A post-test calculation performed without superheat gave a result closer to the experimental result.

The CORFLOW code was found capable of handling general aspects of melt release and melt spreading in the FARO test. It was found that the radiation heat losses have a strong influence on the stopping of the melt. Larger melt masses will increase spreading length (or area) but not proportionately. A number of cases were studied, using different formulation for fluid viscosity and freezing models. A change of the superheat by 50K does not have strong effect on the spreading, but if the superheats were very low the corium melt would behave like a Bingham fluid, and spread rather short distances (Wider, 1997) [44].

S3E experiments: observations and major findings

The objective of the spreading experimental program S3E (Scaled Simulant Spreading Experiments) performed at the Laboratory of Nuclear Power Safety at the Royal Institute of Technology (Stockholm, Sweden) was to delineate the effect of material physical properties in different spreading regimes:

- gravity-inertia vs. gravity-viscous;
- dry spreading vs. spreading into a coolant;
- different heat transfer to substrates.

More than 60 experiments were conducted to date, using different pairs of melt/coolant fluid simulants, on different substrates, in one-dimensional channels, in channels with fixed angle and on two-dimensional spreading area. Also,

experiments of melt spreading into another coolant (including volatile ones) were conducted. Effects of melt superheat, melt flow(pour) rate, eutectic vs. non-eutectic and melt volume were investigated.

In 'wet' low-temperature spreading tests (spreading under coolant) it was observed that initial interactions between flowing melt and coolant cause fragmentation of the melt, which cools fast and forms a porous layer of lower density. Subsequent melt flow lifts the porous layer and carries it to a distance determined by the flow rate (inertial forces). Likely, structure of the porous layer depends on temperature difference $T_{melt} - T_{cool}$ and the layer may partly remelt due to heat transfer from the melt, which flows beneath the upper crust layer. It was also observed that the presence of a coolant significantly decreases the spreading velocity, especially in case of very low superheat over the liquidus temperature.

A trend is observed, particularly in wet spreading tests, that the layer thickness decreases towards the spreading leading edge, which is, of course, natural. Partly, it is related to the formation of a porous layer during the initial interactions period discussed above. There is also a small portion of the spread melt layer at the very leading edge which is significantly thinner. Such small portions of melt are of minor significance and do not determine the spreading distance. In general, variations of the spread thickness and uncertainties associated with the leading-edge portion are of minor consequence.

For high-temperature simulant spreading experiments, it was found that the spreading process on the steel substrate occurred smoothly. Instead, the spreading process on the concrete substrate encountered violent interactions between the high-temperature melt and concrete. As the melt front progressed into the concrete channel it was clear that substantial gas generation occurred due to the heating of the concrete. Both unbound and bound water in the concrete was driven out and it was clearly observed in the videotapes that the viscous glassy-like melt had substantial gas bubbles passing through it. It would also appear that combustible gases (CO) were being generated since the upper surface of the melt was seen to be on fire.

Spallation, defined as the breakoff of thin upper layers of the concrete surface as a result of the buildup of vapor pressure due to the evaporation of the free and bound water in the concrete, was seen to occur at several locations along the bottom of the concrete channel during the course of this experiment.

It resulted in significant disturbances of the spreading melt layer and a small amount of the melt was splashed outside the channel.

It was also seen that structure of the spread melt layer on the concrete substrate is affected by gas/steam bubbles in the melt layer and their collapse on the melt surface. Such gas percolation caused formation of a porous melt layer.

Nonetheless, the spreading distances were almost the same in the two spreading tests 3MDC-Ox-1 (concrete-substrate) and 3MDS-Ox-1 (steel-substrate). Probably, it is because the termination of the spreading process is largely governed by the solidification of the melt at its leading edge rather than on the processes occurring behind the spreading edge.

In 'wet' high-temperature simulant spreading experiments on a steel-substrate channel, melt-water interactions resulted in a porous layer residing on top of another non-porous layer. It indicated significant melt fragmentation and solidification upon melt release into water. Boiling on upper surface of the spread melt would also render formation of porous structure. The bottom layer might have resulted from later melt release which did not come into contact with water but protected by the upper layer of hot debris. The spreading distance was found shorter in melt spreading into water than in similar dry-spreading tests. This is natural because of higher heat removal rate in the wet-spreading which hastened melt solidification. However, no other differences or curious observations were found in experiments of melt spreading into coolant.

Significant new observations and important insights were gained from experiments of melt spreading into channels with fixed opening angle and experiments of melt spreading into an open area.

For cases with small (fixed) included angle of a 2D-channel, low melt flow rate and low melt superheat, spreading is restricted by the channel side walls. In these cases, the spreading behavior is essentially one dimensional as are the spreading characteristics. For cases with large (fixed) included angle of a 2D channel and for relatively large melt flow rate for a certain period, spreading is not restricted by the channel side walls. For these conditions, the spreading process is similar to spreading into an open area.

Melt spreading into an open area is significantly different from the one-dimensional spreading. As melt spreads in all directions, the hydrodynamic

spreading time scale is remarkably reduced, and the spreading efficiency is similarly enhanced. In the initial period of melt discharge into an open area the physical process of 2D spreading is similar to the flow after a dam-break. Later on, (after formation of a bottom crust layer) the spreading flow resembles the flow over a dam. A solid crust is formed on the substrate as the melt spreading occurs. It should be noted that the crust thickness increases with the distance from the entrance into the 2D section. As a result, melt accumulation may occur not far from the entrance region.

In general, it is found that 2D spreading is a very effective means of achieving large spreading area, provided the melt flow rate is high, the melt viscosity is low, and there is a substantial difference between the melt liquidus and solidus temperatures.

Summary on conclusions drawn for experiments and needs for further experiments

Several major conclusions were drawn from the preceding review of melt spreading experiments.

First, there is a sizeable database on melt spreading in channels. Very few experiments were conducted on spreading into an open area, which is of interest to reactor melt spreading process.

Second, in most cases, experiments were performed, to provide data and observations for model development and code validation. However, no strict and proper scaling arguments were developed.

Third, various melt simulants were employed. Only in FARO L-26 test, real corium was utilized. However, for reactor application, the corium melt could be significantly different due to mixing with decomposition and melting products of concrete in the reactor intermediate crucible.

Results and observations from BNL, SPREAD and CORINE programs, as well as from the more recent experiments (KATS, VULCANO, COMAS, FARO, S3E) will be further analyzed later (section 2.3) in the light of the assessment methodology developed in section 2.2.

Currently, there is a lack of observations and data on melt spreading in a 2D spreading area. Although important insights were gained from S3E experiments at RIT (Sweden), confirmatory experiments with higher temperature melts are desirable.

2.1.3 Review of melt spreading analyses and simulations

Scope of the review

There are a large number of papers devoted to various theoretical aspects of liquid spreading. Most of them are however focused on contact angle, wetting and spreading properties. Other articles are directed to simulating lava flows, where thermal erosion, formation of flow channel, lava flow morphology in km-scale are considered. In the present work, these aspects will not be further considered and reviewed.

The scope of the following review is to examine reactor-scale and reactor-related prediction potential and capability of various concepts of melt spreading modeling and assessment developed in the past or under development.

Analytical and semi-empirical approaches

It should be noted that all known analytical solutions for liquid spreading are based on various simplification of the Navier-Stokes equations. Namely, the shallow-water approximation or the well-known approximation of lubrication theory are utilized in the one-dimensional spreading and the axisymmetric spreading. The effect of melt solidification is neglected. Even with such simplifications, the hydrodynamic equation is not easy to solve analytically. For some cases with special initial conditions (stated source) and specific behavior of liquid viscosity, the spreading dynamics equation may be solved with a similarity solution. Huppert (Huppert, 1982 [32]) obtained solution for the isothermal spreading of a volume of liquid which increases with time as $q \cdot t^{\alpha}$ ($\alpha \geq 0$), but assuming constant viscosity.

Later, Sakimoto and Zuber (1995) [40] obtained the solution for the axisym-

metric release of a fixed volume of fluid (α = 0) with time-dependent viscosity in the form $\nu = p \cdot t^{\beta}$ ($0 \leq \beta \leq 1$). They also solved the equation of the model, numerically, for the general case of variable viscosity. Practically, the heat transfer and solidification aspects are replaced by an empirically-chosen law for the melt viscosity variation in time. Results obtained helped to explain certain volcanic dome morphologies observed on Venus (Sakimoto and Zuber, 1995 [40]).

More recently, Foit (1997) [41] extended the analytical solution to flows with $\alpha \geq 0$ and $0 \leq \beta < 3\alpha + 1$ in one-dimensional and axisymmetric geometries.

There are some other analytical studies on liquid spreading, whose focus was, however, placed on microscopic flow characteristics and are, therefore, not reviewed here.

Several semi-empirical methods were developed. Based on observations from experiments of molten Pb-Bi alloy spreading in water layers of different heights, Greene et al. (1988) derived a correlation which determines spreading regimes [16]. Primary parameter in the Green's model was the height of water layer. No and Ishii (1991) [42], based on dimensionless analysis groups, estimated characteristic times for molten corium spreading-related processes in Mark-1 BWR containment. Moody and co-workers (1991) [45] developed a theoretical model for spreading, cooling and freezing of molten core debris on a horizontal surface during a postulated severe accident. Time-dependent spreading geometry was predicted, and it was found that corium discharge from a doorway tends to have a spreading angle of about 52 degrees (104^{o}-opening angle) when surface tension is negligible.

A common feature of the semi-empirical models was that they are based on significant assumptions and empirical correlations derived from data and observations from limited number of small-scale and simulant-material experiments. The models and correlations have not been then tested extensively against larger scale experiments at different conditions. Very few applications of such models and correlations to reactor assessments were reported in the literature.

Simplified-to-mechanistic transient-simulation codes

The mainstream of the on-going spreading-related research is to perform more experiments for validation of computer codes, such as CORFLOW, MELT-SPREAD, THEMA and others (see Table 2.6). Unfortunately, most of the codes listed are still in their developmental stage, and their performance codes has not been discussed thoroughly in the literature. It makes it difficult to review, classify and reach consensus on the status of a particular code and the spreading model employed.

In addition, there is confusion about the definition of simplified codes and mechanistic codes. The roots of such confusion are the complex physical processes. Direct numerical simulations to provide mechanistic description of the flow and heat transfer phenomena are not easy. Therefore, even models and codes, defined hereinafter as mechanistic, employ a number of assumptions and simplifications. In simplified codes, the simplifications are significant, while in mechanistic codes, the assumptions are made with respect to some local physical parameter and property, rather than on the integral behavior.

The MELTSPREAD code (Farmer, 1993 [26]) was developed at Argonne National Laboratory (USA) ander EPRI sponsorship and contains detailed models for gravity-driven flow; melt freezing immobilization, and remelting; concrete heatup; decomposition and gas release; concrete melting and ablation; enhancement of heat transfer from the melt to underlying concrete due to sparging gases from concrete decomposition; chemical oxidation of metallic melt constituents; spreading of melt over previously spread material; and two-dimensional heatup of the steel shell of the BWR Mark-1 containment due to forced convection and impingement heat transfer from spreading melt adjacent to the shell.

Currently, validation exercises are being performed for the MELTSPREAD code in several organizations. However, no systematic assessment has been reported. It should be noted that most of spreading experiments have been performed with simulant materials on steel substrate. Few experiments (SPREAD, COMAS, S3E) were conducted on concrete substrate. MCCIs were observed in the latter. However, no significant effect of MCCIs on melt spreading distance was reported. In any case, aspects of MCCI chemistry and thermal hydraulics during the spreading process become important if the spreading process is of long duration.

Simplified codes, such as THEMA and CROCO codes and SPREAD, presented by Suzuki (1993) [20], are based on phenomenological models and lumped-parameter representation of mass and energy conservation equations. Only limited validation of these models and codes against melt spreading experiments can be found in the literature. No reactor applications using these models and codes have been reported, to the knowledge of the authors at present time.

Table 2.6: Computer code for melt spreading simulation.

Code	Ref.	Country	Model characteristics
CORFLOW *	[39]	Germany	2D - mechanistic
CROCO	[31]	France	simplified (ISPN)
LAVA*	[27]	Japan	2D - Bingham fluid
MELTSPREAD*	[26]	USA	1D - complex physics and chemistry
MECO	[29]	Germany	mechanistic (Ruhr Univ.)
RASPLAV/SPREAD	[30]	Russia	2D - hydrodynamic
SPREAD	[20]	Japan	simplified
THEMA *	[13]	France	phenomenological (CEA/DRN)
Footnote	*	Codes receiving International recognition	

Bolshov and co-workers considered three different approaches to model processes of molten core spreading (Bolshov, 1994 [38]), namely, a) two-dimen sional models based on Navier-Stokes equations in cylindrical geometry, b) simplified quasi-two-dimensional models based on the approximation of thin layer (film flow) and high-viscous (creeping) flow and c) the simples models on the basis of height-averaged description leading to the so-called shallow water approximation.

Example calculations were performed using the first approach. Results were presented for a broken dam problem and for two selected cases of core melt flowing. Assumptions were made on boundary conditions. No validation was however proposed for the models employed for heat transfer, solidification, spreading dynamics and for spreading distance.

Further improvement of the above work was presented in a paper by Popkov and co-workers (1994 [30]), in which features of the RASPLAV/SPREAD code were discussed. The code utilizes the axisymmetric shallow layer approximation. It was shown that the code performs very well in predicting isothermal spreading processes in CORINE experiments (water and glycerol). It was also confirmed that the variation of fluid viscosity does not significantly affect the spreading front propagation, but influence the height of the fluid layer. Information is not available on the code and the model to assess the characteristics of melt spreading with solidification.

The common feature of the mechanistic codes is that the developers first focused their attention on hydrodynamic aspects, including free surface modeling, moving boundary adaptation and numerical diffusion. With the crust formation at the lower surface and upper surface, the friction and heat transfer from the spreading melt flow to to the substrate and enviroment may largely be governed by surface roughness. This is not represented in the models in the mechanistic codes. Phase change is not well treated because of it's complexity. In particular, the melt property variations during phase change affect liquid mobility and they are the dominant phenomena responsible for melt stopping mechanism.

The CORFLOW code was developed by SIEMENS (Germany) (Wittmaack, 1997 [39]). This code treats the hydrodynamics of the melt as an incompressible, viscous Newtonian flow in Eulerian geometry. The temperature calculation includes conduction and convection heat transfer in the fluid and conduction heat transfer in the solid structures below and around the melt flow. The heat transfer between the surface of the melt and the structures above is treated by radiation heat transfer. When the heat losses cause the melt temperature to drop below the liquidus temperature, the melt viscosity increases strongly and the melt eventually comes to rest due to the friction. The crust formed on the top layer of the spreading flow is assumed to float on the melt flow. Currently, 2D simulations have been performed, not including the interaction between the upper crust and the spreading channel's side walls. The halt of the melt spreading is related to the merging of the upper and lower crust layers at the spreading front.

In general, numerical treatment, for spreading flows with solidification, is accompanied by numerical diffusion caused by the treatment of free surfaces, moving boundaries and solidification occurring on interfaces. Other apparent difficulties in the CORFLOW modeling are associated with the assumptions

and methods employed in simulating flow of the mushy melts (in between liquidus and solidus temperatures) and in addressing mechanisms which stop the melt flow spreading further. There are other limitations in representation e.g. of turbulent flow and heat transfer, interactions between the roughened crust surface and the spreading flows and, and the effect of unstable stratification on mixing and heat transfer in the spreading flow due to formation and sinking of higher-density solid crust, etc.

The CORFLOW code has undergone considerable validation through comparison with the analytical isothermal Huppert's solution, through comparison with data from CORINE experiments, and through comparison with some of KATS experiments. Systematic validation and assessment of the CORFLOW code against existing database (including FARO, COMAS, KATS, S3E, VULCANO) are underway in Siemens KWU and in other organizations.

Direct numerical simulations

Methods of direct numerical simulation (DNS) were employed by few groups (Tokyo Institute of Technology in Japan, Royal Institute of Technology in Stockholm) to analyze melt spreading processes. Moving-Particle Semi-implicit (MPS) method and Level-Set Algorithm (LSA) were employed in the above-mentioned groups. However, simulations were performed for very simple cases of hydrodynamic spreading. No significant insights into the physics of melt spreading were gained, since most of simple cases can be effectively analyzed by existing analytical solutions or semi-empirical models.

Some general-purpose CFD codes (STAR-CD, Fluent, Flow-3D) declare that liquid spreading, dam breaking and overflow, water column falling and spreading can be modeled within these codes using VOF (Volume-Of-Fluid) method. The Flow-3D code (Flow Science Inc.) was used to simulate spreading of molten metal melt into a mold and freezing of metal during the spreading process. No validation was however found in the literature for this case.

Generally speaking, DNS requires resolution of the smallest turbulent length and time scales. Moreover, for free and moving surfaces, nodalization should be extremely fine to reduce the effect of numerical diffusion and to ensure accurate description of spreading dynamics. Last, but not least, difficulty is the modeling of phase change, which is associated with melt surface (surface roughness-

induced turbulence generation, solidification front propagation). All these aspects point to very large costs of DNS which is used for real-life applications such as core melt spreading on a containment floor.

In order to effectively employ CFD-type codes, significant simplifications and assumptions have to be made. Additional models should be implemented to represent underlying physics which is not described in coarse-grid simulations. This essentially transfers the DNS and CFD into mechanistic methods with phenomenological models. However, a robust numerical scheme and interface tracking methods have to be employed.

Summary on analyses and simulations and need for further development

It should be noted that analysis, simulation and assessment of melt spreading have attracted significant attention of researchers and engineers in the field of severe accident evaluation and management. Efforts have been initiated in a number of organizations, and a number of methods have been proposed. In general, some significant applications have been reported in the literature. They provided insights into the phenomena from different angles and approaches. Most notably, significant difficulties in modeling were identified.

Unfortunately, at the present stage, none of the efforts have resulted in a reliable prediction method which could be employed in more-or-less straightforward manner to quantify spreading characteristics in a severe accident situation (see Table 2.7).

Futher work in all of the above-reviewed code and models would improve understanding. Likely, future work may achieve a mechanistic method, with a set of reasonable assumptions and validated phenomenological models, to predict reactor-scale melt spreading in severe accident scenarious. However, it appears to us that development of such a method, to be reliable, would need significant investment of time and funds.

Table 2.7: Status of melt spreading analysis and simulation methods.

Approach	Remaining Issue(s)	Prediction Capability
Analytical	Exist only for component models and very simple cases	Limited to specific scenarios (e.g., without solidification)
Semi-empirical	Absence of proper scaling rationale which accounts for effect of properties and geometry	Extrapolation to large scales & other melts not substantiated
Simplified models/codes	Verification of assumptions and validation on large-scale exp.	Very limited (currently, none for 2D)
Mechanistic codes, with phenomeno-logical models	Computational cost (time, memory). Numerical stability & convergence. Sensitive to models and assumptions on phase change, property variation etc.	Not validated for the reactor-assessment purpose
DNS	Simple cases only	None

2.1.4 Review of scaling-related developments

The phenomena involved in the spreading process are complex and there are large uncertainties in describing them. The more important of this phenomena are: heat transfer to concrete, radiation heat transfer, film-boiling heat transfer, solidification of binary oxidic melts, increase uf melt viscosity with decrease in melt temperature. It is also unclear whether the prototypic conditions can be represented in simulant-material and small-scale experiments. Both the effects of material properties and geometry on scaling distortions have to be analyzed in detail in order to warrant the applicability and relevance of the data and observations obtained with simulant material experiments of small scale.

We believe that scaling laws for the spreading phenomena would also allow well-defined and well-focused experimental programs and code/model development and validation.

Table 2.8: Previous scaling-related considerations.

Author(s)	Year	Ref.	Focus	Time & Length Scales
Huppert	1982	[32]	Viscous regime	Yes
Greene et al.	1988	[16]	Water depth	None
Moody	1989	[17]	Heat transfer, q_{che}	τ_{sol}, U (inviscid)
Kazimi	1989	[33]	Heat tr. to concrete	None
Fink & Griffiths	1990	[18]	Morphology	τ_{sol}
No & Ishii	1991	[42]	Integral	Dimensionless groups
Theofanous & Yan	1993	[2]	Transient. Multi-D	Froude number
Veteau et al.	1995	[21]	Geometrical scale	Regime transition
Ehrhard	1996	[15]	Flow regimes	Not explicit

Previously, scaling formalisms were attempted differently in (Huppert, 1982 [32]), (Greene et al., 1988 [16]), (Moody, 1989 [17]), (Kazimi, 1989 [33]), (Fink and Griffiths, 1990 [18]), (Theofanous and Yan, 1993 [2]) and (Ehrhard, 1996 [15]). Huppert (1982) presented analytical solutions for propagation rates in the gravity-viscous regime, for both two-dimensional and axisymmetric spreading [32]. He also performed order-of-magnitude evaluations of forces, based on which he derived the transition time, t_{iv}, at which inertial and viscous forces are comparable in magnitude.. This characteristic time was used by Veteau and Wittmaack (1995) to identify the dominant regime for spreading experiments [28]. Green et al. [16] emphasized the water layer thickness, while neglecting the heat transfer to the bottom. Moody (1989) based his first-order analyses on solidification time scale, which he defined as thermal response time, and on liquid velocity, which he derived from a one-dimensional inviscid analysis [17]. He considered augmentation of decay heat by chemical reactions. Kazimi (1989), instead, emphasized heat losses to the concrete [33]. Fink and Griffiths (1990) focused their analyses on relation between surface morphology and solidification rates, which is important for lava flows [18]. Theofanous and Yan (1993) provided a good review of various concepts and emphasized the transient and multidimensional aspects of spreading. They considered the hydrodynamically controlled spreading and employed the Froude number for scaling purpose [2]. Ehrhard (1996) classified the spreading regimes in term of Reynolds numbers and ratio of liquid thickness to spreading length.

It should be mentioned that No and Ishii (1991) performed a scaling study

on spreading of molten corium in Mark-1 BWR plant. Twenty-nine potentially important phenomena were identified and ranked. Spreading and crust formation were considered as phenomena of high relative importance. Using the concept of open channel flow, two spreading mechanisms were identified: gravitational force-dominant spreading and surface tension-dominant spreading. A large number of dimensionless groups were derived to represent different effects and regimes. Heat transfer was analyzed by considering water-corium-concrete interactions. Two separate steps were modeled: interactions before and after solidification starts. Again, a number of dimensionless groups were derived. Time constants and relative importance of scaling parameters were examined for a selected accident scenario. It was found that time constants related to water-corium-concrete interactions are much shorter than those related to spreading. Unfortunately, a scaling rationale was not developed and no validation was performed.

Generally speaking, none of the previous studies (see Table 2.8) resulted in scaling laws, which could be employed to provide quantitative information for designing of simulant-material and small-scale spreading experiments of interest to reactor applications. Nonetheless, the studies performed in the past, including those cited above, provide the background for the development of the scaling rationale described in section 2.2.

2.1.5 Other phenomena and parameters of interest

Effect of molten corium-concrete interactions (MCCI)

MCCI and related gas release and bubble agitation in the spread melt layer were found not to have a negative effect on melt spreading efficiency. Likely, opposite is applicable: spreading of hot melt on a concrete substrate tends to be longer and to form a more porous layer. Gas bubbles seem to have certain 'lubrication' effect as well as help to destroy or destabilize crust layers formed on the bottom and upper parts of the spreading melt layer.

Effect of molten fuel-coolant interactions (MFCI)

Effect of MFCI on melt spreading may be quite complex, if water is present in the floor. If the melt spreads into a thick layer of water, melt may fragment and solidify faster. Local energetic event may occur (although unlikely for core melt), which however has little impact on melt spreading characteristics. Perhaps, efficient heat removal from melt to water through boiling and radiation is the major concern, since it may hasten melt solidification, strengthen the crust and cause the melt flow to stop.

Effect of melt stratification

Melt stratification may occur if the oxidic and metallic components were well mixed before spreading starts. However, it is more likely that such stratification will occur in the vessel or in the intermediate retention crucible of the EPR prior to melt discharge to the spreading area. Thus, the spreading process includes subsequent spreading of oxidic and metallic melts. Effect of melt stratification during the spreading could therefore be neglected.

2.2 Scaling

2.2.1 Objectives

This section describes an innovative scaling rationale for melt spreading with solidification. The rationale for one-dimensional spreading processes was developed at the Royal Institute of Technology and described in Dinh et al., 1998 [6]. Further, the method is extended to cover melt spreading in a two-dimensional channel, with a fixed opening angle. Finally, the analysis method is extended to the analysis and prediction of melt spreading into an open spreading area.

The scaling method was also employed to analyze the simulant material spreading experiments and compare to the experimental data obtained. This allows determination of constants and verification of assumptions utilized in

deriving length and time scales. With this, the scaling rationale was found to possess predictive capability and therefore can serve as a model for quantification of melt spreading characteristics for prototypic melts, geometries and conditions. Extensive validation of the model was performed (see section 2.3), which demonstrates the reliability and uniqueness of the scaling methodology as an assessment method.

2.2.2 Scaling principles

The need for a scaling methodology was discussed above. We emphasize again that a systematic acquisition and examination of database would only be possible within a frame of a scaling rationale.

In order to develop a scaling methodology, three major principles are maintained.

First, the scaling rationale is based on goal-oriented parameters. In this case, scaling parameters are determined from reactor safety perspectives.

Second, while seeking the simplicity of the scaling equations, it is required to conserve the (potential) effects of simulant-material physical properties on the component phenomena.

Third, equations and correlations, employed in deriving the scaling relations, are transparent and can be separately validated.

It should be noted that the spreading process researches is strongly coupled to the ex-vessel debris long-term coolability issue. The thinner the debris cake or bed, the more probable that it is coolable by water flooding. Thus, from the reactor safety perspective the most important scaling parameter characterizing the spreading process is the *terminal thickness* of the spread melt (debris), δ_{sp}.

2.2.3 Length and time scales

Dimensionless length scale $\mathcal{L}$

Dimensionless length scale of the spreading process with melt solidification is introduced as ratio between the average height of the spread melt δ_{sp} and the capillary thickness δ_{cap}.

$$\mathcal{L} = \frac{\delta_{sp}}{\delta_{cap}} \tag{2.1}$$

Provided no solidification of the liquid, the thickness of the spread liquid is uniform over the terminal spreading area due to the gravitational force. It is known that the spreading continues as long as the force balance at the spreading leading edge is in favor of inertia rather surface tension.

Theoretically, the thickness of the liquid layer δ_{cap} resulting from purely hydrodynamic spreading is determined by the balance between the capillary pressure at the leading edge,

$$p_s = \frac{2\sigma}{r} = \frac{2\sigma}{\delta_{cap}/2} \tag{2.2}$$

and the driving pressure

$$p_g = \rho_m g \delta_{cap} \tag{2.3}$$

Hence,

$$\delta_{cap} = 2\sqrt{\frac{\sigma}{\rho g}} \tag{2.4}$$

Dimensionless time scale $\mathcal{T}$

It was found from the review of physical picture of melt spreading, melt hydrodynamics and melt solidification are two competing phenomena, which determine the efficiency of the spreading process.

Thus, dimensionless time scale can be defined as ratio of competing characteristic times of the hydrodynamic spreading τ_{conv} and melt solidification τ_{sold}.

$$\mathcal{T} = \frac{\tau_{conv}}{\tau_{sold}} \tag{2.5}$$

The hydrodynamic spreading time scale τ_{conv} differs for different hydrodynamic regimes, namely gravity-inertia and gravity-viscous spreading regimes. In the gravity-inertia regime, τ_{conv} can typically be determined as the time period required for liquid (melt) to spread to reach its terminal state (capillary thickness δ_{cap}). Thus, determination of τ_{conv} involves spreading dynamics (spreading velocity U). Detailed discussion on spreading velocity in different regimes is presented in the following sections.

The characteristic solidification time, τ_{sold}, is defined as the time period needed to reduce the melt temperature (enthalpy) to the level that the melt becomes immoveable.

2.2.4 Characteristic velocity U and spreading time scale τ_{conv}

Gravity-inertia regime of liquid spreading

In case the viscous force is small compared to the inertia force, the momentum equation can be re-written in the following form (see e.g. Moody, 1989 [17]).

$$UdU + g \cdot \delta = 0 \tag{2.6}$$

or

$$d(U^2 + 2 \cdot g\delta) = 0 \tag{2.7}$$

For a given melt flow rate $G = U \cdot D \cdot \delta$ (i.e. the continuity equation), one obtain

$$d(U^2 + 2 \cdot g\frac{G}{U \cdot D}) = 0 \tag{2.8}$$

or

$$2U \cdot dU - \frac{1}{U^2}\frac{2 \cdot g \cdot G}{D}dU = 0 \tag{2.9}$$

Finally, the solution for the characteristic velocity U is obtained as follows.

$$U_{inert} = \left(\frac{g \cdot G}{D}\right)^{1/3} \tag{2.10}$$

Note that this equation differs from the solution by Moody (1989) [17] by a constant.

For one-dimensional spreading in a channel, the spreading time scale, τ_{conv}, for the gravity-inertia spreading process can be determined as follows.

$$\tau_{conv} = \frac{V_{tot}}{D \cdot \delta_{cap} \cdot U_{inert}} = \frac{V}{D \cdot \delta_{cap} \cdot \left(\frac{g \cdot G}{D}\right)^{1/3}} \tag{2.11}$$

where V is the total melt volume and D is the spreading channel width.

Gravity-viscous regime of liquid spreading

In case viscosity of the melt is high and the melt supply flow rate is relatively low, the viscous force may affect, or eventually overwhelm, the inertia force. In such a viscous regime of spreading, the effect of viscosity must be accounted for in determining the characteristic velocity and spreading time scale, τ_{conv}.

It is noted that in the gravity-viscous spreading regime, the spreading process is largely driven by melt addition in the beginning of the spreading channel. In fact, major spreading process is terminated upon completion of melt delivery to the channel, although, some melt spreading would continue, very slowly, even after the melt discharge ends.

The melt delivery time period can be determined from the total melt volume V_{tot} and melt volume flow rate, $G = f(t)$ (m^3/s)

$$\Delta t_{dis} = \int_0^V \frac{dV}{G(t)} \tag{2.12}$$

or, for constant volumetric flow rate $\overline{G}$ (or simply, G),

$$\Delta t_{dis} = \frac{V_{tot}}{\overline{G}} \tag{2.13}$$

For spreading process with melt solidification, the assumption that

$$\tau_{conv,v} \simeq \Delta t_{dis} \tag{2.14}$$

appears appropriate for the gravity-viscous regime.

Employing the solution of the viscous spreading equation (e.g., Huppert, 1982 [32])

$$Z_{sp} \simeq \left(\frac{\frac{1}{3} g \cdot G^3}{\nu} \right)^{1/8} \cdot t^{1/2} \tag{2.15}$$

we obtain the characteristic velocity, U_{visc}, for the gravity-viscous regime.

$$U_{visc} = \frac{Z_{sp}(\Delta t_{dis})}{\Delta t_{dis}} = \left(\frac{\frac{1}{3} g \cdot G^3}{\nu}\right)^{1/8} \cdot \left(\frac{G}{V_{tot}}\right)^{1/2} \tag{2.16}$$

2.2.5 Solidification time scale τ_{sold}

Energy conservation equation is employed here to determine the characteristic time required for melt to solidify and reach the immoveable state. The equation using enthalpy formulation, H, is written for melt layer δ_{cap} as in the following.

$$\rho_m \frac{\partial H}{\partial t} = -\frac{q"_{up} + q"_{dn} - q_v \cdot \delta_{cap}}{\delta_{cap}} \tag{2.17}$$

where $q"_{up}$, $q"_{dn}$, q_v are upward and downward heat-removal fluxes (W/m^2) and internal heat generation rate (W/m^3), respectively.

From this equation, the solidification time scale τ_{sold} of a superheated melt, ΔT_{sup}, can be estimated as

$$\tau_{sold} = \delta_{cap} \rho_m \frac{C_{p,m} \cdot \Delta T_{sup} + \eta \cdot H_{fusion}}{q"_{up} + q"_{dn} - q_v \cdot \delta_{cap}} \tag{2.18}$$

η is the fraction of the latent heat of fusion which needs to be removed until the melt becomes immovable.

2.2.6 Scaling equation for one-dimensional melt spreading with solidification

As it can be seen, the dimensionless time scale combines parameters of the process (V_{tot}, G, ΔT_{sup}), geometry (D), boundary conditions (h_{conv}, T_{env}) and

melt physical properties (H_{fusion}, $C_{p,m}$, ρ_m, ν_m).

The dimensionless length scale $\mathcal{L}$ represents a measureable (and highly reproducible) result of the spreading process (terminal spreading melt thickness, δ_s).

In order to obtain scaling laws we need to relate the dimensionless length scale $\mathcal{L}$ to the dimensionless time scale $\mathcal{T}$.

Inviscid analysis

In this section, we derive a scaling equation for gravity-inertia regime, assuming the validity of several linear heat and mass transfer relations. From the mass conservation equation we have

$$\mathcal{L} = \frac{\delta_s}{\delta_{cap}} = \frac{Z_o}{Z_{sold}} \tag{2.19}$$

where Z_{sold} and Z_o are the spreading lengths in case with and without solidification, respectively.

Since, the terminal film thickness is assumed uniform over the spreading area and equal to the capillary thickness, we have

$$Z_o = \frac{V_{tot}}{\delta_{cap} \cdot D} \tag{2.20}$$

In case of melt solidification, the spreading distance is assumed to linearly dependent on the spreading velocity U_s and the solidification time Δt_{sold}.

$$Z_{sold} \sim U_s \cdot \Delta t_{sold} \tag{2.21}$$

Putting Eq.(2.20) and Eq.(2.21) into Eq.(2.19), we have

$$\mathcal{L} \sim \frac{\tau_{conv}}{\Delta t_{sold}} \tag{2.22}$$

The solidification time period Δt_{sold} for the layer δ_s is defined as follows.

$$\Delta t_{sold} = \tau_{sold} \cdot \frac{\delta_s}{\delta_{cap}} = \tau_{sold} \cdot \mathcal{L} \tag{2.23}$$

From Eq.(2.22) and Eq.(2.23) we obtain the following scaling model for inviscid spreading:

$$\mathcal{L} = C \cdot \mathcal{T}^{1/2} \tag{2.24}$$

Since the proportionality coefficients in all the equations employed have order of unity, coefficient C should be about 1 ($C \simeq 1$). This is then confirmed by comparison to experimental data available.

Viscid analysis

In gravity-viscous spreading regime the scaling equation has similar form, but the dimensionless length and time scales should be modified to take into account the effect of viscosity.

We start from the same scaling relation as Eq.(2.24)

$$\mathcal{L}_v = C \cdot \mathcal{T}_v^{1/2} \tag{2.25}$$

with $\mathcal{L}_v$ and $\mathcal{T}_v$ are dimensionless length and time scales in viscous spreading regime.

It can be shown that

$$\mathcal{L}_v = \mathcal{L} \cdot \frac{\delta_{cap}}{\delta_v} \tag{2.26}$$

where δ_v is a characteristic length of the fluid layer in viscous regime, ($\delta_v > \delta_{cap}$).

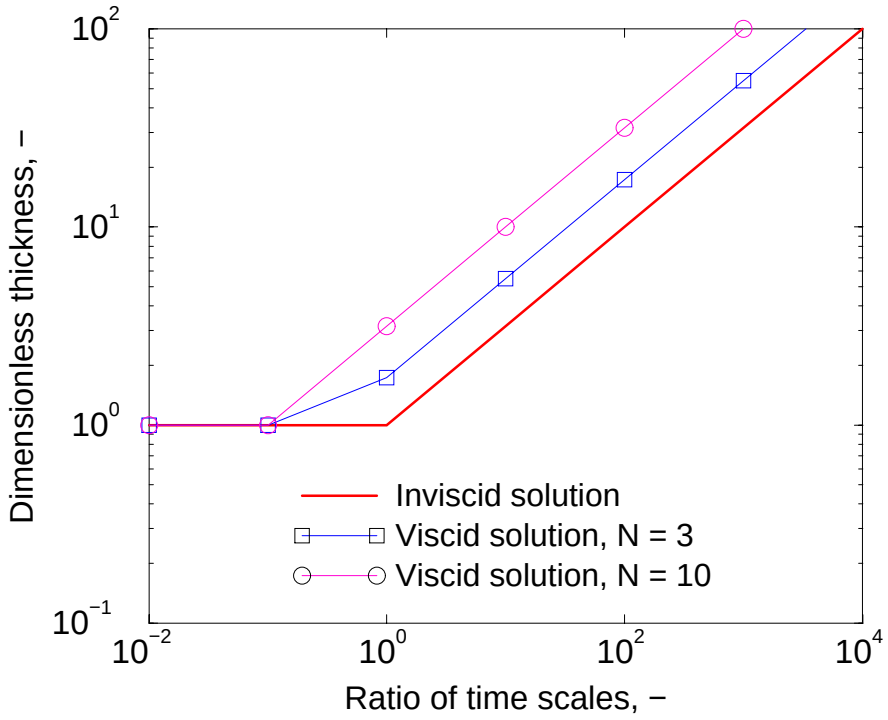

Figure 2.1: Scaling relations.

Knowing the characteristic velocity in the gravity-viscous spreading regime, we obtain

$$\delta_v = \frac{G}{D}\left(\frac{\frac{1}{3}g \cdot G^3}{\nu}\right)^{-1/8}\left(\frac{V_{tot}}{G}\right)^{1/2} \tag{2.27}$$

Assuming the linear dependence of the solidification time scale and the layer thickness, we have

$$\tau_{sold,v} = \tau_{sold} \frac{\delta_v}{\delta_{cap}} \tag{2.28}$$

Taking into account the above relations, Eq.(C.1) becomes

$$\mathcal{L} = C \cdot \mathcal{T}^{1/2} \left(\frac{\tau_{conv,v}}{\tau_{conv}} \right)^{1/2} \left(\frac{\delta_v}{\delta_{cap}} \right)^{1/2} \tag{2.29}$$

Using earlier derived equations, Eq.(B.4) for τ_{conv}, Eq.(2.12) for $\tau_{conv,v}$ ($\tau_{conv,v} = \Delta t_{dis}$), and Eq.(2.27) for δ_v, after algebraic manipulations, we have

$$\mathcal{L} = C_v \cdot \mathcal{T}^{1/2} \cdot \mathcal{N}^{1/2} \tag{2.30}$$

where coefficient C_v is of order of unity, but likely $C_v < 1.0$, and $\mathcal{N}$ is a viscosity number ($\mathcal{N} \geq 1$) defined as

$$\mathcal{N} = \frac{\nu^{1/8} \cdot V_{tot}^{1/2} \cdot g^{5/24}}{D^{1/3} \cdot G^{13/24}} \tag{2.31}$$

It can be seen that the higher flow rate G or lower the fluid viscosity ν, the smaller the viscosity number $\mathcal{N}$. If $\mathcal{N} < 1$, $\mathcal{N}$ = 1, and Eq.(2.30) becomes Eq.(2.24) obtained for the gravity-inertia spreading regime.

2.2.7 Scaling equation for melt spreading with solidification in two-dimensional channel

Geometry effect

In the following, we analyze spreading process in a channel with a fixed opening angle (Fig.2.2). Major assumption employed in the following development is that the spreading melt flow is restricted by the channel's side walls.

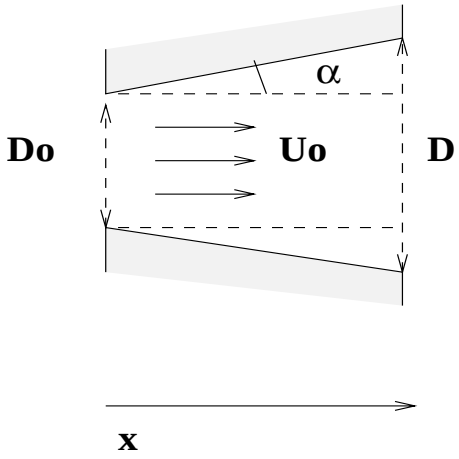

Figure 2.2: Spreading in a channel with a fixed opening angle

It can be seen that the width of the spreading section increases with the distance from the section's beginning as

$$D(x) = D_o + 2x \cdot tg\alpha \tag{2.32}$$

In order to derive a scaling rationale for melt spreading in a 2D channel, we will follow the methodology developed for 1D channel. The solidification time scale is assumed to be unchanged, since it is geometry-independent. The hydrodynamic spreading time scale $\tau_{conv,\alpha}$ has however to be corrected by a factor $\mathcal{A}$ defined as

$$\mathcal{A} = \frac{\tau_{conv,\alpha}}{\tau_{conv,1D}} \tag{2.33}$$

Equation for time scale $\tau_{conv,\alpha}$

We define $\tau_{conv,\alpha}$ and Z_{sp} as the time and spreading length of a melt volume V_{tot} when the spread melt thickness reaches δ_{cap}, providing thus the spreading area of S_{sp}.

$$Z_{sp} = \tau_{conv,\alpha} \cdot \vec{U}_{Z_{sp}} \tag{2.34}$$

Here $\vec{U}_{Z_{sp}}$ is the average spreading velocity, m/s.

From the mass conservation equation

$$V_{tot} = \delta_{cap} S_{sp}(Z_{sp}) \tag{2.35}$$

the spreading area can be determined as follows

$$S_{sp} = \frac{1}{2}[D_o + D(Z_{sp})] \cdot Z_{sp} \tag{2.36}$$

A parabollic equation with respect to Z_{sp} can be obtained from Eq.(2.36) as

$$tg\alpha Z_{sp}^2 + D_o Z_{sp} - V_{tot}/\delta_{cap} = 0 \tag{2.37}$$

Solving Eq.(2.37). one obtains

$$Z_{sp} = \frac{-D_o + \sqrt{(D_o^2 + 4V_{tot} tg\alpha/\delta_{cap})}}{2tg\alpha} \tag{2.38}$$

It can be shown that for the limiting case ($\alpha \to 0$) the spreading length approaches the same solution obtained for spreading in one-dimensional channel (size D_o).

$$\lim_{\alpha \to 0} Z_{sp} = \frac{V_{tot}}{D_o \delta_{cap}} \tag{2.39}$$

At the very beginning of the channel, the characteristic velocity can be determined as

$$U_o = \left(\frac{gG}{D_o} \right)^{1/3} \tag{2.40}$$

From the mass conservation equation, the section-average velocity is

$$U_x = \frac{U_o D_o}{D_x} = \frac{U_o D_o}{D_o + 2x tg\alpha} \tag{2.41}$$

Therefore, the length-average spreading velocity $\bar{U}_x$ is

$$\bar{U}_x(x = Z_{sp}) = \frac{1}{Z_{sp}} \int^{Z_{sp}} U(x) dx \tag{2.42}$$

$$\bar{U}_x(Z_{sp}) = \frac{U_o D_o}{2 Z_{sp}\ tg\alpha} ln \left(1 + \frac{2 Z_{sp}\ tg\alpha}{D_o} \right) \tag{2.43}$$

We obtain later

$$\tau_{conv,\alpha} = \frac{2Z_{sp}^2 tg\alpha}{U_o D_o ln(1+\frac{2Z_{sp}tg\alpha}{D_o})} \tag{2.44}$$

For $\alpha \to 0$ it can be shown that

$$\tau_{conv,\alpha} = \frac{V_{tot}}{D_o \delta_{cap}(gG/D_o)^{1/3}} \tag{2.45}$$

which is identical to the hydrodynamic time scale of spreading in one-dimensional channel.

For $\alpha \neq 0$, the characteristic time of liquid spreading is

$$\tau_{conv,\alpha} = \frac{2[D_o^2 + 2V_{tot}\ tg\alpha/\delta_{cap} - D_o\sqrt{D_o^2 + 4V_{tot}\ tg\alpha/\delta_{cap}}]}{U_o D_o\ tg\alpha\ ln(1+4V_{tot}\ tg\alpha/\delta_{cap}D_o^2)} \tag{2.46}$$

Introducing a dimensionless parameter P_α as

$$P_\alpha = \frac{V_{tot} tg\alpha}{\delta_{cap} D_o^2} \tag{2.47}$$

we re-write Eq.(2.46) in a compact form, taking into account the definition of $\mathcal{A}$ in Eq.(2.33).

$$\mathcal{A} = \frac{2[1 + 2P_\alpha - \sqrt{1+4P_\alpha}]}{P_\alpha ln(1+4P_\alpha)} \tag{2.48}$$

It can be shown that

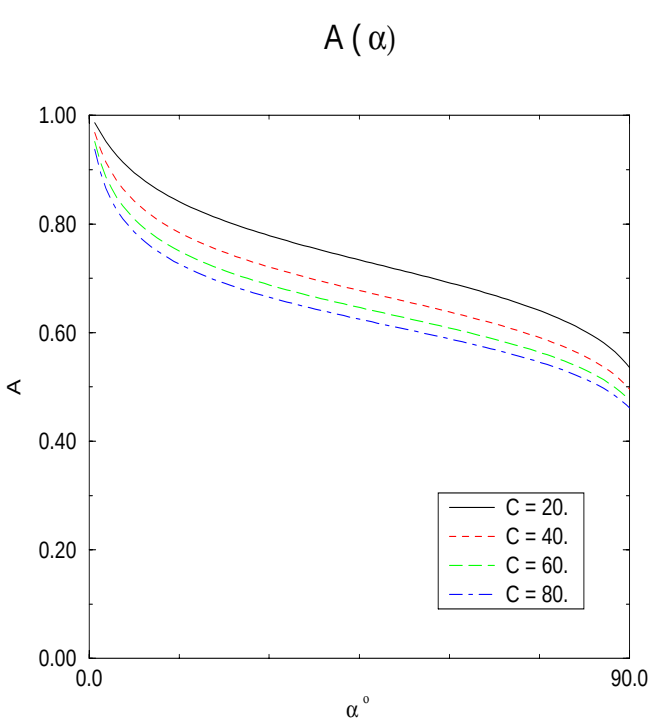

Figure 2.3: The dependence of $\mathcal{A}$ on the angle α

$$\lim \mathcal{A}_{P_\alpha \to 0} = 1 \tag{2.49}$$

The dependence of $\mathcal{A}$ on the angle α can be seen in Fig.2.3. In fact, $\mathcal{A}$ is of order of unity. It can be explained by compensating effects of the spreading velocity and channel size under the increasing spreading angle.

Inviscid and viscid solutions

Dimensionless length scale of the spreading process in the 2D channel with melt solidification has the form

$$\mathcal{L} = \frac{\delta_s}{\delta_{cap}} = \frac{S_{cap}}{S_{sol}} = \frac{V_{tot}/\delta_{cap}}{[D_o + Z_{sold} tg\alpha] Z_{sold}} \tag{2.50}$$

The spreading length Z_{sold} in the case of melt solidification is determined as

$$Z_{sold} = \bar{U}_x \cdot \tau_{sol}^{\delta} \tag{2.51}$$

where τ_{sol}^{δ} is the characteristic time required to solidify melt layer of thickness δ_{sol}.

Defining $\tau_{sol}^{\delta_{cap}}$ as the characteristic time necessary for the melt layer of known height δ_{cap} to solidify, and employing linear solidification law, Eq.(2.51) can be re-written as

$$Z_{sold} = \bar{U}_x \ \ \tau_{sol}^{\delta_{cap}} \ \ \frac{\delta_s}{\delta_{cap}} \tag{2.52}$$

Substituting $\bar{U}_x$ with Eq.(2.43), we obtain

$$Z_{sold} = \frac{U_o D_o}{2 Z_{sold} tg\alpha} \ \ ln(1 + \frac{2 Z_{sold}}{D_o} tg\alpha) \cdot \tau_{sol} \frac{\delta_s}{\delta_{cap}} \tag{2.53}$$

Since,

$$\mathcal{L} = \frac{[D_o + Z_{sp} tg\alpha] \ \ \tau_{conv,\alpha} \bar{U}_{Z_{sp}}}{\mathcal{L}[D_o + Z_{sold} tg\alpha] \ \ \tau_{sol} \ \ \bar{U}_{Z_{sold}}} = \frac{1}{\mathcal{L}} (\frac{\tau_{conv,\alpha}}{\tau_{sol}}) \tag{2.54}$$

the scaling equation similar to that for 1D spreading can be obtained

$$\mathcal{L} = C_\alpha \cdot \left(\frac{\tau_{conv,\alpha}}{\tau_{sol}} \right)^{1/2} \tag{2.55}$$

Using definitions of $\mathcal{T}$ and $\mathcal{A}$, the inviscid scaling equation can be written as in the following.

$$\mathcal{L} = C_\alpha \ \mathcal{T}^{1/2} \ \mathcal{A}^{1/2} \tag{2.56}$$

A viscid analysis can be performed in a way similar to that described above. As a result, Eq.(2.56) can be transformed into Eq.(2.57)

$$\mathcal{L} = C_\alpha \ \mathcal{T}^{1/2} \ \mathcal{A}^{1/2} \ \mathcal{N}^{1/2} \tag{2.57}$$

where $\mathcal{N}$ is defined by Eq.(2.31).

Since $\mathcal{A}$ is of order of unity, Eqs.(2.56)-(2.57) indicates that spreading in a two-dimensional channel, with spreading flows restricted by the channel's side walls, has essentially one-dimensional character.

2.2.8 Scaling equation for two-dimensional melt spreading with solidification in an open spreading area

Spreading regimes in the reactor melt retention device

Before deriving the equation for two-dimensional spreading in open area, it should be noted that, in the EPR scheme, core melt is assumed to possess feature sufficiently high fluidity. That is to say, the melt retention and heat-up in the intermediate crucible beneath the reactor vessel should provide such melt superheat and flowrate which are required for the gravity force to dominate over the friction force caused by the melt viscosity during its cooling and freezing.

Indeed, in the case of very small discharge rate of high-viscosity melt, the melt does not spread far from the release location, solidifying and building up in the inclined channel connecting between the reactor cavity and the open-area

spreading zone. Such highly-viscous spreading regime with very small melt flowrate are not considered here.

For the following analysis, the melt is assumed to flow through the 1D channel to the 2D spreading area. Obviously, even in this 1D channel, the melt will partially lose its heat to bottom structure (melt-crust convective heat transfer) and to upper structure (radiative heat transfer). It was found from S3E experiments at RIT that two-dimensional spreading into open area is much more efficient than one-dimensional spreading in channel. That is to say, the larger the width of the 1D channel, the lower the EPR spreading efficiency. Narrowing the 1D channel would increase the melt velocity, hence, reducing characteristic time of melt residence in the 1D section.

Based on observations from 2D melt spreading experiments, several regimes of melt spreading can be expected in the EPR melt retention device.

In the first, hydrodynamical, case (case H), the melt superheat is assumed very high, so that the effect of melt solidification during the spreading process is negligible. In an initial phase, the melt freely spreads into the 2D area and may even approach steady state predicted by open-channel flow theory (Moody, 1991 [45]). The spreading angle was assumed 45^o-degree in MELTSPREAD code calculations (Farmer, 1993 [26]). It was found from a simplified numerical analysis of open-channel flow (Moody, 1991 [45]) that angle of 56^o degree is more appropriate. Moody's result also qualitatively agrees with observations from water-spreading experiments by Theofanous et al. (1989) [46]. In the later phase, the spreading process is constrained by the concrete boundary wall of the melt retention device, rendering the spreading angle to open further than that predicted by the steady state solution of open channel flow. Unless the spread melt layer reaches its capillary thickness or solidifies, the melt will fill up all the 2D area available for spreading.

A particular situation of case "H" involves very high melt flowrate, so that the melt enters the 2D area and shortly reaches the opposite concrete wall, having small opening angle during this spreading phase. Due to the wall effect, the subsequent melt is decelerated, crawling along the boundary wall. At the same time, the melt spreads sidewards to enlarge the spreading area in the melt retention device. Crust formation may rapidly occur in the stagnant-flow area near the boundary wall. The melt spreads in the later phase is primarily governed by gravity force, which causes melt dam-breaking and dam-overflowing.

In the second, thermally-dominated, case (case T), the melt spreads into the 2D area, slowing down in velocity and rendering rapid crust build-up in the leading edge. This frontal crust dam prevents the melt from further flowing forward. A melt pool is formed near the entrance into the 2D area, and subsequent melt motion is governed by liquid column spreading and dam-overflowing, since melt is continuously supplied into the pool. In this case, the spreading angle could be larger or smaller than the steady-state opening angle predicted by Moody (1991) [45], depending on a number of parameters, but primarily, on the total melt volume. It was found from SPREAD experiments (Suzuki et al., 1993, [20]) that the spreading angles were about 65^o degree (i.e. $130^o/2$), which are larger than the limiting angle of open channel flow (52^o degree).

In general, it is of interest to analyze the spreading process until the whole spreading area is filled. After that, physical process is largely governed by the melt pool filling and instantaneous liquid re-distribution due to gravity. In such a case, nearly uniform core debris cake would be formed in the melt retention device.

Parameters of melt spreading in open area

There are two different ways to characterize the melt spreading process in an open 2D area.

In the first approach, the thickness of the terminal spread melt layer δ_{sp} or its dimensionless number $\mathcal{L}$ can be employed as in the scaling rationale developed for 1D melt spreading process.

In the second approach, fraction of the spreading area filled with core melt can be employed to indicate the spreading efficiency. Since melt spreading in EPR plant is associated with given melt volume and given (maximum) spreading area, the second approach is more appropriate for reactor-related assessment.

However, since experiments are often performed at small scale and have large variations in parameters, the first approach is more general and appropriate for analyzing the experimental data and observations. The analysis method, once developed and validated against experiments, could, then, be easily modified for use in the EPR reactor safety assessment.

Characteristic time of melt spreading

It is known that hydrodynamics of liquid spreading in the 1D channel differs $\tau_{conv,1D}$ from that of spreading in open area $\tau_{conv,open}$, where rate of increase in spreading area is directly related to the perimeter bounding the current area occupied by liquid. That is to say, characteristic time for liquid to reach its capillary thickness in open area should be inversely proportional to P, which is the length of unbound liquid boundary.

We can write the following equation for the ratio $\mathcal{B}$ of hydrodynamic time scale in open area and 1D-channel.

$$\mathcal{B} = \frac{\tau_{conv,open}}{\tau_{conv,1D}} = \frac{D_o}{P} \tag{2.58}$$

Here D_o is the width of the 1D section at its entrance into the 2D spreading area.

$$P = D_o + 2 \cdot Z_{spr} \tag{2.59}$$

where Z_{spr} is the melt spreading length, limited either by geometrical constraint of the open spreading area (R) or the characteristic length determined from solidification.

$$Z_{spr} = min(R; \tau_{sold} \cdot U_o) \tag{2.60}$$

The first limiting case ($Z_{spr} \simeq R$) corresponds to H-regime discussed above. The second case corresponds to T-regime. U_o is melt velocity discharged from the 1D section and can be determined from Eq.(2.10) for U_{inert}.

We can write

$$B = \frac{\tau_{conv,open}}{\tau_{conv,1D}} = \frac{1}{1 + min(\frac{2 \cdot R}{D_o}; \frac{2\tau_{sold} \cdot U_o}{D_o})} \tag{2.61}$$

Application of the open channel flow theory

In this subsection, another approach to determine $\mathcal{B}$ is proposed. It is based on the open channel flow theory, see e.g. Moody, 1991 [45]; Fig.2.4.

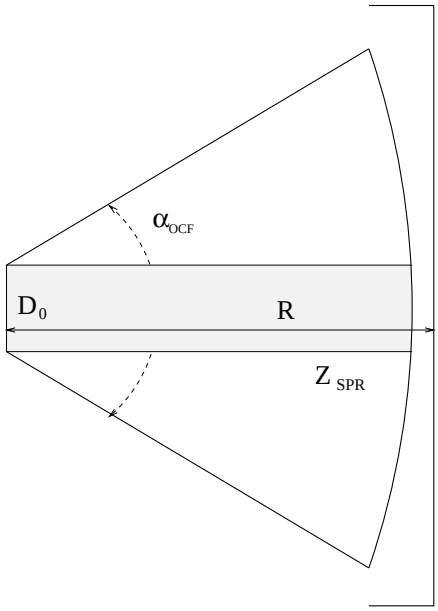

Figure 2.4: Parameters used in the open channel flow theory.

Dimensionless length scale of the spreading process with melt solidification has the form:

$$\mathcal{L} = C \ \mathcal{T}^{1/2} = C \ (\frac{\tau_{conv,2D}}{\tau_{sold}})^{1/2} \tag{2.62}$$

or

$$\mathcal{L} = C \ (\frac{\tau^f_{conv,1D}}{\tau_{sold}} \cdot \frac{\tau_{conv,2D}}{\tau^f_{conv,1D}})^{1/2} \tag{2.63}$$

where $\tau^f_{conv,1D}$ is the time of the melt spreading of the volume V_{tot} in the 1D channel with the width D_o.

Now let us consider the ratio $\frac{\tau_{conv,2D}}{\tau^f_{conv,1D}}$

$$\frac{\tau_{conv,2D}}{\tau^f_{conv,1D}} = \frac{\tau_{conv,2D}}{\tau^p_{conv,1D}} \cdot \frac{\tau^p_{conv,1D}}{\tau^f_{conv,1D}} \tag{2.64}$$

where $\tau^p_{conv,1D}$ is the time of the melt spreading of some particular volume V_p in the 1D channel with the width D_o, and the spreading length is Z_{spr} (see Fig.2.4). That means the times $\tau_{conv,2D}$ and $\tau^p_{conv,1D}$ are equal. Hence, with $\frac{\tau_{conv,2D}}{\tau^p_{conv,1D}} = 1$ we have:

$$\frac{\tau^p_{conv,1D}}{\tau^f_{conv,1D}} = (\frac{V_p}{D_o \delta_{cap} U_o})/(\frac{V_{tot}}{D_o \delta_{cap} U_o}) = \frac{V_p}{V_{tot}} \tag{2.65}$$

We define a dimensionless number $\mathcal{B}$ as:

$$\mathcal{B} = \frac{V_p}{V_{tot}} \tag{2.66}$$

From the spreading geometry we have:

$$\frac{V_{tot}}{\delta_{cap}} = \frac{\alpha_m}{360} \pi Z^2_{spr} \tag{2.67}$$

and

$$V_p = \delta_{cap} Z_{spr} D_o \tag{2.68}$$

Combining of these equations gives us the expression for $\mathcal{B}$

$$\mathcal{B} = D_o(\frac{360\delta_{cap}}{\alpha_m \pi V_{tot}})^{1/2} \tag{2.69}$$

Scaling law for open channel spreading with solidification

Essentially, the scaling law for spreading into 2D area is based on the concept of melt spreading in 1D channel, with accounting for the reduced hydrodynamic time scale of the unbounded liquid on horizontal surface. Exactly similar procedure as for 1D spreading was applied for deriving the relation between the time and length scales. As a result, the general viscid form can be written as follows.

$$\mathcal{L} = C_\alpha \ \mathcal{T}^{1/2} \ \mathcal{B}^{1/2} \ \mathcal{N}^{1/2} \tag{2.70}$$

with parameter $\mathcal{B}$ defined as in Table 2.9.

Table 2.9: Parameter $\mathcal{B}$

	$\mathcal{B}$
hydrodynamic regime	$\frac{1}{1+\frac{2R}{D_o}}$
open channel flow theory	$D_o \left(\frac{360\delta_{cap}}{\alpha_{\text{ocf}} \pi V_{tot}}\right)^{1/2}$
thermal-control regime	$\frac{1}{1+\frac{2\tau_{sold} U_o}{D_o}}$

2.2.9 Remarks on phenomenology, modeling and related uncertainties

Complexity of melt spreading phenomenology may be appreciated in the development of the scaling rationale which accounts for the various phenomena

and the physical properties. In reality, melt physical properties as well as local and instantaneous thermal hydraulic conditions may change over a wide range. Modeling and prediction of the time dependent parameters of melt spreading with solidification is, thus, quite complex. In this context, the melt stopping mechanism, variation of melt physical properties and their impact on the spreading process have caused extensive discussions and debate. Hopefully, since more data from property measurements and from melt spreading experiments may be available in future, a better understanding of these aspects may be achieved. Presently, however, sophisticated methods and theories (on melt physical properties e.g. viscosity) have not yet been brought up to the level when melt spreading process can be predicted with reasonable accuracy and reliability.

Despite many uncertainties in the quantification of separate effects and component phenomena which affect the melt spreading process, the thermodynamic nature of the scaling method described above allows overcoming 'micro'-uncer tainties by integrating them all together. Thus, not every detail of the spreading process in time and space is described, as in a kinetic approach. Rather, driving mechanisms were bounded and related to the final outcome (terminal-spread melt average thickness) of the spreading process.

However, it should also be noted that the above-described approach to the description of the spreading process does not replace the description of the spreading dynamics. It however is a coherent scaling methodology to analyze the spreading data and provide predictions for spreading scenarious. Likely, the terminal spreading melt thickness is not sensitive to experimental design factors, such as gate opening mechanisms or the like. In a broad sense, the present scaling concept is different from the previous, and current, modeling and analysis concepts, whose focus was placed on the spreading-dynamics parameters.

2.2.10 Summary

In section 3, a scaling rationale was developed to describe the spreading process with observations derived from small-scale experiments performed with simulant materials. The focus is the prediction of the spreading of molten corium in a hypothetical severe accident in a LWR.

The methodology is directed towards the predictions of those parameters of the melt spreadig process which are significant from the view point of safety, i.e. the average thickness of the melt layer and the spreading distance or area. Dynamics of the spreading process is not described by the methodology developed.

Although the regimes and governing mechanisms have long been identified, this is the first time the time scales and length scales are integrated together to establish scaling relations for melt spreading with solidification, in both gravity-inertia and gravity-viscous regimes.

The rationale, first developed for melt spreading in 1D channel, has been extended to describe spreading in a channel with fixed opening angle and spreading into an open area.

2.3 Validation of Scaling and Prediction Methodology

2.3.1 Validation strategy

The methodology employed for assessment was first developed as a scaling rationale for designing and analyzing melt spreading experiments. The scaling relations were then shown to be capable of predicting results of melt spreading experiments, including those at relatively large scales with prototypic core melts. A number of mechanistic equations and generic correlations were employed to enable a closed form scaling equations for different regimes and geometries. As such the scaling equations serve as an integral model for assessing and predicting characteristics of melt spreading.

The strategy adopted for validation of the melt spreading model includes:

- verification of component models and correlations which were employed as the basis to develop the scaling methodology;

- validation of the integral model against data and observations in one-dimensional simulant-material melt spreading experiments;

- validation of the model against data obtained from two-dimensional simulant-material melt spreading experiments; and

- validation of the model against data obtained from one and two dimensional high-temperature melt spreading experiments employing prototypic core melts.

2.3.2 Validation of component models and correlations

Heat transfer

Heat transfer from melt largely depends on spreading regime. The upward heat removal rate is governed by radiation flux from the melt surface. Convective heat transfer to gas environment is small in the prototypic reactor situation.

In experiments, however, both dry and wet spreading regimes were tested. Heat transfer from spreading melt to coolant in the wet case is determined by the cooling regime (convective, boiling). In the single-phase convective cooling, heat transfer from the melt crust to the coolant can be determined by using the correlation which was derived for convective heat transfer to a rough, phase change, boundary.

$$Nu = 0.0027 \cdot Pe \tag{2.71}$$

or

$$h_{conv} = 0.0027 \cdot \rho_{coolant} \cdot C_{p,coolant} \cdot U_{rel} \tag{2.72}$$

For the temperature, dry spreading experiments, the heat removal is radiative described by

$$q"_{rad} = \varepsilon \sigma_B (T_m^4 - T_{env}^4) \tag{2.73}$$

where T_m and T_{env} are melt temperature and temperature of the environment, respectively, σ_B is Bolztmann coefficient $\sigma_B = 5.67 \cdot 10^{-8} W/(m^2.K^4)$, and ε is emissivity coefficient. For oxidic crust and melt, ε approaches 1.

Downward heat removal rate q''_{dn} can be evaluated as

$$q''_{dn} = h_{conv,dn} \cdot (T_m - T_{m,sold}) \tag{2.74}$$

providing that the bottom crust forms during the melt-substrate initial contact. The convective heat transfer from the melt flow to the crust boundary is evaluated by Eq.(C.5), which was shown to be valid in a large range of Peclet numbers. In a dimensional form, we have

$$h_{conv,dn} = 0.0027 \cdot \rho_{melt} \cdot C_{p,melt} \cdot U_{sp} \tag{2.75}$$

The above correlation was validated extensively against experimental data obtained in RIT and elsewhere. In particular, experiments on jet impingement on an ablating surface, jet impingement with crust formation and on hole ablation were shown to be governed by the convective heat transfer to a phase change boundary. Dinh and co-workers (1997) have shown that the surface roughness associated with the phase change process enhances energy transfer from the melt to the ablating structure. In a series of water-ice and water-salt ice jet impingement experiments it was recognized that the surface roughness, resulting from the phase change of the melting plate material was a controlling factor in the transition from laminar to turbulent heat transfer regimes in the jet stagnation zone. Experimental observations from the jet impingement research can be extended to the vessel ablation conditions and for heat transfer between the melt flow and crust in spreading situations, considered here, due to the underlying similarities in the physical mechanisms between these processes.

The change of phase of an ablating wall material will produce a roughened surface, regardless of whether or not the conditions for crust layer existence are met. This, in turn, influences the hydrodynamic and thermal boundary layers which must develop and flow past the surface. When the surface roughness becomes thicker than the hydrodynamic sublayer the convective heat transfer will be enhanced, and more importantly, the dependence upon length scales may be reduced or eliminated altogether. Determination of the convective heat transfer from the melt flow to the crust interface will, from classical considerations, depend upon the in-hole skin factor (C_f'), and the Re and Pr numbers for the flow. Under the rough surface conditions associated with phase change, the viscous sublayer is believed to be thin and the skin factor of the surface will become independent of Reynolds number as is the case for common pipe flow. It is clear that the impact of the surface roughness will be significantly influenced by values of the melt fluid Pr number since this number reflects the relationship between the inertial and thermal boundary layers.

For turbulent flow conditions, which is the case in the prototypical situation, the energy transfer can be determined using the Reynolds analogy

$$h = \frac{1}{2} U_\infty \cdot \rho \cdot C_p \cdot C_f' \tag{2.76}$$

For rough surfaces the value of C_f' may range from 0.005 to 0.007. Eq. 2.76 can be easily rearranged as

$$Nu = \frac{1}{2} \cdot Re \cdot Pr \cdot C_f' = \frac{1}{2} C_f' \cdot Pe \tag{2.77}$$

It should be noted that the combination of the Re and Pr numbers removes any influence of the fluid viscosity, and the governing dimensionless group then becomes the Peclet number.

Characteristic velocity of spreading

Equation (2.10) represents the dependence of U on gravity and melt volume flow rate. As it can be seen, no fluid properties are present. This agrees well with the classical spreading results. Velocities estimated by using Eq.(2.10) are in reasonable agreement with experimental data of nearly-isothermal gravity-inertia spreading tests (CORINE, RIT/S3E, FzK/KATS).

Eq.(2.16) gives fairly good assessments for the spreading velocity in CORINE tests [28], using glycerol as melt simulant.

Melt stopping criteria

If no solidification is involved or solidification occurs much later than the termination of the spreading process, the spread melt thickness is equal to the liquid capillary thickness. This length scale δ_{cap} is typically 5 to 10 mm (4.1 mm for cerrobend melt, 4.9-5.3 mm for binary salt and oxide melts and 9-10 mm for thermite melt). This length scale agrees well with spread-fluid thickness observed in nearly-non-freezing or isothermal spreading tests RIT/S3E, FzK/KATS, CEA/CORINE.

In prototypical reactor cases, $\mathcal{L}$ may vary in a wide range, depending on reactor design and severe accident management schemes adopted and on corium composition and melt relocation scenarios (cavity flooding before or after melt release and spreading). A range of $\mathcal{L}$ lower than 30 (i.e. less than 20 cm) is favorable for the severe accident management scheme utilizing water flooding on the containment floor to cool the debris from above.

In early experiments conducted at Brookhaven (using Pb melt spreading under water) $\mathcal{L}$ is estimated to be up to 10 (Greene et al., 1988 [16]). In the CORINE experiments using eutectic Pb-Sn melt, the dry spreading tests resulted in $\mathcal{L}$ up to 5, while the spreading under water gives $\mathcal{L}$ up to 30 (Veteau and Wittmaack, 1995 [28]). In KATS-series (with Al_2O_3 and Fe melts) $\mathcal{L}$ is from 1.2 to 2 (Scholtyssek et al., 1996 [34], Fieg et al., 1996 [23], Fieg et al., 1997 [35]). In dry-spreading COMAS tests (with $UO_2 - ZrO_2 - Cr_2O_3 - FeO - Fe$ melt) $\mathcal{L}$ is about 3 (Steinwarz, 1997 [24]).

The parameter η is unknown for multi-component melts, in particularly, for binary oxidic and prototypic corium melts. Earlier, $\eta \simeq 0.55$ was assumed for stainless steel melt (56 K mushy zone) in order to interpret results of the SPREAD experiments (Suzuki et al., 1993, [20]). For binary oxidic melts, the latent heat of fusion is equivalent to sensible heat with superheats of about 500 K. Thus, the role of heat of fusion may be comparable to the effect of melt superheat (typically, in the range 0 to 200K).

2.3.3 One-dimensional melt spreading experiments

RIT Experiments

Three major series of experiments, both dry spreading tests and spreading under coolant tests were performed at RIT within the S3E program (Scaled Simulant Spreading Experiments). Various low and intermediate temperature melt simulants were employed as working fluid. Series 3 includes 6 experiments, in which a high-temperature binary-oxide melt was employed as the working fluid.

Cerrobend spreading experiments

Table 2.10: Experimental Conditions of Cerrobend Spreading Tests in Water (Series 1&2)

Test #	melt	V_{melt} (l)	T_{melt} (^{o}C)	coolant	T_{cool} (^{o}C)	V_{cool} (l)	δ_{cool} (cm)
2MW-C1	cerrobend	3	90	water	40	9	4.5
2MW-C2	cerrobend	5	85	water	5	9	4.5
2MW-C3	cerrobend	5	105	water	5	15	7.5
2MW-C4	cerrobend	5.7	120	water	2	15	7.5
2MW-C5	cerrobend	5.7	120	water	2	15	7.5
2MW-C6	cerrobend	5.6	100	water	3	15	7.5
3MW-C1	cerrobend	10	80	water	16	30	4.5
3MW-C2	cerrobend	10	80	water	45	30	4.5
3MW-C3	cerrobend	19	80	water	16	30	4.5

Table 2.10 and Table 2.11 present experimental conditions and data (spreading velocity and spreading distance) along with results of analysis by the scaling model respectively. Both viscid and inviscid equations were tested against the data. In addition, sensitivity of the scaling parameters to η (fraction of heat of fusion to be removed during the spreading process) is investigated.

Table 2.11: Analysis of Cerrobend Spreading Tests in Water (Series 1&2)

Test #	L_{spread} (m)	$\mathcal{L}_{exp}$	$\mathcal{T}$		η=0.5		η=1.0	
			η=0.5	η=1.0	$\mathcal{L}^{model}_{inviscid}$	$\mathcal{L}^{model}_{viscid}$	$\mathcal{L}^{model}_{inviscid}$	$\mathcal{L}^{model}_{viscid}$
2MW-C1	>2	3.56	7.92	4.11	2.81	3.82	2.03	2.75
2MW-C2	1.2	9.90	21.90	11.16	4.68	7.22	3.34	5.15
2MW-C3	1.55	7.66	23.87	12.97	4.880	7.54	3.60	5.55
2MW-C4	1.88	7.52	29.30	16.59	5.41	8.63	4.07	6.49
2MW-C5	>2	6.77	29.30	16.59	5.41	8.63	4.07	6.49
2MW-C6	1.6	8.31	26.79	14.35	5.17	8.22	3.78	6.01
3MW-C1	1.55	7.66	18.48	9.24	4.29	7.03	3.04	4.97
3MW-C2	3.1	3.83	8.53	4.26	2.93	4.77	2.06	3.37
3MW-C3	2.45	9.09	34.11	17.06	5.84	11.17	4.13	7.90

It can be seen that the scaling models are capable of predicting major dependences of the spreading distance (or terminal fluid average height) on melt volume V_{melt} and temperature difference ($T_{melt} - T_{cool}$) variations.

Molten salt spreading experiments

A binary salt $NaNO_3$-KNO_3 was used to represent a binary oxide mixture of prototypic core melt UO_2-ZrO_2. It should be noted that although differing by temperature level, the phase diagram of the binary salt is quite similar to that for one of reactor coria. Two salt compositions were employed: eutectic mixture (50-50%) and non-eutectic mixture (20-80%).

Analysis of the experimental results by means of the scaling model indicates that best agreement between calculated and measured $\mathcal{L}$ is achieved for η = 0.5. Thus, it suggests that in order to immobilize the spreading fluid, about half of the heat of fusion should be removed from the leading edge of the spreading melt.

Table 2.12: Experimental Conditions of a 20-80% (non-eutectic) $NaNO_3$-KNO_3 Salt in Oil

Test #	melt	V_{melt} (l)	T_{melt} (^{o}C)	coolant	T_{cool} (^{o}C)	V_{cool} (l)	δ_{cool} (cm)
2MW-S1	salt,20-80	5.8	364	paraffin	3	10	5
2MW-S2	salt,20-80	5	325	paraffin	0	10	5
2MW-S3	salt,20-80	5	320	paraffin	5	10	5
2MW-S4	salt,20-80	5	300	paraffin	5	10	5
2MW-S5	salt,20-80	5	280	paraffin	25	10	5
2MW-S6	salt,20-80	5	300	paraffin	25	10	5
2MW-S7	salt,20-80	5	320	paraffin	25	10	5
2MW-S8	salt,20-80	5	350	paraffin	25	10	5

Table 2.13: Experimental Conditions of Spreading of a 50-50% (eutectic) $NaNO_3$-KNO_3 Salt in Oil.

Test #	melt	V_{melt} (l)	T_{melt} (^{o}C)	coolant	T_{cool} (^{o}C)	V_{cool} (l)	δ_{cool} (cm)
2MW-E1	salt,50-50	5	250	paraffin	5	10	5
2MW-E2	salt,50-50	5	270	paraffin	25	10	5
2MW-E3	salt,50-50	5	250	paraffin	25	10	5
2MW-E4	salt,50-50	5	220	paraffin	25	10	5

Table 2.14: Analysis of Spreading of a 20-80% (non-eutectic) $NaNO_3$-KNO_3 Salt in Oil

Test #	L_{spread} (m)	$\mathcal{L}_{exp}$	$\mathcal{T}$		η=0.5		η=1.0	
			η=0.5	η=1.0	$\mathcal{L}^{model}_{inviscid}$	$\mathcal{L}^{model}_{viscid}$	$\mathcal{L}^{model}_{inviscid}$	$\mathcal{L}^{model}_{viscid}$
2MW-S1	>2	4.92	20.80	17.34	4.56	4.75	4.16	4.34
2MW-S2	>2	4.92	26.63	20.29	5.16	5.37	4.50	4.69
2MW-S3	1.7	5.79	27.89	20.86	5.28	5.50	4.56	4.76
2MW-S4	1.55	6.35	35.86	24.04	5.98	6.24	4.90	5.11
2MW-S5	1.06	9.29	57.34	30.04	7.57	7.89	5.48	5.71
2MW-S6	1.4	7.04	35.86	24.04	5.98	6.24	4.90	5.11
2MW-S7	1.75	5.63	27.89	20.86	5.28	5.50	4.56	4.76
2MW-S8	>2	4.92	22.33	18.17	4.72	4.92	4.26	4.44

Table 2.15: Analysis of Spreading of a 50-50% (eutectic) $NaNO_3$-KNO_3 Salt in Oil.

Test #	L_{spread} (m)	$\mathcal{L}_{exp}$	$\mathcal{T}$		η=0.5		η=1.0	
			η=0.5	η=1.0	$\mathcal{L}^{model}_{inviscid}$	$\mathcal{L}^{model}_{viscid}$	$\mathcal{L}^{model}_{inviscid}$	$\mathcal{L}^{model}_{viscid}$
2MW-E1	1.73	5.69	21.08	13.30	4.59	4.93	3.64	3.92
2MW-E2	>2.0	4.92	18.66	12.89	4.32	4.64	3.59	3.86
2MW-E3	1.7	5.79	21.08	13.30	4.59	4.93	3.64	3.92
2MW-E4	1.7	5.79	31.39	15.72	5.60	6.02	3.96	4.26

More importantly, this finding of the present study appears to valid for metallic alloy melt (cerrobend), for binary salt melts, and, as it is shown latter, for oxide melts. Interestingly, not type of phase change (first or second, eutectic or non-eutectic) but the latent heat of phase change is the primary parameter to be considered when explaining the differences observed in spreading of different materials. There is some relation between the composition of a binary (metallic-alloy, salt or oxide) mixture and the latent heat of fusion. However, such a relation is likely material-specific rather than general.

Oxide melt spreading

Three experiments of Series 3 were performed, employing a high-temperature binary-oxide melt as working fluid. Substrate materials were 5cm-thick common-sand concrete or 1cm-thick steel. Thermocouples were embedded in the concrete and steel substrates to measure the thermal response.

Experimental conditions of spreading tests of Series 3 can be seen in Tables 2.16 and 2.17.

Table 2.16: Experimental conditions for dry spreading tests of Series 3.

Parameter		Value
Melt material		30%-70% $CaO - B_2O_3$
Solidus temp.	K	1225 ± 5
Liquidus temp.	K	1323 ± 10
Melt volume	lit.	12
Flow rate	l/s	$\sim 0.15 \pm 0.03$
Channel width	m	0.2
Channel length	m	3.6

Table 2.17: Specific conditions and results of dry spreading tests of Series 3.

Parameter	3MDC-Ox-1	3MDS-Ox-1	3MDS-Ox-2	Comments
Superheat	150 K	150 K	50 K	over liquidus
Substrate	5cm-concrete	1cm-steel	1cm-steel	concrete sidewalls
$Z_{sp,exp}$	3.0 m	2.95 m	2.15 m	uniform layer
$Z_{sp,cal}$	2.9 m	2.90 m	2.20 m	viscid model

The spreading distances observed are almost the same in the two spreading

tests 3MDC-Ox-1 and 3MDS-Ox-1. Probably, it is because the termination of the spreading process is largely governed by the solidification of the melt at its leading edge rather than on the process occurring behind the leading edge.

Test 3MDS-Ox-1 and Test 3MDS-Ox-2 were performed to investigate the influence of melt superheat on the spreading distance. It was expected from the pre-test calculations that the melt superheat has a small effect on the spreading characteristics even in the viscous-spreading regime; change from 150K to 50K superheat caused the spread distance decrease from 2.9 to 2.2 m. It is because the sensible heat is only a fraction of the total heat content to be removed to immobilize the spreading melt.

In all the above calculations, the fraction of heat of fusion contributing to the spread-melt heat content η is 0.5 . Upward radiation heat transfer is based on the oxide emissivity coefficient ($\sim$ 1) and initial melt temperature. Downward heat transfer is determined by equation which describes convective heat transfer from melt to its rough phase-change boundary. It was found that the pre-test predictions of the spreading distance were in an excellent agreement with the experimental results.

Finally, it should be noted that the RIT methodology was also validated against experimental data obtained from spreading of oxidic melt under water. Experimental conditions of oxide spreading tests under water can be seen in Table 2.18

The final spread distances and results of post-test calculations using the RIT model are presented in Table 2.19. It can be seen that the spread melt thickness (or the spreading distances) can be predicted quite well by the viscid model. The melt superheat in the three tests was only about 50^oK. Spreading under water involves very high heat removal rates in the boiling mode, causing the melt to become viscous and freeze rapidly.

Summary on validation against S3E experimental data

A large number of simulant material spreading experiments were performed using different fluids with different phase change behavior and properties and varying melt superheats, melt volume, melt flow rates and cooling conditions. Specifically, binary eutectic and non-eutectic melts were employed. Spreading tests on steel and concrete substrates were performed and compared. It was

Table 2.18: Experimental conditions for oxide spreading tests under water

Parameter		2MWS-Ox-1	2MWS-Ox-2	2MWS-Ox-3
Date		980219	980226	980305
Melt material		$CaO\text{-}B_2O_3$	$CaO\text{-}B_2O_3$	$CaO\text{-}B_2O_3$
Melt volume	lit.	2	5	10
Melt temperature	K	1373	1373	1373
Flow rate	l/s	$\sim$0.15	$\sim$0.15	$\sim$0.15
Channel width	m	0.2	0.2	0.2
Channel length	m	2	2	2
Water volume	lit.	50	50	50
Water depth	m	0.12	0.12	0.12
Water temperature	K	353	358	363

Table 2.19: Experimental results for oxide spreading tests under water

Parameter		2MWS-Ox-1	2MWS-Ox-2	2MWS-Ox-3
η		0.5	0.5	0.5
Spreading distance	m	0.45	0.8	1.15
$\mathcal{L}_{exp}$		4.49	6.31	8.79
$\mathcal{T}$		1.95	4.18	7.52
$\mathcal{L}_{theory}^{invisc}$		1.39	2.05	2.74
$\mathcal{L}_{theory}^{visc}$		4.58	7.00	10.00

found that the scaling relations developed are capable of predicting the spreading distance and the spread melt thickness data obtained in the S3E spreading experiments (see Fig.2.5).

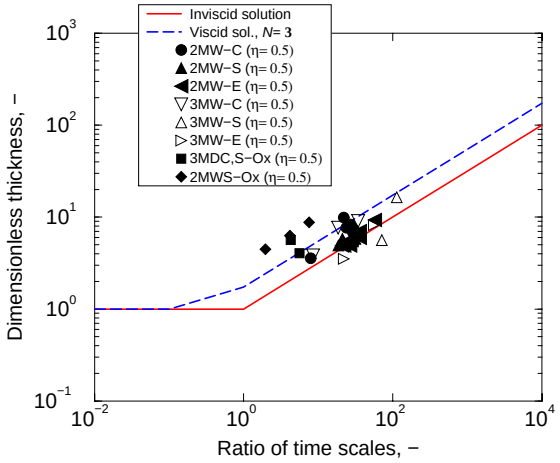

Figure 2.5: Validation of the RIT model against the S3E one-dimensional melt spreading experiments.

KATS Experiments

The scaling model predicts $U_s \simeq 1$ m/s for KATS-6 (iron melt) test, when the average spreading velocity observed was 0.85 m/s. Heat fluxes $q"_{dn} \simeq 2.8$ MW/m^2 and $q_{up} \simeq 0.7$ MW/m^2 were calculated in the scaling model.

Higher melt superheat (700 K for iron melt), but significantly lower melt flow rate (1.8 ... 2.5 l/s) was employed in KATS-7 experiment, compared to 20 l/s in KATS-6. The spreading velocity of 0.44 m/s was estimated by the scaling model, while it was experimentally observed in the range from 0.5 to 0.35 m/s. Very high heat fluxes, $q"_{dn} \simeq 3.8$ MW/m^2 and $q_{up} \simeq 1.64$ MW/m^2, were calculated in the scaling model.

KATS-5 and KATS-7 oxide-melt experiments are essentially similar, with the only difference being in the melt flow rate, 40 l/s in KATS-5 and 3.5 l/s in KATS-7 tests. The average measured spreading velocities were 0.8 m/s and 0.22 ... 0.3 m/s in KATS-5 and KATS-7, respectively. The calculated velocities were 1.0 and 0.44 for the two KATS-5 and KATS-7 tests. The scaling model predicts a difference 34% in the terminal fluid heights ($\mathcal{L} \sim G^{-1/6}$). Smaller difference (21%) between the measured spreading distances in the two tests is attributed to the different downward heat fluxes ($q"_{dn}$ = 1.25 and 0.56 MW/m^2), which affect the melt solidification.

Table 2.20: Performance of the RIT scaling model against KATS test data.

Test	Melt	$\mathcal{L}_{exp}$	$\mathcal{T}$	$\mathcal{L}^{invisc}_{theor}$	$\mathcal{L}^{visc}_{theor}$
KATS 5	oxide	1.33	1.48	1.21	1.21
KATS 6	iron	1.28	1.59	1.26	1.26
KATS 7	iron	1.47	2.74	1.65	2.44
	oxide	1.66	2.14	1.46	2.32
KATS 8	iron	1.00	6.19	1.00	1.00
	oxide	1.31	8.73	1.00	1.00
KATS 11,	iron	1.41	1.53	1.72	2.13
12, 13	oxide	2.23	3.25	1.91	3.45

In general, the KATS spreading distances can be predicted by the RIT scaling model. More importantly, the effect of different parameters observed in the KATS experiments can be reproduced, with excellent results, by the RIT scaling model.

2.3.4 Two-dimensional melt spreading experiments

There are very limited number of experiments of melt spreading into open area. The general observation is that the spreading is highly efficient in these cases, and the spread melt thickness is small.

Table 2.21: Experimental conditions of 2D SPREAD tests (Suzuki, 1993).

Test	Type of test	Volume (m^3)	T_{melt} (^oK)	Melt entrance width,(m)
14	2D,dry	0.01	1584	0.05
15	2D,dry	0.009	1587	0.05
16	2D,dry	0.017	1585	0.05
17	2D,dry	0.016	1625	0.05

2D SPREAD Experiments

Conditions, results and analysis of 2D SPREAD experiments are shown below. It can be seen that the maximum spreading efficiency is achieved ($\mathcal{L}$ = 1). The inviscid model was shown to be able to predict the test results.

Table 2.22: Analysis of 2D SPREAD tests by the RIT model.

Test	$\mathcal{L}_{exp}$	$\mathcal{T}$	$\mathcal{L}_{theor}^{invisc}$	$\mathcal{L}_{theor}^{visc}$
14	1.0	2.4	1.0	1.0
15	1.2	2.4	1.0	1.1
16	1.2	4.4	1.0	1.5
17	1.09	4.6	1.0	1.5

2D RIT experiments

Within the S3E program, experiments were performed on spreading of intermediate-temperature molten-salt and high-temperature oxide melt into an open area. Analysis of results of these tests indicates that the spreading area (terminal spread melt thickness) can be predicted by the 2D scaling model developed at RIT and described early in this report.

Table 2.23: Analysis of S3E molten-salt 2D-spreading (dry and wet) tests.

Test	η	$\mathcal{L}_{exp}$	$\mathcal{T}$	$\mathcal{L}_{theory}^{invisc}$	$\mathcal{L}_{theory}^{visc}$
2DW-S1	0.5	3.58	73.34	2.78	6.31
2DW-S2	0.5	3.28	63.61	2.59	5.87
2DW-S3	0.5	2.81	52.09	2.35	5.32
2DD-S1	0.5	1.09	6.09	1.00	1.82
2DD-S3	0.5	1.41	10.53	1.00	2.53
2DD-S6	0.5	1.36	5.40	1.00	2.18

Among theories tested for 2D spreading, the open-channel flow theory provides best agreement between the calculated terminal thickness and the experimental data. This theory will be employed in the assessment performed and presented below. It should be noted that melt spreading into an open area is significantly different from the one-dimensional spreading. As melt spreads in all directions, the hydrodynamic spreading time scale is remarkably reduced, and hence the spreading area is significantly enhanced. As a result, the spread melt thickness in the open-area spreading case may decrease by multiples of 3 to 10, compared to one-dimensional spreading process.

Table 2.24: Experimental Conditions of 2D Binary Oxide Spreading Tests

Test	Melt volume (l)	Flow rate (l/s)	T_{melt} (^{o}C)	Melt entrance width, (m)	T_{cool} (^{o}C)
2DDS-Ox-1	12	0.05	1100	0.1	dry
2DWS-Ox-1	12	0.15	1200	0.1	14
2DWS-Ox-2	12	0.15	1100	0.1	14
2DWS-Ox-3	12	0.15	1100	0.1	75

Table 2.25: Analysis of 2D RIT/NPS Oxide Melt Experiments

Test	$Melt$	Spreading area (m^2)	$\mathcal{L}_{exp}$	$\mathcal{T}$	$\mathcal{L}^{invisc}_{theory}$	$\mathcal{L}^{visc}_{theory}$
2DDS-Ox-1	$CaO\text{-}B_2O_3$	0.65	2.4	7.2	1.0	4.0
2DWS-Ox-1	$CaO\text{-}B_2O_3$	0.95	2.5	20.2	1.2	4.3
2DWS-Ox-2	$CaO\text{-}B_2O_3$	0.75	3.2	22.7	1.2	4.6
2DWS-Ox-3	$CaO\text{-}B_2O_3$	0.80	3.0	22.7	1.2	4.6

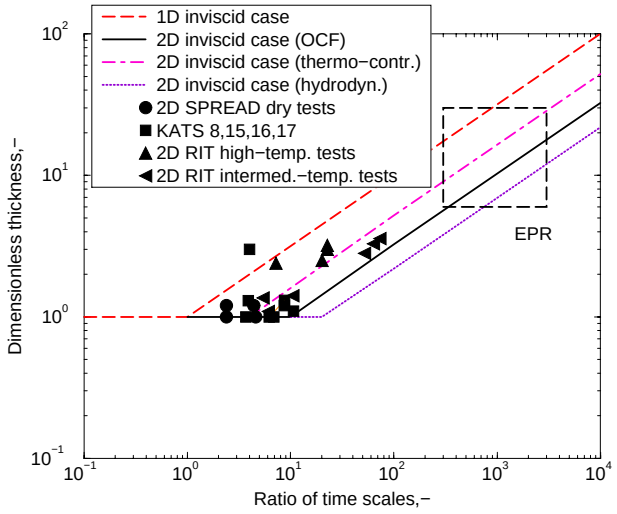

Figure 2.6: Scaling analysis of two-dimensional melt spreading experiments.

2.3.5 Spreading experiments involving core melts

High temperature, prototypic core melt spreading experiments were performed in several facilities. Straight one-dimensional channels and channels with an opening angle were employed in these experiments. It should be noted however that the melt spreading process is bound by the side walls. It has been shown early in our theoretical analyses that the spreading of melt into a channel with an opening angle, but bound by side walls, is essentially one-dimensional.

COMAS Experiments

Results of analysis of COMAS core melt spreading tests by the RIT model are shown in the following table. The spread melt thickness is re-calculated from the total spread melt volume and the spreading distance, taking into account the experimental observation that the terminal spread melt thickness is quite uniform. It can be seen from the spreading distances calculated, that the RIT viscid model is able to predict the spreading distances. The preference of the viscid model over the inviscid model is related to the absence of melt superheat in COMAS 5a and rather low superheats in other tests. The higher the melt

superheat, the more inviscid the spreading becomes.

Table 2.26: Analysis of COMAS tests.

Test	Type of substrate	Flow rate (m^3/s)	$\mathcal{L}_{exp}$	$\mathcal{T}$	$\mathcal{L}_{theor}^{invisc}$	$\mathcal{L}_{theor}^{visc}$
COMAS 5a	concrete	0.0135	3.1	6.36	2.5	3.1
	ceramic	0.0135	3.2	6.36	2.5	3.1
	cast iron	0.0135	3.4	6.36	2.5	3.1
COMAS EU-1	concrete	0.005	3.9	8.73	2.9	4.8
	ceramic	0.0016	5.5	11.72	3.4	7.5
	cast iron	0.005	3.7	8.73	2.9	4.8
COMAS EU-2b	concrete	0.01	3.7	8.1	2.8	3.8
	ceramic	0.01	3.7	7.5	2.7	3.6
	cast iron	0.01	3.7	7.5	2.7	3.6

COMAS EU-4 corium spreading test has a special arrangement of the spreading channel, with an opening angle of 45^o (see Fig.2.7). The initial melt temperature in the 2D section estimated in the range between 1950^o C and 2050^o C. Several measurements indicate that the most probable initial melt temperature was 2000-2050^oC, which is 100-150K superheat. Thus, the melt spreading was largely inviscid.

The COMAS EU-4 test is analyzed by the RIT two-dimensional scaling model for spreading into wall-bound channel. The spreading area S_{spread} is calculated from the spread thickness and compared to the spreading area $S_{spread,exp}$ obtained in the COMAS EU-4 experiment. Characteristic velocity $U \sim$1.2 m/s is obtained by integrating the given transient velocity over length of the 1D section. The mass flow rate is estimated by using 1D spreading model. Results of the scaling analysis are presented in Table 2.27. It can be seen that the inviscid model shows an excellent performance.

FARO Experiment

Experimental conditions and analysis of FARO experiment LS-26 are shown in the following tables. The experiment was performed with essentially no

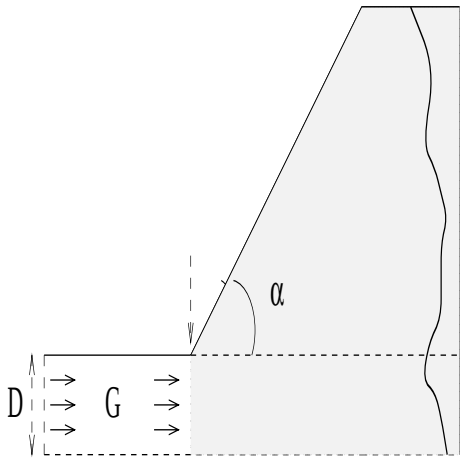

Figure 2.7: COMAS EU-4 geometry.

Table 2.27: Analysis of COMAS EU-4 spreading test.

η	T_{melt}^{init} (^{o}C)	$\mathcal{T}$	$\mathcal{L}_{exp}$	$\mathcal{L}_{model}^{invis}$	$\mathcal{L}_{model}^{vis}$
0.5	2050	19.4	3.3	3.3	4.6
0.5	2000	17.3	3.3	3.1	4.4
0.5	1950	14.5	3.3	2.8	4.0

superheat. Therefore, the viscid model should provide a better prediction. It can be seen that the spreading distance calculated by the RIT viscid model is in excellent agreement with the experimental result.

VULCANO experiment

Experimental conditions and analysis of VULCANO experiments VE-U1 and VE-U3 are shown in the following tables. The experiments were performed with essentially no superheat. Therefore, the viscid model should provide a better prediction. It can be seen that the spreading distances calculated by the RIT viscid model are in excellent agreement with the experimental results.

Table 2.28: Experimental conditions of FARO core melt spreading test.

Test	Melt composition	Type of test	Mass (kg)	T_{melt} (^oK)	Melt entrance width
LS-26	UO_2/ZrO_2	2D	230	2923	0.15

Table 2.29: Experimental results and analysis of the FARO LS-26 test.

Test	Flow rate (m^3/s)	S_{spread} (m^2)	$\mathcal{L}_{exp}$	$\mathcal{T}$	$\mathcal{L}^{invisc}_{theor}$	$\mathcal{L}^{visc}_{theor}$
LS-26	0.0018	0.35	14.8	29.4	4.5	14.5

Pre-test calculations and analysis of COMAS EU-2b test

The COMAS EU-2b experiment was designed to investigate the effect of addition of SiO_2 in the core melt.

Addition of SiO_2 into the oxidic R-corium will complicate the multi-component oxidic mixture of the melt. It may slightly decrease the melt density. More importantly, SiO_2 will form a mixture with other oxides, changing the phase diagram. In particular, one expects a lower solidus and lower liquidus, with even a larger temperature difference over the mushy phase. Apparently, silica as a network-forming oxide will increase the melt viscosity. Results of MCCI-related measurements of viscosity of oxidic mixture (ACE program) indicate that the viscosity of silica-based melt is very high, especially, in the mushy phase region. It is not clear whether the melt behaves as a Newtonian liquid or not.

It is clear that viscid solution is required to analyze such a test as the COMAS EU-2b. Uncertainties remain with respect to the viscosity, and the melt flowrate chosen in the present pre-test calculations. Based on measured data from COMAS EU-1 and COMAS 5a tests, it appears that the viscous melt has smaller melt discharge rate for the given hydraulic head, but bigger friction losses due to the melt higher viscosity.

Table 2.30: Experimental Conditions of VULCANO Tests

Test	Type of test	Mass (kg)	T_{melt} (^oK)	Melt entrance width
VE-U1	2D	47	2200	0.08
VE-U3	2D	27	2370	0.08

Table 2.31: Experimental Results of VULCANO Tests

Test	Flow rate (m^3/s)	S_{spread} (m^2)	$\mathcal{L}_{exp}$	$\mathcal{T}$	$\mathcal{L}^{invisc}_{theor}$	$\mathcal{L}^{visc}_{theor}$
VE-U1	0.00043	0.4	3.8	2.6	1.3	4.2
VE-U3	0.00025	0.1	8.6	11.1	2.8	8.9

In the present sensitivity study the melt flowrate is chosen in between 5 l/s and 15 l/s (see Table 2). The melt temperature varies from 1900 to 2000 C, as planned by Siempelkamp GmBH team.

Table 2.32: Experimental conditions of COMAS EU-2b (* - expected variation range).

Parameter	Unit	Course 1	Course 2	Course 3
Melt material	-	Corium R' (10% SiO_2)		
Melt temp.	^{o}C	1900-2000		
Melt mass	kg	1050/3=350		
*Melt flowrate	l/s	5-15		
*Melt viscosity	Pa·s	0.0086-0.086		

Results of the spreading analysis are present in Table 3 for varied melt viscosity, melt flowrate and initial melt temperature. It can be seen that the spreading distance calculated is sensitive to:

- melt temperature;
- melt flowrate;

- melt viscosity;

The upper limit of predicted distances is more than 5 m, while the lower limit is about 3 m. Even with relatively high melt temperature (2000 C), 4 m is the value to expect.

Table 2.33: Pre-test calculations of the COMAS EU-2b spreading experiment

T_{melt}^{init}	L_{pred} (m), ν=0.0086 (Pa·s)			L_{pred} (m), ν=0.086 (Pa·s)		
(^{o}C)	G=5 (l/s)	G=10 (l/s)	G=15 (l/s)	G=5 (l/s)	G=10 (l/s)	G=15 (l/s)
2000	3.9	5.0	5.8	3.4	4.3	5.0
1950	3.8	4.8	5.6	3.2	4.2	4.8
1900	3.6	4.6	5.3	3.1	4.0	4.6

Three conclusions were drawn from this pre-test analysis.

- For the COMAS EU-2b experiment, addition of 10% of SiO_2 may cause a significant increase in melt viscosity. As a result, the melt discharge time period may be longer than that observed in COMAS-5a (not taking into account the effect of section modification). The lower melt flowrate resulted from the higher melt viscosity and the effect of higher viscosity itself are likely compensating the effect associated with higher melt superheats planned in the COMAS EU-2b test.
- Major uncertainties in the COMAS EU-2b test are melt flowrate and melt viscosity. The former can be resolved from the test results, while the later should be estimated or measured to ease the post-test analysis.
- Results of sensitivity study were tabulated in the above section. It is expected that the spreading length in the COMAS EU-2b is about 4 m, based on the scaling model and judgements made with respect to experimental uncertainties.

Observation from experimental results indicated that the core melt spread to a distance of approximately 4 m. It confirmed the excellent pre-test prediction, made by RIT, of the spreading distance in the COMAS EU-2b experiment.

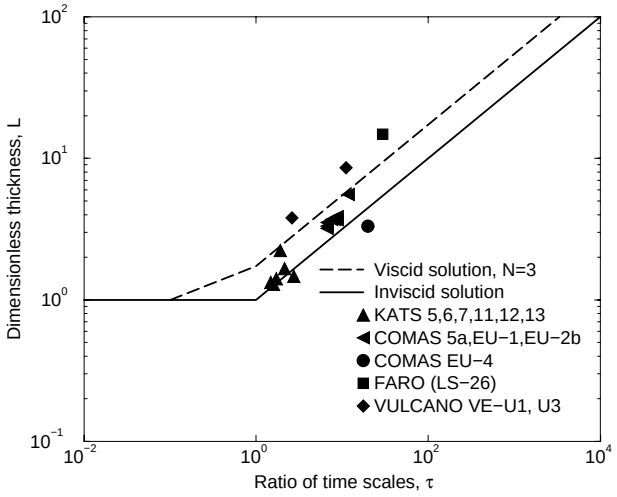

Figure 2.8: Validation of the RIT model against data from high-temperature melt spreading experiments.

2.4 Reactor Application

2.4.1 EPR melt retention device

In the retention device design at the moment the walls of the reactor pit, below the RPV, are covered with a specific sacrificial concrete. If this layer is eroded the melt will face either a protective layer, in the cylindrical part, or the melt plug, at the bottom. This plug will melt through and release the corium (Fischer, 1999) [53]. Provided the melt height is 2.0 m, the discharge velocity may be up to 5 m/s. For an initial opening of 0.2 m^2, the volume flow rate of core melt discharged is estimated to be of the order of 1 m^3/s, or 7 Mg/s. This strategy of melt accumulation over time and discharge through a large hole is called the one-shot melt release, providing relatively high melt flow rate (10 to 20 Mg/s) and with sufficient melt superheat (100K to 200K), since addition of the concrete products to the corium decreases the melt liquidus and solidus temperatures considerably.

2.4.2 Selected scenarios of core melt accident progression

According to the worst-case scenario, prior to the core melt discharge, the total mass of the homogeneous mixture of metal and oxide melts available for delivery to the spreading channel was found to vary in the range from 300 to 400 Mg (40 to 60 m^3). Two cases are selected for design base assessment (case A and case B). In case A, minimum amount of concrete slag is assumed to mix with the oxidic core melt. In case B, maximum amount of concrete slag mixing is assumed. Parameters of these cases are provided by Siemens KWU, based on results of the Siemens study of core melt relocation and melt-concrete interactions in the intermediate concrete crucible and its rupture.

Table 2.34 shows parameters of melt delivery conditions, melt physical properties and geometrical characteristics of the melt retention device. These parameters are used in the assessment.

It should be noted here that the hole ablation and melt discharge are not modeled here. The discharge melt flow rate is time-dependent and may be significantly different for different scenarios (case A and case B). It is our judgement that addition of large amount of concrete slag makes the mixture difficult to be ejected. To enable a conservative assessment of the spreading characteristics, the melt release time period is chosen 6 times larger in case B than that in case A. The difference in melt discharge rate is however smaller (about 4 times), owing to the larger melt volume in case B (larger melt mass and smaller melt density).

Section IV of Table 2.34 also depicts variation range of key modeling parameters. This reflects the phenomenological uncertainties and takes into account the current understanding. While the variation range for η, C_{conv} and α_{oct} is sufficiently small, the variation range for C is rather big. In fact, the variation range of C envelopes uncertainties induced by assumptions and idealization employed in deriving the scaling methodology.

2.4.3 Spreading efficiency

The objective of the assessment is to determine the characteristics of the core melt spreading in the EPR melt retention device. The methodology developed

Table 2.34: Input parameters and uncertainties. (Base-parameters are given in bold).

%	*Parameter*	*Case A*	*Case B*
	I. Melt Delivery Conditions:		
1	Total melt mass, (Metal+Oxide) M_{melt}, t	300-**332**	300-**350**
2	Melt release temperature, T_{melt}, C°	2410-**2442**-2500	1800-**2185**-2330
3	Environment temperature, T_{env}, K	400-**800**	400-**800**
4	Decay power, Q, MW	30-**35**-40	30-**39**-45
5	Melt release time, $t_{release}$, sec	20-**30**-60	60-**90**-120
	II. Physical Properties:		
6	Mass fraction of metallic melt, φ_{met}, wt%	**40**	**36.8**
7	Density of metallic melt, ρ_{met}, kg/m^3	6000-**6350**-6500	6200-**6450**-6600
8	Density of oxidic melt, ρ_{ox}, kg/m^3	7000-**7200**-7400	6300-**6500**-6700
9	Specific heat, $C_{p,m}$, J/(kg0·K)	2500-**3000**-3500	1200-**1260**-1300
10	Dynamic viscosity, μ_m, Pa·sec	0.01-**0.02**-0.1	0.01-**0.02**-0.1
11	Surface tension, σ_m, N/m	0.45-**0.47**-0.5	0.45-**0.47**-0.5
12	Fusion heat, H_f, MJ/kg	0.6-**0.62**-0.65	1.4-**1.45**-1.5
13	Liquidus/Solidus temperature, T_{liq}/T_{sol}, C°	**2510/2300**	**2330/1180**
14	Melting point temperature, $\frac{T_{liq}+T_{sol}}{2}$, C°	**2405**	**1755**
15	Emissivity, ε	**0.8**-1	**0.8**-1
	III: Geometrical Characteristics:		
16	Total spreading area, A_{EPR}, m^2	170-**180**	170-**180**
17	Transport channel width, W_{EPR}, m	**1.2**	**1.2**
	IV: Modeling uncertainties:		
18	η	0.4-**0.5**-0.6	0.4-**0.5**-0.6
19	Coefficient C_{conv}	(2.5-**2.7**-3)·10^{-3}	(2.5-**2.7**-3)·10^{-3}
20	Coefficient C	0.5-**1**-2	0.5-**1**-2
21	Open-channel theory spreading angle α_{oct}, deg.	45-**50**-60	45-**50**-60

Table 2.35: Assessment results for case A and case B (base-parameters/mean value from Monte-Carlo simulations).

%	*Result*	*Case A*	*Case B*
	1D inviscid theory:		
1	Spreading thickness, δ_s, cm	24/{32}	13/{18}
2	Spreading efficiency, ε_s	1.12/{1.04}	2.29/{1.79}
	1D viscid theory:		
3	Spreading thickness, δ_s, cm	31/{43}	21/{32}
4	Spreading efficiency, ε_s	0.87/{0.79}	1.4/{1.04}
	2D viscid open channel theory:		
5	Spreading thickness, δ_s, cm	4.6/{6.4}	3.96/{5.3}
6	Spreading efficiency, ε_s	5.84/{5.06}	7.6/{5.98}

at RIT is employed here to predict the core melt spreading characteristics in the EPR melt retention device. Although the prototypic situation is of spreading into open area, both the RIT method for spreading into an open area and the RIT method for one-dimensional spreading are employed. The latter is to provide the conservative lower bound estimate of the spreading area. The two methods are used to calculate the terminal spread melt thickness. Given the melt volume, the theoretical spreading area A_{theo} can be then determined. Comparison between the spreading area A_{theo} and the designed area A_{EPR} shows whether the spreading area is fully covered by core melt or the latter is piled up in only a smaller area. In reality, the maximum spreading efficiency ($\gamma = A_{real}/A_{EPR}$ = 1) is achieved when $A_{theo} \geq A_{EPR}$.

2.4.4 Base case results

Results of the assessment employing three solutions (1D inviscid, 1D viscid and 2D viscid open channel flow models) are shown in Table 2.35 for the two selected base cases. In each column, one sees two values; the first results from the deterministic calculation for the conditions given and for the model parameters chosen; the second (in brackets) value is a mean value from Monte-Carlo simulations (10^6 simulations), using the uncertainty variation range specified in Table 2.34. As it can be seen, the two sets of values are quite close. The results indicate the very high spreading efficiency of melt spreading into an open

area. Even in case B, when the melt viscosity is kept high, the melt volume is increased and the melt discharge velocity is decreased, the spreading efficiency remains about 6. As a result, the core melt is predicted to spread all over the spreading area provided in the EPR melt retention device.

2.5 Summary

2.5.1 Methodology

In general, reactor core melt spreading is a complex, thermofluid process, which is governed by

- (1) hydrodynamic motions of the spreading liquid (melt), and
- (2) solidification of melt during the spreading process.

The first phenomenon is affected by gravitational, inertial, viscous and surface forces. Depending on the viscosity, the liquid spreading may be categorized into gravity-inertia and gravity-viscous regimes. Phenomenon 2 is affected by heat transfer from core melt to surrounding media, i.e. downward: $q"_{dn}$ and upward: $q"_{up}$ heat removal rates, decay heat generation rate q_{vol}, and phase change behavior of the melt. For the EPR melt retention conditions, other phenomena (e.g., molten corium-coolant and molten corium-concrete interactions, melt stratification) are found to have negligible effect, since the time period (20 to 40 s) of core melt spreadingis very short; or they have been shown to be bounded by other phenomenological and scenario uncertainties.

The RIT method, first developed for spreading in one-dimensional channels, has recently been extended to describe spreading in two-dimensional channels and, more importantly, for spreading into open area. In the RIT method, the terminal spread melt thickness δ_s is shown to be a function of the time scales of two competing processes: hydrodynamic (convective) spreading τ_{conv} and solidification τ_{sold}. In the gravity-inertia regime, the hydrodynamic spreading time scale τ_{conv} is determined as the time period required for liquid (melt) to spread to reach its capillary thickness, δ_{cap}. The characteristic solidification

time, τ_{sold}, is defined as the time period needed to cool the melt to an immovable state. For this, not only the superheat, but also a part η of the latent heat of fusion, has to be removed from the bulk melt.

Based on the mass and momentum conservation equations, a square-root relation was established between the dimensionless length scale (representing ratio δ_s/δ_{cap}) and the dimensionless time scale (representing ratio τ_{conv}/τ_{sold}). The square-root law was shown to be valid in both gravity-inertia and gravity-viscous regimes, employing a dimensionless viscosity number, which was analytically derived.

2.5.2 Methodology validation

An experimental program named scaled simulant spreading experiments (S3E) was performed at RIT. The S3E data were analyzed and found to fit very well with the scaling rationale developed. The RIT method was then used to predict the spreading distance in one-dimensional high-temperature oxidic melt spreading tests at RIT. Very good agreement between the pre-test prediction results and data was obtained. The validation success confirmed assumptions made in deriving the model equations (e.g., η = 0.5) and justified the use of heat transfer correlations employed.

Extensive validation of the RIT method was performed against experimental data from KATS, COMAS, VULCANO and FARO spreading experiments. The method was found to predict, with reasonable accuracy, the spreading distance in one-dimensional spreading channels and spreading into two-dimensional channels (COMAS EU-4, VULCANO and FARO L-26). It was also found that the spreading in two-dimensional channels bounded by the channel's side walls is essentially one-dimensional. It should also be noted that the RIT method was employed to perform pre-test predictions for COMAS EU-2b core melt spreading experiment. Excellent agreement between the predicted and observed spreading distance was obtained. In general, it can be concluded that the phenomenology of one-dimensional melt spreading is reasonably well understood.

Validation of the RIT method for melt spreading into open area was also performed on the data base obtained from the RIT simulant-material experiments. It was found that the open-channel flow theory performs best in evaluat-

ing the convection time scale used in the scaling model. Further validation can be performed when new data on core melt spreading into open area becomes available. At this point, it should be noted that melt spreading into an open area is significantly different from the one-dimensional spreading. As melt spreads in all directions, the hydrodynamic spreading time scale is remarkably reduced, and hence the spreading area is significantly enhanced. As a result, the spread melt thickness in the open-area spreading case should be significantly less than that obtained with one-dimensional spreading process. Consequently, with two dimensional open area spreading (as in EPR) it appears to us that the melt will cover the whole area quite uniformly.

The methodology developed at RIT is employed to predict the core melt spreading characteristics in the EPR melt retention device. Although the prototypic situation is of spreading into open area, both the RIT method for spreading into an open area and the RIT method for one-dimensional spreading are employed. The latter to provide the conservative lower bound estimate of the spreading area.

The assessment was performed for two basic cases, with minimum (case A) and maximum (case B) amount of sacrificial concrete slag added to the oxidic corium before spreading. In addition, owing to the higher viscosity of the core melt-concrete slag mixture, a lower range of core melt discharge rate was chosen for a conservative evaluation of the spreading characteristics in case B. For the base selected cases, it was found that even the one-dimensional spreading model predicts complete spreading ($A_{theo}/A_{EPR} \approx 0.85$ .. 1). The spreading-into-open-area model predicts that $A_{theo}/A_{EPR} \geq 6..8$. The lower numbers (0.85 and 6) of the calculated spreading efficiency are for case B. Results of the sensitivity analysis indicate that the total melt mass and melt discharge rate are the important parameters. However, within the range of these parameters investigated, scenario and phenomenological uncertainties were found to have no profound impact on the results of the assessment.

Chapter 3

Investigation of Re-Spreading Phenomena

3.1 Introduction and Background

In the current accident management and melt stabilization approach for the European Pressurized water Reactor (EPR) [13], the core melt discharged from the failed vessel is assumed to accumulate in an intermediate retention crucible made of a special concrete. Interactions between decay-heated core melt and concrete lead then to the concrete ablation and rupture of the crucible bottom, therefore, the mixture of molten corium-concrete is discharged to spread through a short slope on a two-dimensional spreading area. The time period required for failure of the intermediate crucible bottom should ensure relocation and accumulation of a major part of reactor core melt in the crucible from the moment of vessel failure.

The issue addressed in this work is whether an initially spread-and-stopped, uncooled and crusted mass (layer) of corium will re-spread earlier than it would get buried into the concrete substrate. There is the race: the internally-heated corium mass can break the crust and re-spread in the X-Y plane, or keep ablating the concrete and go downward (-Z) direction. The scenario of concern is that in which either the melt mass flow rate or the total melt mass (at the time of spreading initiation) is not large enough to spread the melt mass over the whole

area of the basemat or of the spreading chamber (for the EPR). In this work, the re-spreading is investigated in X-Y plane aspect, since much work has been performed on the concrete ablation of a crusted mass of melt (BETA tests at Karlsruhe [54], ACE and MACE tests at ANL [61],[55], SURC tests at SANDIA [60]) etc. These data provide the rate of downward ablation of corium into concrete at various temperatures of the crusted melt pool. The ablation rate is a direct function of the melt temperature. Near the end of the MACE test when the melt pool temperatures were low, although above the concrete ablation temperature, the rate of concrete ablation (or the rate of downward movement of melt mass) is only a few millimeters/hour.

An investigation on respreading phenomena have been performed, both, experimentally and analytically. The objective of this work was to perform small scale experiments, observe the respreading process and develop a model which could describe the experiments well; and then use it for prototypic accident situations. A series of experiments at intermediate temperatures have been performed with simulant materials to obtain data necessary for model development and validation.

3.2 Experimental Study

The purpose is to investigate the rate of attack of an internally heated melt on its crust, and the location and the mode of the failure of crust. Another objective is to determine whether, and how, the whole melt pool (inside the crust boundary) will re-spread or only a part of it will re-spread.

The RIT/NPS experimental program is named RESCO (Re-Spreading and Coolability) and employs simulant materials as working fluids. In the re-spreading test series the intermediate temperature non-eutectic salt mixture 20%$NaNO_3$-80%KNO_3 (T_{sol} = 220^{o}C, T_{liq} = 280^{o}C) and the eutectic salt mixture 50%$NaNO_3$-50%KNO_3 (T_{liq} = 220^{o}C) were employed as core melt simulants to investigate the timing, location and mode of crust failure. It should be noted that the mixture was selected owing to similarity of its phase diagramm, as shown in Figure D.1 (App. D), to that of the prototypic binary-oxide core-melt mixture UO_2-ZrO_2.

Experiments were performed in the RESCO facility of RIT/NPS in an open

atmosphere.

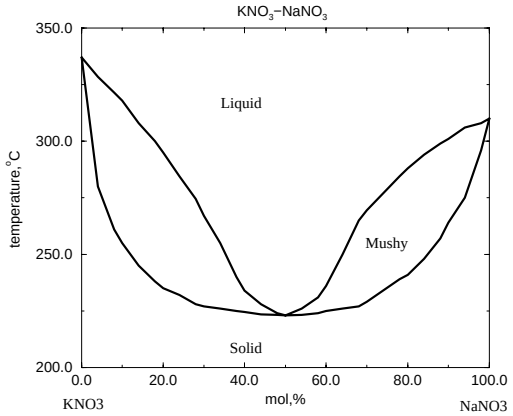

Figure 3.1: Phase Diagram of the Binary $NaNO_3$-KNO_3 Salt Mixture

3.2.1 Experimental Results

The objective of the re-spreading related research at RIT/NPS is to delineate the effect of different scenarios on the crust break-up location and the corresponding times. The following scenarios were investigated:

- different initial cooling times (different initial crust thicknesses)
- different power supply (different internal heat generation)
- different top boundary conditions (radiation or no radiation from the top)

Twelve intermediate temperature re-spreading experiments were performed, employing both the binary eutectic and non-eutectic salt mixture as working fluid. Experimental conditions of these re-spreading tests are given in Tables D.1 and D.3.

The first comparison can be made for tests with different top boundary conditions, i.e. with or without the radiation from top. The RESCO-S1 and RESCO-S2 tests have similar initial superheats, similar initial cooling times

and same remelting heats (see Table D.1). As shown in Table D.2, the remelting time is more in the case of cooled top boundary due to larger crust thickness. The location of the beginning of the crust break-up in cases with insulated top boundary was always at the very top of vertical crust layer, where as, in the cooled top case it is 1-2 cm lower (see for example Figure D.3). The same results were obtained with the eutectic salts, RESCO-E3 and RESCO-E4 (see Tables D.3 & D.4). The differences in the crust shape between the two different boundary conditions are shown in Figures D.4 and D.5.

The second comparison is made for crust break-up location and time of failure for different cooling times. It was found that the remelting time is a direct function of the crust thickness, but it did not lead to any change in the vertical direction, as given in tables D.2 & D.4 (for tests, RESCO-E4 and RESCO-E5).

The final comparisson was made between the tests with different internal heat generation rates, the RESCO-S2 and S7 tests, RESCO-S2 and S6 tests, RESCO-E1 and E3 tests, as well as, RESCO-E2 and E5 tests. The reduction of power by a factor of two results in melting times getting increased, although by different magnitudes for eutectic salt and non-eutectic salt.

For the non-eutectic salt, it changes by factor of four where as for eutectic salt, it changes by a factor of, approximately two, about the same as the reduction of power. In the non-eutectic salt case the presence of mushy layer controls the erosion of the solid-liquid interface during the reheating process in sharp contrast to the eutectic case. The convective velocities in a mushy layer would depend on the solid fraction in it and hence can considerably slow down in the low heat flux case.

Some differences in solidification and melting processes between the eutectic and non-eutectic experiments can be envisaged due to the presence of the mushy layer. The fluid mechanics of mushy layers is quite different from that of liquid regions [62]. In principle, a mushy layer is a porous medium through which the interstitial melt can flow, however, the permeability structure of the mushy layer is not known. The difference in density between solid and liquid drives a non-solenoidal flow of the interstitial fluid within the mushy layer, even no external forces are acting. There are two significant consequences of the transport of solute by such a flow. One is that the porosity, and hence the permeability, of the layer is altered, which has important implications for the onset of natural convection within the interstices, for example. The other is that

it causes macro-segregation in the mixture that cannot be eliminated by forming the solid in microgravity, since it is intrinsic to the solidification itself [58].

More over, the thermosolutal convection in the mushy layers have a strong influence on the solidification process in that, they modify the temperature field and hence the final solidified structure. For example, they lead to the erosion and remelting of solid dentrites during solidification thus afffecting the final crust thickness [56]. In essence, the presence of a mushy zone can present us with a very different crust morphology, in the case of non-eutectic salts when compared to that with an eutectic salt.

The results of few non-eutectic and eutectic tests RESCO-S5 and RESCO-E1, RESCO-S3 and RESCO-E2, RESCO-S4 and RESCO-E4 with similar experimental conditions can be compared. Due to the lower heat of fusion energy for non-eutectic salt mixture (Table F.5) the solidification process could be somewhat faster,initially. However, the final crust thickness, where temperature is less than T_{sol} ($\simeq$ 493 K, Table F.5), was thinner than in corresponding eutectic case, due to the above mentioned reasons (see Figures D.6 and D.14). Finally, it led to reduction of the remelting times in non-eutectic tests in comparisson to those for the eutectic, Tables D.2 and D.4.

The main observation that could be drawn from these experiments was that the crust failure location was always at the *upper part* of the vertical crust layer, irrespective of the test conditions and the non-eutectics remelt *faster*.

3.3 Analysis of experiments

The experimental results were analyzed with MVITA (Melt Vessel Interactions - Thermal Analysis) code, which was developed, validated and employed earlier for reactor predictions at RIT [51]. Studies have been performed to develop and validate a simple model of natural convection heat transfer in heat-generating pools, in which only the heat conduction equation is solved over the pool domain, and the effect of natural convection flows is accounted for by effective directional conductivities. A fixed grid enthalpy approach is used in this code to incorporate the phase change (for details see [57]). The mushy region is modelled as a conduction dominated region with a conductivity in between the solid and the liquid. This is formulated as an **Effective Conductivity-Convectivity**

Model (ECCM).

3.3.1 Solidification and remelting modeling

Performance of all RESCO tests consisted from two parts: solidification and remelting parts (beginning of failure), and both of them were examined using MVITA code.

The calculated results are presented in Figures together with the experimental data. It can be seen that a reasonable agreement between the calculated and measured results was achieved for the upper part of the cavity near the sidewall, while differences exist in the lowermost region near the side wall. This is due to the fact that interaction between the vertical boundary layer and the cavity's bottom surface, as well as with the stagnant liquid layer at the lower part of cavity was not taken in to account in the present model, since Nu_y presents the heat transfer across the one-dimensional free boundary layer along an infinite heat-exchange surface. The stagnant region is always present at the bottom of a cavity undergoing convection with internal haeting. In addition, the laminar boundary layer model can not adequately describe the heat flux distribution in case of transition to turbulence ($Ra = 3.71 \times 10^{13}$). For $Ra_y > Ra_{y,transition}$, the turbulent heat transfer correlation ($Nu_y \sim Ra_y^{1/3}$), developed for turbulent boundary layer, should be used. In the turbulent part of the vertical surface, the local heat flux distribution is uniform, *i.e.* independent of y. More over, in the non-eutectic tests (the -S tests), the presence of convection can dissolve the solidifying dentrites and hence, the temperature profile. It must be noted, however, that the mushy region is modelled as a conduction region with an average conductivity between those of liquid and solid.

As, some of RESCO experiments have been performed with both the side wall and the top surface being cooled, the internally-generated heat has to be removed through the isothermal vertical and horizontal boundaries. For this case, both the concepts of effective velocity, and effective heat conductivity, have to be employed in order to describe the heat transport in the cavity. In the present analysis, the model of laminar boundary layer (along the vertical wall) is applied to calculate the effective horizontal heat conductivity k_x.

Comparison of the calculated results with the experimental data shows that

the model is capable of providing the distributions of the heat removed through the top and side wall of the cavity (see Figures D.10, D.11, D.12, D.13, D.15, D.17).

The shape of the crust, before and after the re-melting, can be viewed through the isotherm plots. Representative contour plots are shown in Figures D.18 & D.19.

Table 3.1: Salt mixture properties used in calculatons

Property	Eutectic		Non-eutectic	
	solid	liquid	solid	liquid
	1925		1925	
Conductivity, $W/(mK)$	0.459		0.439	
Specific heat, $J/(kgK)$	1236	1320	1328	1369
Latent heat, J/kg	100200		58730	
Melting point, K	493		553	
Mushy zone, K	0		60	

3.4 Summary

Focus was placed on obtaining data on crust re-melting, failure location, failure area development and the resulting re-spreading of molten materials. We believe that the governing mechanism of this phenomena is solidification and re-melting driven by natural convection.

A number of simulant material re-spreading experiments were performed using fluids with different phase change behavior and properties. It was found in all the tests that the crust failure location is at the upper part of the vertical crust layer.

Analysis of the experiments was performed with MVITA code. Experimental and calculated results are in reasonable agreement with each other.

The present study indicates that natural convection of the self-heated melt contained within a crust vessel will be the controlling phenomenon for crust re-melting and break-up. The break-up location will be high due to the shape of

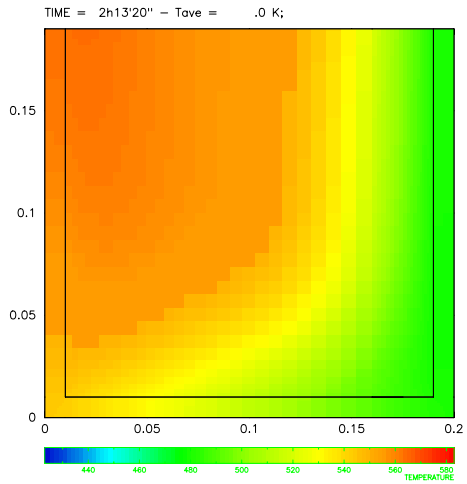

Figure 3.2: Modeling of the crust formation with no radiation from the top

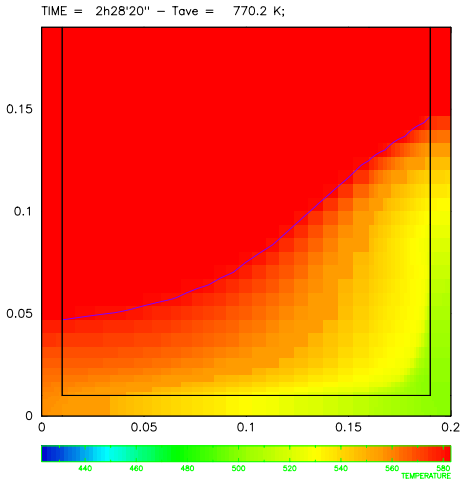

Figure 3.4: Modeling of the crust break-up with no radiation from the top

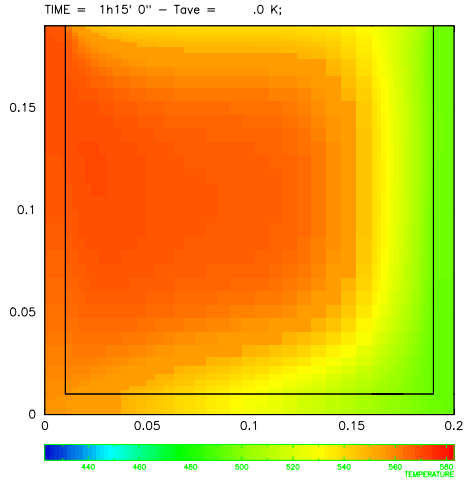

Figure 3.3: Modeling of the crust formation with no radiation from the top

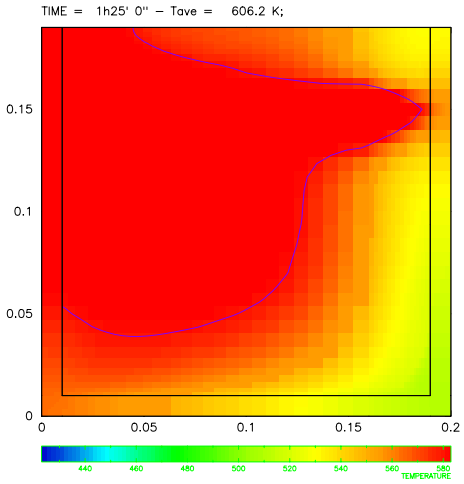

Figure 3.5: Modeling of the crust break-up with radiation from the top

the crust it attains during solidification along the vertical wall and subsequent erosion by natural convection. These results are in conformity with the observations obtained from TMI-2 accident on the break location of the crust in the in-vessel melt pool, which was immersed in water.

Chapter 4

Porous Media Coolability

4.1 Dryout Heat Flux

4.1.1 Introduction and Background

Coolability of a heat-generating porous beds has been of concern, since the LMFBR days. In the LWR severe accident scenario, particulate debris beds are formed when corium melt comes in contact with water. This may occur in-vessel in the lower head when melt is discharged from the core to the lower head (e.g. TMI-2), and, may occur ex-vessel, when melt is discharged from the vessel failure site to the containment. Some containment cavities are designed to remain dry (German PWR), however most others will have varying depths of water. The Swedish BWRs, in particular, employ the severe accident management (SAM) scheme in which a deep water pool is established in the lower dry-well to fragment the melt into, hopefully, a coolable debris bed. The melt-water interaction scenario will, most probably, produce a stratified bed, quite akin to that found in the FARO tests [63]. The small size particles will be lifted, by the steam produced, into the containment atmosphere and will later on deposit as a dense layer on top. The dryout heat flux as the limiting parameter for steady state removal of the decay heat by boiling of the coolant has been the subject of many theoretical and experimental investigations during the last two decades. The long-term coolability of debris beds is eesential to keep the bed

temperatures below the melting temperatures of the bed.

An early theoretical and experimental study of the thermalhydraulic characteristics of single phase flow through a volumetrically heated porous layer is that of Choudhary and El-Wakil [64]. They solved the coupled linear energy equation for the solid and gas phase using an implicit modified Crank-Nicholson method.

Dhir and Catton [65] made experimental observations of the dryout heat fluxes for inductively heated particulate beds cooled from the top. This study dealt with two bed configurations, shallow and deep. Different mechanisms for the dryout in these beds were identified. It was concluded that the deep bed dries out at a particular section primarily in the lower regions of the bed where gravity can no longer maintain the flow rate necessary to compensate for the evaporation rate, or, in other words, when the evaporation rate is greater than what can be sustained by the average downward superficial velocity of the coolant. Some semi-theoretical correlations based on the proposed hydrodynamic models were developed and validated.

Vasiliev and Mairov [66] analyzed heat transfer, pressure drop and stability characteristics of a volumetrically heated porous layer cooled with forced flow evaporation. Depending on the physical properties of the coolant , they divided the porous layer into three regions - subcooled, saturated two phase mixture and superheated steam. For each region, they solved the energy equations with appropriate boundary and interfacial conditions to obtain temperature distribution in the solid and the fluid. But the of flow direction in this study is normal to the body force, whereas in physical situations of interest in reactor safety, the gravity acts in a direction parallel to the flow.

Later, Naik and Dhir [67] experimentally investigated a volumetrically heated porous layer with coolant flowing through that. The purpose of this work was to obtain the data for the steady state temperature profile and pressure drop of an evaporating two-phase coolant flowing vertically. A model for the temperature profile, based on the solution of the one-dimensional energy equations for the particles and the coolant with assumption of no differences between the solid and liquid temperatures, was developed. The two-phase pressure drop was evaluated by a separated flow model based on the empirical relations obtained from the experiments. In this model, the void fraction was correlated as a function of the flow quality and mass flow rate. The model worked reasonably well

for water-steam at atmospheric pressure, however not as well for fluid mixtures with a higher vapor/liquid volume ratio.

Hofmann [68] presented the results of experimental and analytical investigation on dryout heat flux in inductively heated beds for, both, top and top-and-bottom fed conditions. His model, which calculates the heat flux as a function of the saturation by solving the conservation equations for momentum, mass and energy, gives a saturation distribution for dryout condition. But no satisfactory comparison was achieved with experimental data.

Considerable interest was generated in employing hydrodynamic models for predicting dryout, since, clearly, counter-current flooding generally controls dryout in porous media made up of large size particles. Several experimental and analytical studies on hydrodynamic aspects of two-phase flow through porous media were performed, as summarized by Schulenberg and Müller [69]. It is unfortunate that most of these studies were carried out for the idealized condition of a one-dimensional homogeneous porous layer, whereas those encountered in actual practice are multi-dimensional and may be composed of regions with widely varying permeabilities and heating conditions.

Tsai in [70] measured dryout heat fluxes in axi-symmetric porous layers with partial volumetric heating. His numerical solution was obtained by a finite difference scheme without the interfacial drag term. Capillary pressure was included in his solutions through the use of the Lawrett function. In this work the solutions were obtained with ”pseudo stream functions” to include the source terms due to the volumetric heating. But such an approach exists only for certain distribution of volumetric heating in the porous layers.

A hydrodynamic model was developed by Tung and Dhir [71] to predict void fractions and pressure gradient for one-dimensional two-phase flow through porous media. The particle-gas drag, particle-liquid drag and liquid-gas interfacial drag were evaluated theoretically for the flow configurations associated with different flow regimes. The drag models were then employed in conjunction with force balances on the two phases to obtain the void fraction and pressure gradient as functions of liquid and gas superficial velocities. This mechanistic model was modified and solved numerically in [72] by the same authors. The numerical scheme, based on the finite element model, called for elimination of velocities in favor of pressure and void fraction to predict dryout heat flux. The finite element model allowed the existence of several regions of different

permeabilities in the domain. Solutions were obtained both in two-dimensional cartesian and in the axi-symmetric coordinate system.

The modeling approach of channeling of self-heated particle beds is exemplified by the Lipinski model [73]. It was assumed in this model that the vapor pressure at the bottom of a channel is sufficient to offset the weight of the overlying particles plus liquid and the flow resistances in the channeled region are neglegible. Later on, Lipinski [74] introduced the idea of a sticking factor S_f, which means that the vapor pressure must be S_f times the overlying bed pressure at the bottom of a channel. However, it appears that a nondimensionalization of this sticking pressure leads straightforwardly to the sticking factor concept. The sticking factor model relies upon the analysis of the motion of particles caused by the upward displacement of a piston through the bed. Such a simulation is regarded as representative of the onset of channeling. Stubos and Buchlin [75] extended Lipinski's model by applying a force balance to a single bottom particle which included the weight of the overlying particles and the friction force. In details, they investigated [76] the behavior of vapor channels traversing the upper part of a boiling, unconstricted, homogeneous debris bed and suggested a theoretical model for the dryout heat flux in a channeled bed. A multi-dimensional mathematical model for numerical analysis was developed and presented in [77] by Stubos and Buchlin assuming local thermal equilibrium (LTE) between the solid and liquid phases (thermally homogeneous medium). But this assumption may not be satisfactory for the step change problems in which, during the early stages of the transport processes there may be considerable differences between the temperatures of the flowing fluid and solid particles. This is also true even during the later stages of the transport processes in high speed flows in which the fluid to solid interaction time may not be large enough to bring the temperatures of the fluid and solid phases close enough for LTE to be a reasonable assumption.

Non-thermal equilibrium flow through a porous bed is a subject of essential interest. Sözen and Vafai [78] presented a general set of volume-averaged governing equations for non-thermal equilibrium condensing forced flow through a latent heat storage porous media and comprehensive numerical investigations of the phenomenon were carried out. Kuznetsov [79] made such an analysis based on solution, by the perturbation technique, of the full energy equations for incompressible fluid and solid phases, without neglecting any terms in the equations. He showed that the temperature between the fluid and solid phases in a semi-infinite packed bed forms a wave localized in space. Later on, he

investigated [80] the thermal behavior of the three-dimensional porous bed during non-thermal equilibrium fluid flow through it, with assumption of constant thermal, physical and transport properties.

The present work describes the determination of the dryout location by introducing initial thermodynamic perturbations which, if they grow, will lead to a temperature escalation at a specific location. An analysis of the steam thermal behavior in the two-dimensional homogeneous and stratified porous beds with temperature dependent thermal conductivity coefficient has been performed.

4.1.2 Experimental Study

An experimental investigation named POMECO (POrous MEdiia COolability) on dryout heat flux of a particulate bed was performed. Both homogeneous and stratified debris beds were recently employed at RIT and some results were reported [81].

The objectives of the POMECO program are to provide the data base and the models to resolve the following issues:

- Is a deep, stratified, low-porosity, bed coolable at low pressure in a deep pool of water?
- Can the dryout heat flux be enhanced, i.e. coolability potential enhanced?
- What are the feasible back-fits and what is the enhancement in the dryout heat flux?

Focus is placed on low porosity, small particle size and relatively large scale debris beds. Bed stratification is an important parameter for investigations. Most debris bed coolability experiments have been performed with steel balls of different size, generally heated by induction. We have taken a different approach. Since corium debris have a particle size distribution and are more like sand, our debris beds were built with sand of different particle size distributions, heated with a network of thin heaters, distributed uniformly in the sand bed to produce uniform volumetric heat generation. The experiments were conducted on low porosity beds, since they are the most difficult to cool with top

flooding. For enhancement of the dryout heat flux, we reasoned that since water addition from bottom has been shown to be a more efficient mode of cooling in earlier experiments, as well as in the COMET experiments [82] for melt coolability, water should be channeled to the bottom of the debris bed. A similar approach was proposed by late Prof. Becker of RIT [83], who performed some small scale scoping experiments. The downcomer(s) were built in the debris bed which would channel the water from the water overlayer to the bottom of the bed and develop a two phase natural circulation flow loop, providing greater mass flow rate in the bed. The following parameters were varied in the experients: (i) the downcomer flow area, (ii) downcomer geometry, e.g. with holes along bed height.

Experimental facility

The schematic of POMECO facility is shown in Figure 4.1 and described in more detail in [81]. The POMECO facility consists of water supply system, test section, heater system, measurement and DAS systems.

Different size sand particles are chosen to construct the porous particle bed with different characteristics, e.g. mean particle size, porosity, and stratification. The top surface of the particle bed is covered by grids with small size holes to avoid channel formation in the particle bed and fly off of small sand particle.

The test section is a stainless steel vessel whose details are presented in Fig. 4.1. The cross-sectional area of the test section is 350×350mm rectangular. The height of the lower part is 500 mm and the height of the upper part is 900 mm. The maximum height of the sand can be 450 mm. A porous plate was placed 50 mm above the bottom of the test section to provide enough space for the water coming from the downcomer, for disribution into the sand bed. It is a 350×350 stainless steel plate, in which there are about 100 holes with a diameter of 10 mm. The downcomer fixed to the porous plate is a tube of stainless steel with 500mm height and 30 mm internal diameter, it is fixed on the porous plate. Later, the downcomer was drilled with holes along vertical direction, and then, this number of holes was doubled. Before the sand bed is formed, a grid is placed on this porous plate in order to prevent fine sand particles from falling into the bottom space. A water level gauge is installed in the upper part of the test section to monitor the water level variation during the

experiment.

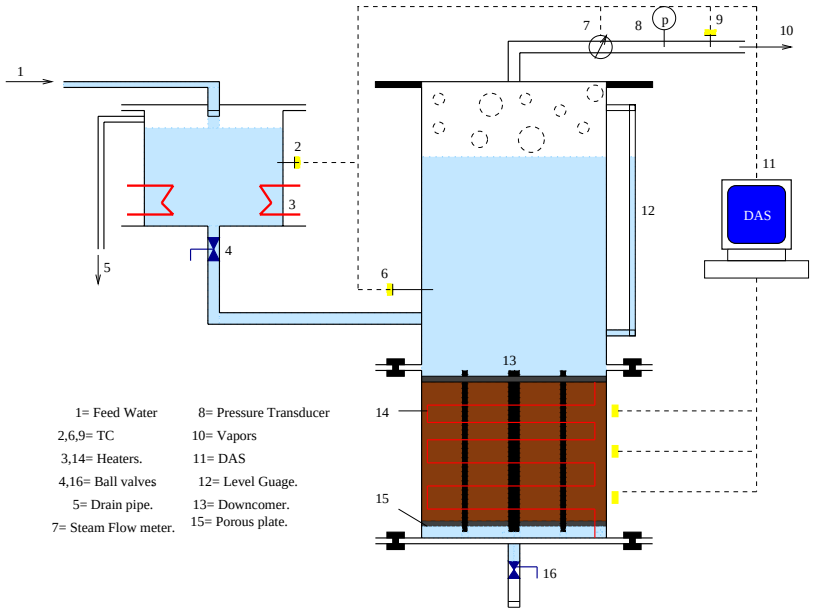

Figure 4.1: Schematic of the POMECO facility.

4.1.3 Experimental results and discussion

Six series of experiments were performed for both homogeneous and stratified particle beds. The effects of porosity, mean particle size, and stratification of the particle bed on the dryout heat flux have been measured. The first test series (Homo-1.1, -2.1, -3.1 and Strat-1.1, -2.1, -3.1, -4.1) was conducted without downcomer, the second (Homo-1.2, -2.2, -3.2 and Strat-1.2, -2.2, -3.2, -4.2) with the downcomer, the third (Homo–3.3 and Strat-1.3, -2.3, -3.3, -4.3) with the downcomer with the holes, the fourth (Homo–3.4 and Strat-2.4, -4.4) with the downcomer with twice the number of the holes, the fifth (Homo–3.5 and Strat-2.5, -4.5) with four additional downcomers, which increase the total flow area by a factor of two and the sixth (Homo–3.6 and Strat-2.6, -4.6) with four downcomers to investigate the influence of the change of downcomer geometry with no change of the flow area.

Three homogeneous sand particle beds are tested, in which the porosities of the particle beds are varied from 0.258 to 0.397, the mean (mass-averaged)

particle sizes are smaller than 1 mm.

Table 4.1: Experimental results for homogeneous particle beds.

Test Number	**Sand Bed Type**	**Dwcm**	**Dryout h. flux KW/m^2**		**Enhanc. by dwcm** %
			Exp.	**Lipinsky Model**	
Homo-1.1	Porosity = 0.4, D_{mean} = 0.2mm	No	90	23	
Homo-1.2	same as Homo-1.1	Yes	183		104
Homo-2.1	Porosity = 0.36,	No	222	215	
Homo-2.2	same as Homo-2.1	Yes	331		49
Homo-3.1	Porosity = 0.26, D_{mean} = 0.8mm	No	111	100	
Homo-3.2	same as Homo-3.1	Yes	202		82
Homo-3.3	same as Homo-3.1	Yes	200		80
Homo-3.4	same as Homo-3.1	Yes	258		132
Homo-3.5	same as Homo-3.1	Yes (5)	313		182
Homo-3.6	same as Homo-3.1	Yes (4)	209		88

Table 4.1 shows the experimental results on the dryout heat flux for the homogeneous particle beds both with and without a downcomer. The predictions of dryout heat flux by Lipinski's zero-dimension model [73] for the particle bed without a downcomer are also listed in this table. It seen that except for the particle beds with very small mean particle sizes (test Homo-1.1) the experimental results on dryout heat flux agree quite well with the predictions by Lipinski's model. For the test Homo-1.1, the experimental result on dryout heat flux is much higher than the prediction by Lipinski's model, even though the porosity is not low. This indicates that either the Lipinskimodel does not extend to mean particle size of 0.2 mm or for these small particle beds, capillary force contributes substantially to the flow in the bed.

From Table 4.1 it can also be seen that there is a large enhancement of the dryout heat flux by the downcomer, the natural circulation flow that gets established. Water is channeled to the bottom of the particle bed through the downcomer. The dryout heat flux consists of two parts: one is the contribution from the water penetrations from the top of the particle bed, which is governed

Table 4.2: Experimental results for stratified particle beds.

Test Number	**Sand Bed Type**	**Dwcm**	**Dryout h. flux KW/m^2 Experiment**	**Enhanc. by dwcm** %
Strat-1.1	U. layer: H = 130 mm Porosity = 0.4, D_{mean} = 0.2mm L. layer: H = 240 mm Porosity = 0.36, D_{mean} = 1mm	No	87	
Strat-1.2	same as Strat-1.1	Yes	186	113
Strat-1.3	same as Strat-1.1	Yes	210	140
Strat-2.1	U. layer: H = 130 mm Porosity = 0.26, D_{mean} = 0.8mm L. layer: H = 240 mm Porosity = 0.36, D_{mean} = 1mm	No	54	
Strat-2.2	same as Strat-2.1	Yes	138	157
Strat-2.3	same as Strat-2.1	Yes	212	295
Strat-2.4	same as Strat-2.1	Yes	226	321
Strat-2.5	same as Strat-2.1	Yes (5)	319	494
Strat-2.6	same as Strat-2.1	Yes (4)	114	112

by counter-current flooding limitation (CCFL) and is the dryout heat flux of the particle bed without a downcomer; the second is the contribution from the heat transferred to the water channeled to the bottom of the particle bed through the downcomer.

The experimental results show that larger enhancement of dryout heat flux by the downcomer occurs for the particle beds with fine particles or will low porosity. This clearly indicates that the capillary force contributes to the driving head of the natural circulation in the pool. The provision of a downcomer to channel the coolant to the bottom of the bed has a significant effect on the dryout heat flux.

Table 4.3: Experimental results for stratified particle beds (cont.).

Test Number	**Sand Bed Type**	**Dwcm**	**Dryout h. flux KW/m^2 Experiment**	**Enhanc. by dwcm** %
Strat-3.1	U. layer: H = 240 mm Porosity = 0.4, D_{mean} = 0.2mm L. layer: H = 130 mm Porosity = 0.36, D_{mean} = 1mm	No	55	
Strat-3.2	same as Strat-3.1	Yes	190	242
Strat-3.3	same as Strat-3.1	Yes	205	268
Strat-4.1	U. layer: H = 240 mm Porosity = 0.26, D_{mean} = 0.8mm L. layer: H = 130 mm Porosity = 0.36, D_{mean} = 1mm	No	122	
Strat-4.2	same as Strat-4.1	Yes	235	93
Strat-4.3	same as Strat-4.1	Yes	258	111
Strat-4.4	same as Strat-4.1	Yes	280	129
Strat-4.5	same as Strat-4.1	Yes (5)	315	159
Strat-4.6	same as Strat-4.1	Yes (4)	201	65

Focus of the stratified bed experiments is on the effects of particle bed characteristics (such as porosity, mean particle size and the thickness of the fine particle layer, resting on the top of another layer) on the dryout heat flux. In all the experiments, the lower particle layer employs the same particle configuration (mean size and porosity).

Tables 4.2 and 4.3 show the experimental results for the dryout heat flux for the stratified particle beds both with and without a downcomer. Comparing the experiments Strat-2.1 and Strat-4.1 with experiment Homo-3.1, the upper particle layer of experiments Strat-2.1 and Strat-4.1 is the same as the particle bed of experiment Homo-3.1, which has low porosity. Experimental results on the dryout heat flux in these three cases (see Table 4.1, 4.2 and 4.3) show

that stratification of the particle beds does not decrease the dryout heat flux. This observation is different from the analytical model and the experimental observation of Lipinski.

The thickness of the fine particle layer has different effect from that of low porosity. Comparing the particle bed configurations of Homo-1.1, Strat-1.1 and Strat-3.1, and experimental results on dryout heat flux for these three experiments in Table 4.1, Table 4.2 and Table 4.3, it appears that the stratification decreases the dryout heat flux a little. The decrease of the dryout heat flux may be caused by the reduction of the porosity at the interface between the layers. However, when the particle size of the upper layer is very small, the capillary force may increase the water penetration flow. Therefore, the thickness of fine particle layer has little effect on the dryout heat flux.

It can also be seen in Tables 4.2 and 4.3 that the effect of the downcomer on the dryout heat flux is significant. The downcomers can enhance the dryout heat flux from 50 to 600%. Greater enhancement occurs with larger downcomer flow area, as it can be seen from the fifth test series. The sixth test series showed that changing the downcomer geometry with no change of the flow area does not modify the increase in the dryout heat flux.

4.2 Analysis

4.2.1 Mathematical formulation of the problem

Figure 4.2 depicts the schematic diagram of the problem under consideration. A two-dimensional self-heated porous packed bed, wich consists of k homogeneous layers, is filled with the fluid, which moves from the bottom to the top, and is initially at an uniform temperature. In establishing a model for analyzing this problem, the following assumptions were employed:

- The fluid phase is single phase and is compressible (steam)
- The particle sizes are significantly larger than molecular-kinetic sizes, but they are significantly less than characteristic size of the system

- The physical properties such as thermal conductivity coefficient, dynamic viscosity etc. are temperature dependent
- Solid particles are immovable and porosity is constant in each layer

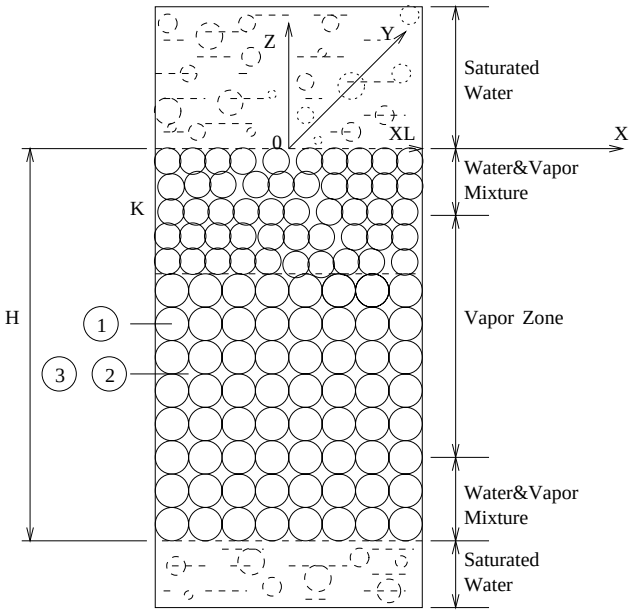

Figure 4.2:

Employing the equations of the saturated granular layer which were introduced by Nigmatulin [84] and then developed by Kazachkov [85] for two-dimensional case; the mathematical model of this system can be presented as follows:

Mass balance equation

$$\frac{\partial \rho_1^o}{\partial t} = -\rho_1^o(\frac{\partial u_1}{\partial x} + \frac{\partial w_1}{\partial z}), \tag{4.1}$$

Momentum equations

$$\rho_1 \frac{\partial \vec{v}}{\partial t} + \nabla p_1 + (\rho_1 + \rho_2)\vec{g} = \nabla \sigma_k, \tag{4.2}$$

$$\rho_1^o(1+0.5\alpha_2)\frac{\partial \vec{v}}{\partial t} + \nabla p_1 + \mu_1 \frac{\vec{v}}{K_0}(\frac{\alpha_1}{\alpha_{10}})^{-n} + \rho_1^o \vec{g} = 0, \tag{4.3}$$

$Energy\ equations$

$$\rho_1 C_{v1}(\frac{\partial T_1}{\partial t} + \vec{v}\nabla T_1) = \alpha_1 R T_1 \frac{\partial \rho_1^o}{\partial t} + \nabla(k_1 \nabla T_1) + Q_\Sigma + Q_V + \tag{4.4}$$
$$+\mu_1(u_1^2 + w_1^2)\frac{\alpha_1}{K}$$

$$\rho_j C_j \frac{\partial T_j}{\partial t} = \nabla(k_j \nabla T_j) + (j-3)Q_\Sigma \tag{4.5}$$

where j = 2, 3, $K = K_0(\alpha_1/\alpha_{10})^n$, $k_1 = \mu_1 \frac{C_{p1}}{Pr}$, $\frac{\mu_1}{\mu_{10}} = (\frac{T_1}{T_{10}})^m$ with Prandtl number taken at μ_{10} and m = 0.5 - 1.0.

The values with "0" indexes are taken at the fixed temperature T_{jo}. At such conditions the velocity component is calculated as follows:

$$w_1 = (\rho_1 + \rho_2 - \rho_1^o)\frac{gK}{\mu_1}$$

The above expression for the vertical velocity component w_1 corresponds, in the first order approximation, to the Darcy's law when $\rho_1^o \ll \rho_1 + \rho_2$. The Darcy's law can also be employed, when u_1 the horizontal component is much smaller in comparison with w_1 the vertical component of the velocity.

4.2.2 Boundary conditions

The initial conditions of this system are taken as following:

$$t = 0, \quad p_1 = p_1^o, \quad \alpha_1 = \alpha_1^o, \quad T_j = T_j^o$$

Later, the initial conditions may suffer perturbations, which may make them decrease or increase.

The system is symmetrical relative to the vertical axis and at the right boundary the horizontal velocity is zero:

$$x = x_L, \quad u_1 = 0$$

The condition of temperature and heat flux equilibrium at the boundary with unpermeable surrounding and with $\alpha_1 \sim \alpha_2$ and $k_1 \ll k_2$ gives:

$$x = x_L, \quad k_2 \frac{\partial T_2}{\partial x} = k_3 \frac{\partial T_3}{\partial x}$$

When we have $x = x_\infty$

$$\frac{\partial T_3}{\partial x} = 0$$

At the lower boundary $z = -H$ the temperatures are:

$$T_j = T_{jH}$$

A boiling water pool occurs at the upper layer of the system and at the bottom, hence:

$$z = 0, \quad T_j = T_{jH}$$

4.2.3 Non-dimensional formulation of the problem

The following length, time, velocity, pressure and temperature scales were introduced: H, H^2/a_2^o, a_2^o/H^2, $\mu_{10}a_2^o/K_c$ and ΔT, where ΔT is the characteristic change of temperature in the system. The equations (1) - (5) for the case $\alpha_1 = const$ can be rewritten as:

$$u_1 = -(\frac{T_{10}}{T_1})^m \frac{\partial p_1}{\partial x}, \qquad \frac{\partial \rho_1^o}{\partial Fo} = -\rho_1^o(\frac{\partial u_1}{\partial x} + \frac{\partial w_1}{\partial z}), \tag{4.6}$$

$$w_1 = (\rho_1 + \rho_2 - \rho_1^o)\frac{gK}{\mu_1} \tag{4.7}$$

$$\frac{\partial p_1}{\partial z} = Pe(\alpha_1 - 1)(1 - \Delta_2(T_2 - T_{20})) - Re_*^2 \frac{\alpha_1 p_1}{T_1}, \tag{4.8}$$

$$\begin{aligned} \frac{\partial T_1}{\partial Fo} = (1-\gamma_1)T_1(\frac{\partial u_1}{\partial x} + \frac{\partial w_1}{\partial z}) - (u_1\frac{\partial T_1}{\partial x} + w_1\frac{\partial T_1}{\partial z}) + \\ +(\gamma_1 - 1)(u_1^2 + w_1^2)(\frac{T_1}{T_{10}})^m \frac{T_1}{p_1} + \frac{\gamma_1 Pe(T_1/T_{10})^m}{\alpha_1 \kappa_a \kappa_p Re_*^2 p_1}[T_1(\frac{\partial^2 T_1}{\partial x^2} + \frac{\partial^2 T_1}{\partial z^2}) + \\ +m[(\frac{\partial T_1}{\partial x})^2 + (\frac{\partial T_1}{\partial z})^2] + \xi N u_1 T_1(T_2 - T_1)], \end{aligned} \tag{4.9}$$

$$\frac{\partial T_2}{\partial Fo} = \frac{1/(1-\alpha_1)}{1 - \Delta_2(T_2 - T_{20})}[\frac{\partial^2 T_2}{\partial x^2} + \frac{\partial^2 T_2}{\partial z^2} + N u_1 \frac{\xi}{\kappa_k}(\frac{T_1}{T_{10}})^m (T_1 - T_2)], \tag{4.10}$$

$$\frac{\partial T_3}{\partial Fo} = a_{32}(\frac{\partial^2 T_3}{\partial x^2} + \frac{\partial^2 T_3}{\partial z^2}), \tag{4.11}$$

$$Fo = 0, \quad p_1 = p_1^o, \quad T_j = T_j^o \tag{4.12}$$

$$x = x_\infty, \quad \frac{\partial T_3}{\partial x} = 0 \tag{4.13}$$

$$x = x_L, \quad u_1 = 0, \quad \frac{\partial T_2}{\partial x} = a_{32}\frac{\partial T_3}{\partial x} \tag{4.14}$$

$$z = 0, \quad T_j = T_{jH} \tag{4.15}$$

$$z = -1, \quad T_j = T_{jH} \tag{4.16}$$

where $Pe = w_o H/a_2^o$ - Peclet number; $w_o = \rho_{20}^o Kg/\mu_{10}$; $\rho_1^o = \kappa_\rho \frac{Re_*^2 p_1}{PeT_1}$; $w_1 = (1-\alpha_1)[Pe - \kappa_\rho Ra^*(T_2 - T_{20}) - Re_*^2 \frac{p_1}{T_1}](\frac{T_{10}}{T_1})^m$; $Re_v = w_o b_1/\nu_{10}$ - Reynolds number in voids; $Re_*^2 = \frac{gH}{R\Delta T}$; $Da = K/H^2$ - Darcy number; $Gr = g\Delta_2 H^3/\nu_{10}^2$ - Grasshoff number; $Ra^* = GrPr^*Da$ - Rayleigh number; $Nu_1 = 2 + 0.6Pr^{1/3}Re_v^{1/2}$ - Nusselt number; $\kappa_a = a_2^o/a_1^o$; $\kappa_\rho = \rho_{20}^o/\rho_{10}^o$; $a_1^o = k_1^o/C_1\rho_{10}^o$; $Fo = a_2^o t/H^2$ - Fourier number; $\Delta_2 = \Delta T\beta_{T2}$; $\gamma_1 = C_{p1}/C_{v1}$; $\kappa_k = k_2/k_1^o$; $a_{32} = a_3/a_2^o$; $\xi = s_{12}H^2/b_1$ - parameters of the structure of the granular layer; s_{12} - specific interface area, $b_1 = b\sqrt{2(2-\pi/3)\pi}$ - void radius, b - particle radius.

In this system three different conditions are present: non-thermal equilibrium between fluid and solid, system non-linearity and non-linearity of the physical properties. The first condition is shown by the term $\xi(T_1 - T_2)$. However,it should be noted that there is some limitation to the ξ parameter. The energy equations have the term $\xi(T_1 - T_2)$, which at the small particle sizes, big linear system sizes and, if fluid and solid temperatures are close enough,

will hold an uncertainty of the "$\infty \cdot 0$" type. The term $m[(\frac{\partial T_1}{\partial x})^2 + (\frac{\partial T_1}{\partial z})^2]$ might cause the escalation of heat processes in local space because of non-linearity of the thermal conductivity coefficient. This phenomenon was investigated by Samarsky [86] as an example of solution of the one-dimensional heat conduction problems with non-linear thermal conductivity coefficient.

4.2.4 Solution procedure

The equations (6) - (15) were solved employing the finite-difference scheme based on the split step method described by Janenko [87]. Spliting between spatial variables transformed the two-dimensional problem to two onedimensional problems:

On the lower limit of the time step

$$\frac{\partial \rho_1^o}{\partial Fo} = -2\rho_1^o \frac{\partial u_1}{\partial x}, \tag{4.17}$$

$$\frac{1}{2}\frac{\partial T_1}{\partial Fo} = (1-\gamma_1)T_1\frac{\partial u_1}{\partial x} - u_1\frac{\partial T_1}{\partial x} + (\gamma_1 - 1)u_1^2(\frac{T_1}{T_{10}})^m\frac{T_1}{p_1} + \tag{4.18}$$
$$+\frac{\gamma_1 Pe(T_1/T_{10})^m}{\alpha_1\kappa_a\kappa_p Re_*^2 p_1}[T_1\frac{\partial^2 T_1}{\partial x^2} + m(\frac{\partial T_1}{\partial x})^2 + \alpha\xi N u_1 T_1(T_2 - T_1)],$$

$$\frac{1}{2}\frac{\partial T_2}{\partial Fo} = \frac{1/(1-\alpha_1)}{1-\Delta_2(T_2 - T_{20})}[\frac{\partial^2 T_2}{\partial x^2} + Nu_1\alpha\frac{\xi}{\kappa_k}(\frac{T_1}{T_{10}})^m(T_1 - T_2)], \tag{4.19}$$

$$\frac{\partial T_3}{\partial Fo} = 2a_{32}\frac{\partial^2 T_3}{\partial x^2}, \tag{4.20}$$

On the upper limit of the time step

$$\frac{\partial \rho_1^o}{\partial Fo} = -2\rho_1^o \frac{\partial w_1}{\partial z}, \tag{4.21}$$

$$\frac{1}{2}\frac{\partial T_1}{\partial Fo} = (1-\gamma_1)T_1\frac{\partial w_1}{\partial z} - w_1\frac{\partial T_1}{\partial z} + (\gamma_1 - 1)w_1^2(\frac{T_1}{T_{10}})^m\frac{T_1}{p_1} + \tag{4.22}$$
$$+\frac{\gamma_1 Pe(T_1/T_{10})^m}{\alpha_1\kappa_a\kappa_p Re_*^2 p_1}[T_1\frac{\partial^2 T_1}{\partial z^2} + m(\frac{\partial T_1}{\partial z})^2 + (1-\alpha)\xi Nu_1 T_1(T_2 - T_1)],$$

$$\frac{1}{2}\frac{\partial T_2}{\partial Fo} = \frac{1/(1-\alpha_1)}{1-\Delta_2(T_2 - T_{20})}[\frac{\partial^2 T_2}{\partial z^2} + Nu_1(1-\alpha)\frac{\xi}{\kappa_k}(\frac{T_1}{T_{10}})^m(T_1 - T_2)], \tag{4.23}$$

$$\frac{\partial T_3}{\partial Fo} = 2a_{32}\frac{\partial^2 T_3}{\partial z^2}, \tag{4.24}$$

where α = [0;1] is an approximation parameter.

Differentials inside the two-dimensional area are approximated with the central differences of the second order:

$$\frac{\partial f}{\partial x} \sim \frac{f_n^{i+1,j} - f_n^{i-1,j}}{2h_x}; \quad \frac{\partial^2 f}{\partial x^2} \sim \frac{f_n^{i+1,j} - 2f_n^{i,j} + f_n^{i-1,j}}{h_x}$$

and on the boundary:

$$\frac{\partial f}{\partial x} \sim \frac{f_n^{3,j} - 2f_n^{2,j} + f_n^{1,j}}{2h_x}$$

Relative to "z" coordinate the same operations have to be made. To calculate differential in time the following expression is employed:

$$\frac{\partial f}{\partial F_o} \sim \frac{f_{n+1} - f_n}{\tau}$$

4.3 Examples of calculated results

In all of the POMECO tests a stable local dryout was observed, which confirmed the assumption about an escalation of temperature in space. We assumed that at high enough heat generation the governing cooling mechanism becomes steam cooling. The homogeneous and stratified POMECO tests with one downcomer were analyzed using the model presented above. The initial temperature perturbations were set as a $sine$function:

$$T_1^o(x,z) = T_{10}^o(x,z) + \Theta_1^o sink_1 x sinm_1 z$$

where $T_{10}^o(x,z)$ is the uniform temperature distribution, Θ_1^o - the perturbation amplitude, k_1, m_1 - wave numbers. Calculations were performed using the 21x51 grid.

The first examination was performed for the homogeneous test (homo-1.2) with mean particle size of 0.2 mm and porosity of 0.4. Figure 4.3 depicts the space distribution of the dimensionless temperature difference. As it can be seen, except the temperature peak, some increase in temperature near the wall was obtained. It can be explained by the the zero heat flux boundary condition, which was set at the side wall. Figure 4.5 presents the comparison between the model prediction and experimental results, they are in reasonable agreement.

Three stratified tests (strat-1.2, strat-2.2, strat-3.2) were analyzed, in which different particle layers for simulation of debris bed were employed. It should be noted that, basically, these tests are quite similar in term of porosity numbers and power density. However, there are some differences compared to the homogeneous case.

As it can be seen from the Table 4.4 the dryout locations in the tests homo-1.2 and strat-3.2 are very close, what was confirmed by calculations (Figures

Table 4.4: Dryout locations in POMECO tests with one downcomer.

Test	Dryout heat flux KW/m^2	Temperature in the dry zone, ^{o}C	Dryout location X, Z coordinate, mm
homo-1.2	186	151	X =30, Z =140
strat-1.2	187	123	X =30, Z =180
strat-2.2	138	160	X =90, Z =180
strat-3.2	190	155	X =30, Z =100

4.8 and F.10b). The bed in the test strat-3.2 consists of two layers: lower layer (130 mm height) formed from the sand particles with mean diameter of 1 mm and porosity of 0.36, and upper layer (240 mm height), which is the same as in the test homo-1.2.

Positions of dryout in the test strat-1.2 and strat-2.2 are higher than in the tests described above. In these experiments the bigger lower layers with height of 240 mm were produced from the sand particles with mean diameter of 1 mm and porosity of 0.36, which is lower than porosity of thicker layers in the tests homo-1.2 and strat-3.2. The decrease in porosity could lead to increase of the pressure drop inside the bed, because of the water supply from the bottom was the same in all experiments. The increase of the pressure drop can enhance the steam velocity and intensify cooling process, which led to movement of dryout position to the top. But due to the different compositions of upper layers in these tests the power densities, at which the beginnings of dryout were observed, were different. In the test strat-1.2 the upper layer (130 mm) was built using the sand particles with mean size of 0.2 mm and porosity of 0.4 and in this case the dryout power density was 0.5 MW/m^3. In the case of strat-2.2 the upper layer had mean particle size 0.8 mm and porosity 0.26 and this layer provided enhanced thermal resistance compared to strat-1.2, what led to decrease in the dryout power density to 0.4 MW/m^3. The results of these calculations are presented in Figures 4.4, 4.6, 4.7 and 4.9.

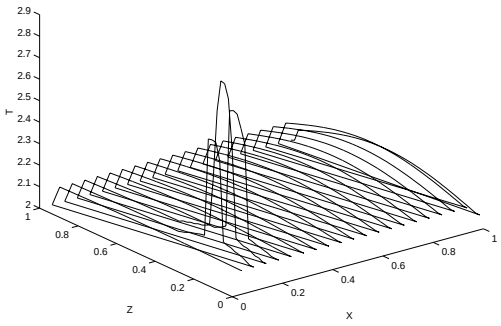

Figure 4.3: Temperature distribution in the bed (test homo-1.2) Calculations performed at the power density 0.5 MW/m^3.

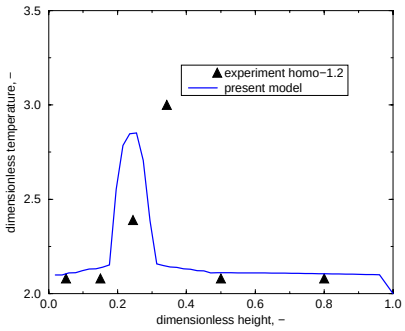

Figure 4.5: Temperature distribution along Z-axis at X=0.2

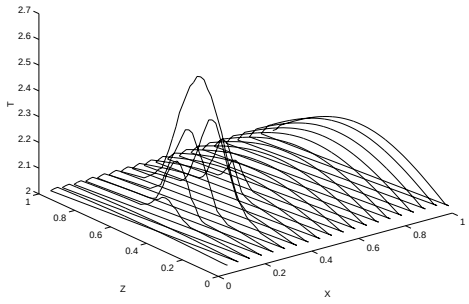

Figure 4.4: Temperature distribution in the bed (test strat-1.2) Calculations performed at the power density 0.5 MW/m^3.

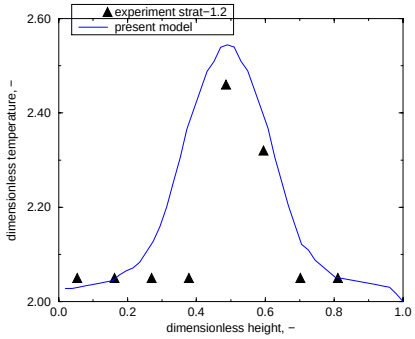

Figure 4.6: Temperature distribution along Z-axis at X=0.2

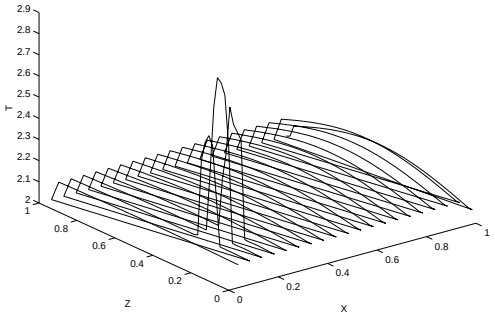

Figure 4.7: Temperature distribution in the bed (test strat-2.2) Calculations performed at the power density 0.4 MW/m^3.

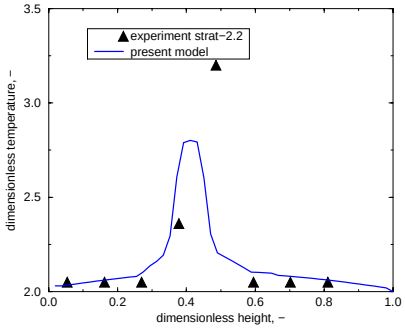

Figure 4.9: Temperature distribution along Z-axis at X=0.2

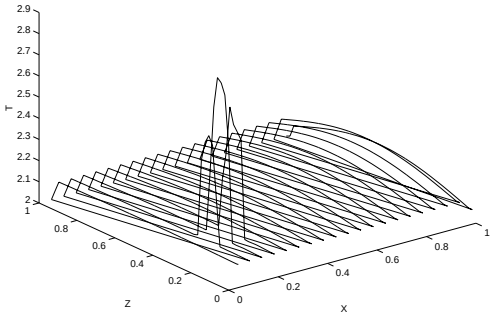

Figure 4.8: Temperature distribution in the bed (test strat-3.2) Calculations performed at the power density 0.5 MW/m^3.

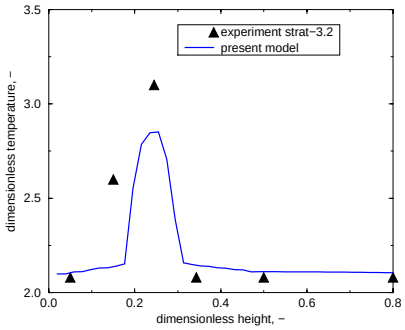

Figure 4.10: Temperature distribution along Z-axis at X=0.2

Comparison between the experimental and calculated results of the tests homo-1.2 and strat-3.2, strat-1.2 and strat-2.2 show that the thermal behavior of stratified beds is determined by the composition of the dominating layer.

4.4 Quenching

4.4.1 Introduction and Background

There are important in-vessel scenarios in which the bed dries out, and reheats; and later the water supply to the vessel is restored. For accident management purposes, it is important ascertain (a) that the bed can be quenched and (b) the steam and hydrogen generation rates. Most important is the potential to quench and the time to quench a low porosity, deep, hot particulate debris bed.

Several studies of quenching of particle debris beds either by flooding from top or from bottom have been reported in the literature. Cho and Bova [88] found that during top flooding, the penetration of liquid was faster in the middle of the particulate layer. Ginsberg at al. [89], however, concluded from their experiments that the quenching process was characterized by a two step bi-frontal process with a partial quench front propagating downward and another front traveling upward after the downward front had reached the bottom of the bed. They also proposed a model based on counter-current flooding limitation (CCFL). Tung et al. [90] experimentally and analytically studied quenching by top flooding when a certain amount of gas was injected at the bottom and heat was generated in the particles. Their model also utilized CCFL.

In particulate layers quenched by bottom flooding, there is no such CCFL limitation as with flooding from top. Studies performed by Hall and Hall [91] and Tung and Dhir [92] have shown that the rate of heat transfer is limited only by the available driving pressure or flow rate of the coolant. The heat removal process was found to be very efficient in this case. Heat removal rates as high as 8-10 times those given by counter-current flooding were observed.

The purpose of the present work is to study experimentally the quenching process in the hot homogeneous and stratified low porosity particle beds, which were quenched by, both, a water overlayer, and by injection of water from the

bottom, delivered through downcomers from the overlayer.

4.4.2 Experimental Results

Three series of quenching experiments on the POMECO test facility (figure 4.1) have been performed for both homogeneous and stratified particle beds, respectively. The quenching tests simulating debris beds have been carried out to study the effects of porosity, mean particle size, and stratification of particle bed on the quenching process.

Tables 4.5 - 4.6 show the experimental results on quenching rates for the homogeneous particle beds with and without downcomers. Each test series consisted of six experiments with different temperatures of the coolant and the number of downcomers.It can be seen that for the particle beds with relatively large mean particle sizes (series QH-2) the quenching rates are much higher in comparison to those in the the small particle bed (series QH-1) due to the capillarity. In the cases of particulate debris coolability with coolant addition from the bottom (with downcomers), the coolant flow rate in the bed is greatly enhanced by steam formation. It was observed that between the top and bottom addition of water, the bottom water addition dominates the quenching process.

Table 4.7 lists the experimental results for the stratified particle beds. Focus of the experiments is on the effects of particle configurations (such as porosity, mean particle size and the thickness) of the fine particle layer, resting on the top of another layer, on the quenching rate. Six experiments were performed with and without a downcomer and with different coolant temperatures. It was found that cooling times in the series QH-2 and QS-1 are quite close. It may be explained by the fact that the average mean particle diameters were very close: 0.8 and 0.7 mm in these two experiments. In the stratified tests a large enhancement in quenching rate by downcomers was also observed.

In all quenching experiments, described here, the same water overlayer ($\sim$ 0.5 m) was employed.

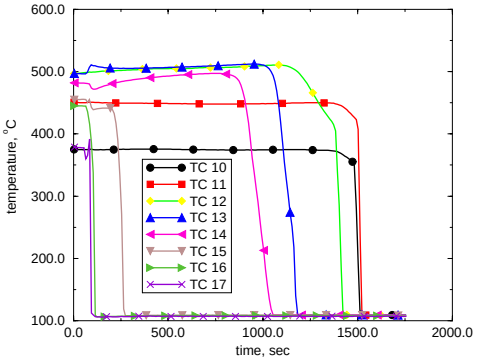

Figure 4.11: Quench front propagation in the test QS-12.

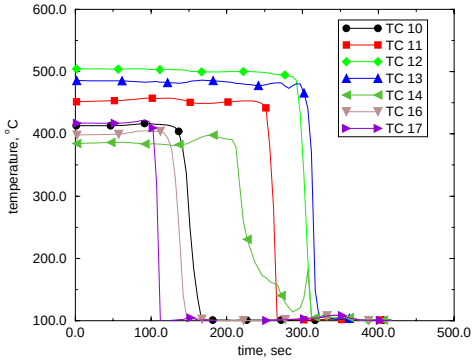

Figure 4.12: Quench front propagation in the test QS-16.

Table 4.5: Experimental results of quenching tests for homogeneous particle bed (porosity - 0.4, mean particle size - 0.2 mm)

Test N	**Dwcm**	**Water temp., ^{o}C**	**Power supply, W**	**Bed temp., ^{o}C**	**Quenching time, sec**	**Average steam discharge flow rate, x10^{-3} kg/s**
QH-1.1	No	20	4600	450	22000	0.08
QH-1.2	No	90	4600	450	9300	0.15
QH-1.3	Yes(1)	20	4600	450	3000	0.55
QH-1.4	Yes(1)	90	4600	450	6000	0.7
QH-1.5	Yes(5)	20	4600	450	200	1.
QH-1.6	Yes(5)	90	4600	450	1200	1.7

Table 4.6: Experimental results of quenching tests for homogeneous particle bed (porosity - 0.26, mean particle size - 0.8 mm)

Test N	**Dwcm**	**Water temp., ^{o}C**	**Power supply, W**	**Bed temp., ^{o}C**	**Quenching time, sec**	**Average steam discharge flow rate, x10^{-3} kg/s**
QH-2.1	No	20	4600	450	2800	0.1
QH-2.2	No	90	4600	450	1650	2.
QH-2.3	Yes(1)	20	4600	450	900	0.7
QH-2.4	Yes(1)	90	4600	450	1200	3.0
QH-2.5	Yes(5)	20	4600	450	200	1.0
QH-2.6	Yes(5)	90	4600	450	700	5.0

From the measured temperature histories at various locations in the particulate layer (see Figures 4.11, 4.12), the quenching time was determined by noting a rapid drop in the particle bed temperature to about the saturation temperature of water at the system pressure. In all these tests, while keeping the mean temperature the same ($\sim 450^o$C), the temperatures in the lower and upper portions of the bed before quenching were slightly less ($\sim 400^o$C) due to the heat loss to the enviroment.

Figure 4.14 shows the quench front histories of the tests QH-11 and QH-12 in comparison to the case of penetration of the water at 20^oC into the bed, heated up to 450^oC without internal heat generation. It was noticed in the all top flooding tests that the almost saturated water penetrates down faster. It can be explained by the fact that the steam dynamic viscosity is much lower than that of water and, hence, due to the Darcy law steam velocity is much higher.

The steam discharge flow rate is plotted as a function of time in Figure **??**. In comparison to the tests with 20^oC coolant, where condensation rate was much more significant, the steam release rates were much higher when 90^oC coolant was employed.

Table 4.7: Experimental results of quenching tests for stratified particle bed (Upper layer (130 mm): porosity - 0.4, mean particle size - 0.2; Lower layer (240 mm): porosity - 0.36, mean particle size - 1 mm)

Test N	Dwcm	Water temp., ^{o}C	Power supply, W	Bed temp., ^{o}C	Quenching time, sec	Average steam discharge flow rate, x10^{-3} kg/s
QS-1.1	No	20	4600	450	1900	1.
QS-1.2	No	90	4600	450	1600	3.
QS-1.3	Yes(1)	20	4600	450	700	5.
QS-1.4	Yes(1)	90	4600	450	1000	6.5
QS-1.5	Yes(5)	20	4600	450	200	10.
QS-1.6	Yes(5)	90	4600	450	350	15.

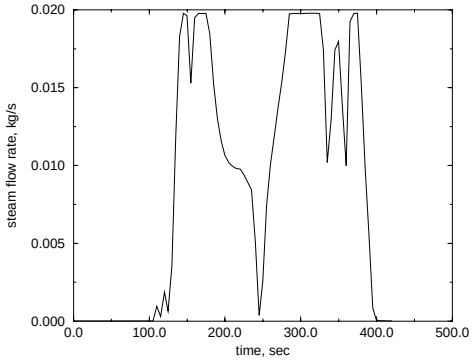

Figure 4.13: Steam discharge flow rate (test QS-16) .

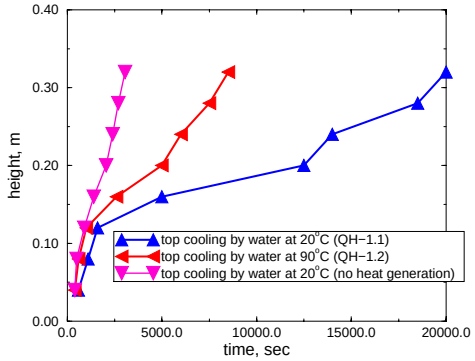

Figure 4.14: Quench front history.

4.4.3 Analysis

A simple zero-dimensional integral analysis has been perfomed based on consideration of hydrodynamic flooding due to steam formation. The analysis applies for both the cases of only top flooding, and of flooding from the top and bottom by the water delivered by downcomers. The basic assumptions are that the penetration of the quench water is uniform across the bed cross section and the steam is generated immediately after contact of water with the solid particles, and the steam heats up the water overlayer. In addition, it is assumed that the hot particles are completely quenched and cooled to water saturation temperature as the water penetrates in the bed. The quenching rate of the bed is directly proportional to the penetration rate. The following relation for the quenching time can be written:

$$\Delta t = \frac{\rho_{sol} C_{p,sol}(1-\epsilon)V(T_{sol} - T_{sat}) + W\Delta t}{G_v H_{fg} - G_w C_{p,w}(T_{sat} - T_w)} \tag{4.25}$$

where Δt is the quench (cooling) time, ρ_{sol} is the solid particle density, $C_{p,sol}$ is the particle specific heat, ϵ is the bed porosity, V is the bed volume, T_{sol} is the initial bed temperature, T_{sat} is the water saturation temperature, W is the power supply, G_v is the steam mass flow rate, H_{fg} is the heat of vaporization of water, G_w is the water mass flow rate, $C_{p,w}$ is the water specific heat and T_w is the initial water (coolant) temperature. The numerator in this ratio is responsible for the total heat, which should be removed toquench the bed, and the denumerator is the quench (cooling) rate. Using the continuity relation between the steam and water mass fluxes we obtain:

$$\Delta t = \frac{\rho_{sol} C_{p,sol}(1-\epsilon)V(T_{sol} - T_{sat})}{G_w(H_{fg} - C_{p,w}(T_{sat} - T_w)) - W} \tag{4.26}$$

First, let us consider water penetration from the top. The water mass flow rate can be calculated as following:

$$G_{w,top} = \rho_w u_w \epsilon A \tag{4.27}$$

where u_w is the velocity of water penetration into the bed, and A is the cross-sectional area of the bed. The velocity can be calculated using the Darcy law:

$$u_w = \frac{K(\epsilon, d_p)}{\mu} \cdot \frac{(p_{over} - p_{cap}(\epsilon, d_p))}{H_{bed}} \tag{4.28}$$

where K is the permeability coefficient, μ is dynamic viscosity, p_{over} is the pressure of water overlayer, p_{cap} is the capillary pressure, and H_{bed} is the bed thickness. In the present work the data given in [93] were employed for an estimation of the permeability coefficient.

For the calculation of the capillary pressure, it is assumed that counter-current annular flow is established in a hypothetical flow channel, described in [94], whose hydraulic diameter d_h is calculated by:

$$d_h = \frac{2}{3} \cdot \frac{\epsilon}{(1-\epsilon)} d_p \tag{4.29}$$

and using Eq. 4.29:

$$p_{cap} = \frac{4\sigma}{d_h} = \frac{6\sigma(1-\epsilon)}{\epsilon d_p} \tag{4.30}$$

where σ is the surface tension. As it can be seen from the Figure 4.15 the capillary pressure affects strongly the system pressure, when particle diameters are less than 0.5 mm. At the bigger particle sizes this influence is not significant.

For the calculation of the water mass flow rate from the bottom. it is necessary to estimate the amount of water per unit time, which can be delivered through the 'hot' downcomers. For the flooding which occurs in an annular counter-current flow of gas and liquid, Wallis [95] provided the correlation:

$$(j_v^*)^{1/2} + (j_w^*)^{1/2} = C_w \tag{4.31}$$

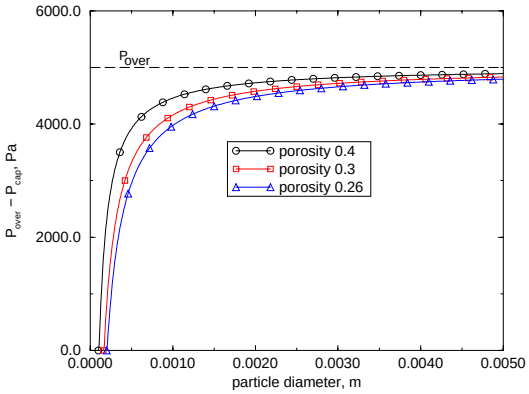

Figure 4.15: Capillarity effect on the system pressure.

where

$$j_v^* = j_v \rho_v^{1/2} / [g(\rho_w - \rho_v)d]^{1/2} \tag{4.32}$$

$$j_w^* = j_w \rho_w^{1/2} / [g(\rho_w - \rho_v)d]^{1/2} \tag{4.33}$$

where j_v and j_w are steam and water velocities, respective, in the tube of diameter d.

The following combined equation for continuty and enrgy holds at the critical heat flux q_c:

$$j_v \rho_v (\pi d^2/4) = j_w \rho_w (\pi d^2/4) = q_c \pi d L / H_{fg} \tag{4.34}$$

where L is the tube length.

In the cases of subcritical heat flux q" and subcooled water not all the liquid is evaporized in the downcomer during the passage, and the water mass

flow rate, which is delivered to the bottom of downcomer, can be calculated as follows:

$$G_{w,tube} = G_{w,init} - \frac{q" \pi d L^*}{H_{fg}} \tag{4.35}$$

where $L^* = L - l_s$ and l_s is the distance, where water becomes saturated.

$$l_s = \frac{j_w \rho_w d C_{p,w} (T_s - T_w)}{4q"} \tag{4.36}$$

where liquid velocity and $G_{w,init}$ can be calculated with the Bernoulli law.

To relate the results of analysis to the experimental data the steam condensation rate in the subcooled water overlayer has to be estimated. In this work correlation given in [96] was used:

$$h = 6.5 \rho_w C_{p,w} u_v^{0.6} (\frac{\nu_w}{D})^{0.4} \tag{4.37}$$

where h is the heat transfer coefficient, u_v is the outlet bed steam velocity, ν_w is the water kinematic viscosity and D is the character diameter of the steam-water inlet area.

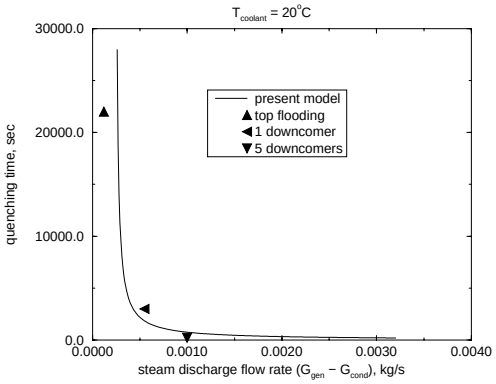

Figure 4.16: Analysis of the tests QH-11, QH-13, QH-15.

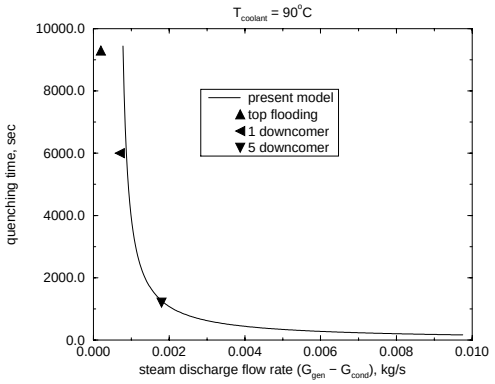

Figure 4.18: Analysis of the tests QH-12, QH-14, QH-16.

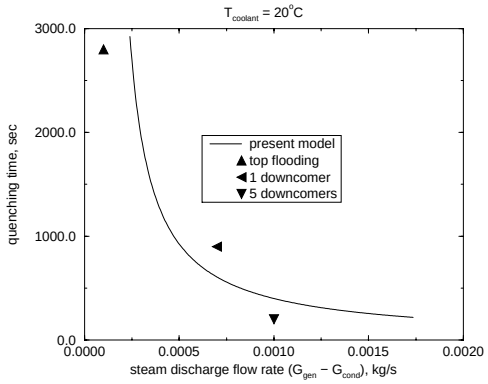

Figure 4.17: Analysis of the tests QH-21, QH-23, QH-25.

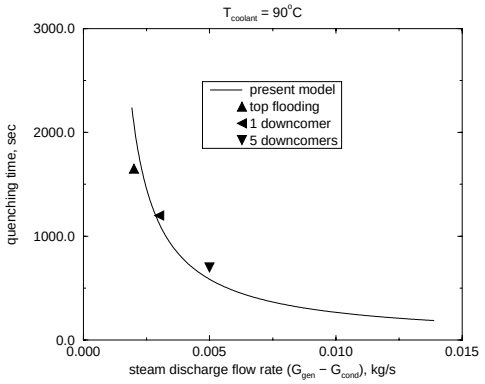

Figure 4.19: Analysis of the tests QH-22, QH-24, QH-26.

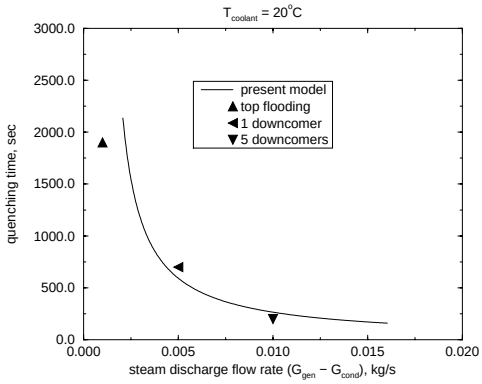

Figure 4.20: Analysis of the tests QS-11, QS-13, QS-15.

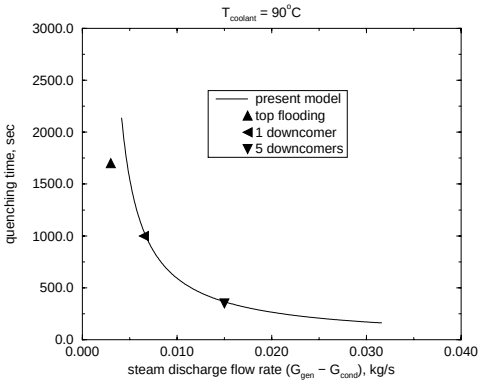

Figure 4.21: Analysis of the tests QS-12, QS-14, QS-16.

Figures 4.16 - 4.21 show the comparison between experimental data, described in previous section, and results of analysis presented above. It is seen that the the quench (cooling) time is an hyperbolic function of the steam mass flow rate, which is generated during the quenching process.

4.5 Summary

The conclusions from POMECO experiments can be formulated as follows:

- Local dryout was observed in all POMECO experiments.
- The measured dryout heat flux for homogeneous particle beds, without downcomers, agrees quite well with predictions by the Lipinski model.
- The downcomers can enhance the dryout heat flux from 50 to 600%. Greater enhancement occurs with larger downcomer flow area.
- Changing the downcomer geometry with no change of the flow area does not change the increase in the dryout heat flux.

A model of steam flowing through a saturated porous medium with internal heat generation was described. Some of POMECO experiments performed

at RIT were analyzed with this model. The calculated results agree with the measurements on dryout location with reasonable accuracy. The dryout is understood to be caused by escalation of heat transfer in local area because of non-linear dependence of thermal conductivity coefficient (with power factor of 0.5) in critical regimes. In reality, the physical situation is much more complicated: two-phase flow in porous media with local phase change, variable boundary conditions depending on flow regimes, etc. Nevertheless, in the heat escalation cases it may be assumed the local steam temperature grows so fast that the dryout position is predetermined by the thermodynamic processes in the steam flow.

The quenching experiments showed that in the tests with only top flooding quenching process was faster when coolant temperature was higher. In the cases of quenching with downcomers, the cooling time was tremendously enhanced. But in these cases quenching by lower temperature coolant was more intesive due to more water per unit time could be delivered through the 'hot' downcomers. It was also observed that during, both, top and bottom addition of water, the bottom quenching dominates the quenching process.

The analysis of the experimental data with integral model, which combines parameters of the process, geometry and physical properties has been performed. Reasonable agreement between experimental and calculated results has been achieved.

Chapter 5

Conclusions

In this chapter, main results of the thesis are summarized. The main objective of the thesis is to improve the understanding of the melt spreading and coolability processes occuring during a postulated severe accident.

In Chapter 2 the various physical phenomena of core melt spreading were considered and studied in depth experimentally and analytically, taking into account the state-of-the-art knowledge base, available experimental observations and data and results of assessments and simulations performed in the past and in other organizations. This was complemented by a considerable data base on spreading that was generated at the Royal Institute of Technology (RIT), Stockholm, with molten simulant materials with a comprehensive variation of the controlling parameter.

Melt spreading with solidification is evaluated by deterministic methods, which are based on an innovative scaling methodology and predictive models developed at RIT. The methodology focuses on the safety relevant characteristics of melt spreading i.e., the average thickness of the spread melt and thereby the spreading length (in 1D) and the spreading area (in 2D). This assessment method, initially proposed for one-dimensional spreading, was extended to describe melt spreading in two-dimensional channels, and then, melt spreading into an open area. Validation of the scaling methodology was performed with the existing database of melt spreading with solidification. The data base gained at RIT and the organizations recently. Both simulant-material and prototypic core melt experiments were analyzed and their data used for validation. Al-

though confirmatory experiments on core melt spreading into open area deem desirable for further validation of the assessment methodology, it is believed that the physics of core melt spreading is reasonably well understood. The spreading characteristics can be predicted by the methods developed and validated at RIT for the purpose of design and assessement written or toilarable level of uncertainty.

Characteristics of core melt spreading in the EPR melt retention device were evaluated for selected core melt accident scenarios, in which melt superheat and melt flow rate as well as melt physical properties have some uncertainties. Based on the results of the assessment performed, it was found that the EPR melt delivery conditions ensure high effectiveness of core melt spreading in the melt retention device as an accident management measure in a hypothetical severe core meltdown situation. For the spread melt thickness of 20 to 35 cm (depending on the amount of concrete slag added), the decay-power generated in the debris layer ($\approx$ 200 kW/m^2) may, then, be removed by an overlying water layer. This leads to the termination of the containment basemat concrete ablation and maintainence of containment integrity during a hypothetical severe accident in the EPR plant.

The melt-crust interactions occuring in an already spread and stopped corium, which can lead to respreading in the event of the failure of the crust have been investigated experimentally and analytically in Chapter 3. Focus was placed on obtaining data on crust re-melting, failure location, failure area development and the resulting re-spreading of molten materials. Debris melt pool formation, natural convection heat transfer inside a melt pool and crust melting are included in consideration. The modeling was performed with MVITA code, which has been applied to study the thermal transients leading to crust melt-through. The debris bed configurations with and without a crust on top surface were considered. The present study indicates that natural convection of the self-heated melt contained within a crust vessel will be the controlling phenomenon for crust re-melting and failure. The failure location will be high along the vertical wall since that is where the natural convection flux peaks. The subsequent erosion of the crust occurs due to the flow of the melt at the failure site, which applies greater heat flux due to the flow motion. These results are in conformity with the observations obtained from TMI-2 accident on the break location of the crust in the in-vessel melt pool, which was immersed in water.

Experimental and analytical investigations of the coolability of heat-generat

ing porous beds has been presented in Chapter 4. A large data base was obtained in the POMECO facility on the dry out heat flux, in homogeneous and stratified debris beds with and without downcomers. A mathematical model for the description of flow of a compressible fluid (steam) through the volumetrically heated porous bed with particular consideration of the local non-thermal equilibrium was formulated and solved numerically using the split step method. It was shown that an initial thermodynamic perturbation which, if it grows, may lead to a temperature escalation at a specific location in a bed, thereby predicting the location of the dry out heat flux. The model was validated against the data obtained from the POMECO facility. Quenching experiments were also performed in the POMECO facility and an integral model was developed as a prediction tool. This model was validated against the data obtained. An innovative aspect of the particulate debris bed dry out and quenching experiments in the POMECO facility was the introduction of downcomers in the bed which enabled the water overlayer to supply water to the bottom of the debris bed where it would flow co-current with the steam produced. It was found that the provision of downcomers enhanced the magnitude of the dry out heat flux several times and increased the bed quench rate by one to two orders of magnitude.

In general, the work described in this thesis helps to advance the current understanding about the complex phenomenology associated with ex-vessel melt accident progression during a severe accident scenario in nuclear power plants. Insights into the processes of melt spreading, re-spreading and debris coolability have been gained by means of experiments, and phenomenological and mechanistic modeling. Phenomenological modeling has been employed as an effective tool to perform safety assessment, which helps to resolve different scenario and phenomenological uncertainties, whereas mechanistics modeling has been used to gain insight into a particular physical phenomenon.

Bibliography

[1] Theerthan, A., Karbojian., A., and Sehgal, B.R., ”EC-FOREVER Experiments on Thermal and Mechanical Behavior of a Reactor Pressure Vessel During a Severe Accident’, Technical report-1, KTH, Stockholm, Sweden, (2000).

[2] Theofanous, T.G. and H. Yan, ”The Probability of Liner Failure in a Mark-I Containment, Parts I-III. Part II: Melt Release and Spreading Phenomena,” Nuclear Technology, Vol. 101, pp. 299-384, (1993).

[3] Theofanous, T.G., ”On the Proper Formulation of Safety Goals and Assessment of Safety Margins for Rare and High-Consequence Hazards”, Reliability Engineering and Systems Safety, Vol.54, pp.243-257 (1996).

[4] Sehgal, B.R., Bui, V.A., Dinh, T.N., and Nourgaliev, R.R.,”Treatment of Phenomenological Uncertainties in a LWR Severe Accident Risk Analysis Computer Code”, International Conference on ”Probabilistic Safety Assessment and Management - PSAM-4”, Sep. 13-18, 1998 - New York City, USA.

[5] Sehgal, B.R., Dinh, T.N., Green, J.A., Konovalikhin, M.J., Paladino, D., Leung, W.H., Gubaidulin, A.A., ”Experimental Investigation of Melt Spreading in One-Dimensional Channel”, RIT/NPS Research Report for European Union EU-CSC-1D1-97, 86p., 1997.

[6] Dinh, T.N., Konovalikhin, M.J., Green, J.A., Paladino, D., Gubaidulin, A.A., and Sehgal, B.R., ”Experimental Simulation of Core Melt Spreading on a LWR Containment Floor in a Severe Accident”, CD-ROM Proceedings International Conference on Nuclear Engineering, ICONE-6, San Diego, CA, USA, May, (1998).

[7] Leger, L. and J.F. Joanny, ”Liquid Spreading,” Reports on Progress in Physics, Vol. 55, No. 4, pp.431-486, (1992).

[8] Shikhmurzaev, Y.D., ”Spreading Flow of a Viscous Liquid Over a Solid Surface,” Soviet Physics Doklady, Vol. 36, No. 11, pp. 749-752, (1991).

[9] Kalliadasis, S. and H.C. Chang, ”Dynamics of Liquid Spreading on Solid Surfaces,” Ind. Eng. Chem. Res., Vol. 35, pp. 2860-2874, (1996).

[10] Rahman, M.M., W.L. Hankey and A. Faghri, ”Analysis of the Fluid Flow and Heat Transfer in a Thin Liquid Film in the Presence and Absence of Gravity,” Int. Journal of Heat Mass Transfer, Vol. 34. No. 1, pp. 103-114, (1991).

[11] Weisshäupl, H.A. and D. Bittermann, ”Large Spreading of Core Melt for Melt Retention-Stabilization,” Nuclear Engineering and Design, Vol. 157, pp. 447-454, (1995).

[12] Alsmeyer H., et al., ”Overview on the Results of the RCA Project on Molten Core - Concrete Interactions”, FISA-95 Proceedings, Luxemburg EUR 16896 EN, pp.231-255 (1996).

[13] Cognet, G., J.M. Veteau, P. Eberle and J.M. Seiler, ”French Research Programme on Spreading-Based Core Catcher Designs,” Proceedings of the Fifth International Topical Meeting on Nuclear Thermal Hydraulics, Operations and Safety (NUTHOS-5), Beijing, China, pp. V5:1-6, (April, 1997).

[14] G. Cognet, Vulcano Experiments on Melt Spreading. CSC Project Report, 1998; and VULCANO VE-U3 Experiment, Information Letter, 1998.

[15] Ehrhard, P. ”Spreading of Melts in the Presence of Solidification,” International Conference on Nuclear Engineering (ICONE-4), Vol. 1B, pp. 935-941, (1996).

[16] Greene, G.A., C. Finrock, J. Klages, and C.E. Schwarz, ”Experimental Studies on Melt Spreading, Bubbling Heat Transfer and Coolant Layer Boiling,” Proceedings of 16^{th} Water Reactor Safety Meeting, NUREG/CP-0096, pp.341-358, (1988).

[17] F.J. Moody, ”First Order Analyses of Molten Corium Heat Transfer”, ANS Proceedings of 1989 National Heat Transfer Conference, Philadelphia, pp.217-224, 1989.

[18] Fink, J.H. and R.W. Griffiths, ”Radial Spreading of Viscous-Gravity Currents with Solidifying Crusts,”, Journal of Fluid Mechanics, Vol. 221, pp. 485-509, (1990).

[19] Griffiths, R.W. and J.H. Fink, ”Effects of Surface Cooling on the Spreading of Lava Flows and Domes,” Journal of Fluid Mechanics, Vol. 252, pp. 667-702,(1993).

[20] Suzuki, H., et al., ”Fundamental Experiment and Analysis for Melt Spreading on Concrete Floor,” Proceedings of 2^{nd} ASME/JSME Nuclear Engineering Conference, Vol. 1, pp. 403-407, (1993).

[21] Veteau, J.M., ”CORINE Program,” OECD/CSNI/NEA Workshop on Large Molten Pool Heat Transfer, pp. 531-548, (1994).

[22] Cognet, G. and J.C. Bouchter, ”VULCANO: A Large Scale UO_2 Program to Study Corium Behavior and Cooling for Future Reactors,” OECD/CSNI/NEA Workshop on Large Molten Pool Heat Transfer, pp. 521-529, (1994).

[23] Fieg, G., et al., ”Simulation Experiments on the Spreading Behavior of Molten Core Debris”, Proceedings of the 1996 National Heat Transfer Conference, in the session ”Fundamental Phenomena in Severe Accidents”, Houston, Texas, August 3-6, 1996, HTC-Vol.9, pp.121-129.

[24] Steinwarz, W., ”Investigation on the Phenomenology of Ex-Vessel Core Melt Behavior”, Presented to Joint INV/EXV Clusters Meeting, Roma, 1997.

[25] Magallon, D., ”FARO Spreading Test LS-26”, CSC Project Internal Communication, 1997.

[26] Farmer, M.T., J.J. Sienicki, C.C. Chu, and B.W. Spencer, ”The MELTSPREAD-1 Computer Code for the Analysis of Transient Spreading and Cooling of High-Temperature Melts,” ANL, (1993).

[27] LAVA - A Computer Code for Simulation of Lava Flows. GRS, Köln, Germany, 1997.

[28] Veteau, J.M. and Wittmaack R., ”CORINE Experiments and Theoretical Modeling”, FISA-95 Proceedings, Luxemburg EUR 16896 EN, pp.271-285 (1996).

[29] MECO Code for Melt Spreading and Coolability Modeling. Ruhr University. Bochum, 1997.

[30] Popkov, A.G., V.V. Chudanov, V.F. Strizhov, P.N. Vabishchevich, J.C. Latche and J.M. Veteau, ”Validation of Hydrodynamic Models of the RASPLAV/SPREAD Code Against the CORINE Experiments,” Heat and Mass Transfer in Severe Nuclear Reactor Accidents, Turkey, (1994).

[31] CROCO Code for Melt Spreading Simulation. ISPN, Cadarache, France, 1997.

[32] Huppert, H.E., ”The Propagation of Two- Dimensional and Axisymmetric Viscous Gravity Currents Over a Rigid Horizontal Surface”, Journal of Fluid Mechanics, Vol. 121, pp. 43-58, (1982).

[33] Kazimi, M.S., ”On the Liner Failure Potential in MARK-I Boiling Water Reactors”, Nucl.Sci. Eng., Vol.103, 59 (1989).

[34] Scholtyssek, W., H. Alsmeyer, and H. Werle, ”Recent Results of Melt Spreading and Cooling Experiments at FZK - The KATS and COMET Projects,” CSARP-96, Bethesda, MD, (1996).

[35] Fieg, G., et al. PSF News, FZK Quick Look Reports from Internet, http://psf-nt-server.fzk.de/psfhome.htm, 1997.

[36] Moraga, F., R.T. Lahey and M.Z. Podowski, ”Experimental Simulation of the Water Cooling of Corium Spread Over the Floor of a BWR Containment,” Proceedings of NURETH-7, Saratoga Springs, N.Y., pp. 1930-1948, (1995).

[37] Cognet, G. ”Main Results of the COMAS-5a Benchmark (CROCO, THEMA, MELTSPREAD, LAVA, CORFLOW, MECO Codes)”, Presented to CSC Project Meeting, Cadarache, June 1997.

[38] Bolshov L.A., et al., ”Numerical Models of Molten Core Spreading Processes in Nuclear Reactor Safety Problems”, Proceeding of the 4th International Topical Meeting on Nuclear Thermal Hydraulics, Operations and Safety, April 1994, Taipei, Taiwan.

[39] Wittmaack, R., ”CORFLOW, a Computer Program for the Numerical Simulation of Free Surface Flow”, J. Nuclear Technology, 1997 (Siemens KWU NA-M/96/E041, 1996).

[40] Sakimoto, S.E., and Zuber, M.T., ”The Spreading of variable-Viscosity Axisymmetric Radial Gravity Currents: Applications to the Emplacement of venusian ’pancake’ domes”, J. Fluid Mechanics, Vol. 301, pp.65-77, 1995.

[41] Foit, J.J., ”Spreading with Variable Viscosity”, Forschungszentrum Karlsruhe, FZKA 6006, 15p, 1997

[42] No, H.C. and Ishii, M., ”Scaling Studies on Spreading of Molten Corium in Mark-1 Boiling Water Reactors”, ANS Meeting, 1991.

[43] Morris, S., ”Report on FARO Spreading Test L-26”, EU JRC, Ispra, presented to FARO Experts Group and CSC Project Meetings, Dec. 1997.

[44] Wider, H.U., ”Pre-Test Calculations with the CORFLOW Code for the First UO_2/ZrO_2 Spreading Test in FARO”, EU JRC Internal Report, 1997, presented to CSC project meeting, Dec. 1997.

[45] Moody, F.J., Fruth, K.M., Muralidharan, R., ”Parameter Effects on MOlten Debris Spreading and Coolability”, Proceedings of the Nineteenth Water Reactor Safety Information Meeting, Vol.6, pp.241-263, (1991).

[46] Theofanous, T.G., et al., ”The Probability of Liner Failure in a Mark I Containment”, NUREG/CR-5423, 1989.

[47] Kymälämen, O., Bongisto, O., Antman, J., tuomisto, H., and Theofanous, T.G.,”COPO Experiments for Heat Flux Distribution from a Volumetrically Heated Corium Pool”, Proceedings of the 20-th Water Reactor Safety Information Meeting, Bethesda, Maryland, October 21-23, 1992.

[48] Theofanous, T.G., Lin, C., Additon, S., Angelini, S., Kymälämen, O., Salmassi, T.,”In-Vessel Coolability and Retention of a Core Melt”, DOE Report DOE/ID-10460, v.1&2, 1996.

[49] Bonnet, J.M., Ronge, S., and Seiler, J.M.,”Large Scale Experiments for Core Melt Retention”, Proceedings of the OECD/CSNI/NEA Workshop on Large Molten Pool Heat Transfer, Grenoble, France, March 9-11, 1994, 1994.

[50] Strizhov, V.,”OECD RASPLAV Project”, Proceedings of the OECD/CSNI/NEA Workshop on Large Molten Pool Heat Transfer, Grenoble, France, March 9-11, 1994, pp. 445-468, 1994.

[51] Sehgal, B.R., Bui V.A., Dinh T.N. and Nourgaliev R.R., ”Heat Transfer Processes in Reactor Vessel Lower Plenum during a Late Phase of In-Vessel Core Melt Progression”, J. Advances in Nuclear Science and Technology, Plenum Publ. Corp., 1998.

[52] Turland B.D.,"In-vessel Phenomena Relevant to the Achievement of Debris Coolability By Ex-Vessel Flooding of a PWR", Proceedings of the OECD/CSNI/NEA Workshop on Large Molten Pool Heat Transfer, Grenoble, France, March 9-11, 1994.

[53] Fischer, M.,"Main Conceptual Features of the EPR Melt Retention Concept", OECD Workshop on Ex-Vessel Debris Coolability Karlsruhe, Germany, 16-18 November, (1999).

[54] Alsmeyer, H., "BETA Experiments on Zirconium Oxidation and Aerosol Release during Melt-Concrete Interactions", Proceedings of the Second OECD (NEA), CSNI Specialist Meeting on Molten Core Debris-Concrete Interactions , Karlsruhe, KFK 5108 (NEA/CSNI/R (92)), 1992.

[55] Alsmeyer, H., Review on Experiments on Dry Corium Concrete Interaction in: Molten Corium/Concrete Interaction and Corium Coolability - A State of the Aet Report - Directoriate-General XII Science, Research and Development, EUR 16649EN.

[56] Beckermann, C., "Modeling of Transport Phenomena in mushy zones", Modeling of casting, Welding, and Advanced solidifica tion processes VI, Ed. T.S. Piwonka *et. al.*, The minerals, Metals & Materials Society ©1993.

[57] Bui V.A., Dinh T.N. and Sehgal, B.R., "In-Vessel Core Melt Pool Formation during Severe Accidents", Proc. National Heat Transfer Conference, Houston, Texas, HTC-Vol.9, 1996.

[58] Chiareli, A.O.P., Huppert, H.E., Worster, M.G., "Segregation and flow during the solidification of alloys", Journal of Crystal Growth, 139, pp. 134-146, 1994.

[59] Cognet, G., et al., "Corium Spreading and Coolability (CSC Project)", FISA-97, Luxembourg, November, 1997.

[60] Copus, E.R., "Sustained Uranium Dioxide/Concrete Interactions Tests: The SURG Test Series", Proceedings of the Second OECD (NEA), CSNI Specialist Meeting on Molten Core Debris-Concrete Interactions , Karlsruhe, KFK 5108 (NEA/CSNI/R (92)), 1992.

[61] Thompson, D.H., Fink, J.K., Armstrong, D.R., Spencer, B.W., and Sehgal, B.R., "Thermo=-Hydraulic Aspects of the Large-Scale Integral MCCI Tests

in the ACE Program", Proceedings of the Second OECD (NEA), CSNI Specialist Meeting on Molten Core Debris-Concrete Interactions , Karlsruhe, KFK 5108 (NEA/CSNI/R (92)), 1992.

[62] Worster, M.G., "Convection in Mushy Layers", Annu. Rev. Fluid Mech. 29, pp. 91-122, 1997.

[63] Magalon, D., et al., "The FARO Programme Recent Results and Synthesis", CSARP Meeting, USA, Bethesda, Maryland, May, 1997.

[64] Choudhary, M.V., and El-Wakil, N.M.,"Heat transfer and flow characteristics in conductive porous media with energy generation", Proc. Int. Heat Transfer Conf., Versailles, France, 1970.

[65] Dhir, V., Catton, I., "Dryout Heat Fluxes for Inductively Heated Particulate Beds", J. of Heat Transfer, Vol. 99, May, 1977.

[66] Vasiliev, L.L. and Mairov, V.A., "An Analytical Study of Resistance, Heat Transfer and Stability in Evaporative Cooling of a Porous Heat Producting Element", Int. J. Heat Mass Transfer, 12, 301-307, 1979.

[67] Naik, A.S. and Dhir, V.K. "Forced Flow Evaporative Cooling of a Volumetrically Heated Porous Layer", Int. J. Heat Mass Transfer, Vol. 25, No. 4, pp. 541-552, 1982.

[68] Hofmann, G. "On the Location and Mechanisms of Dryout in Top-Fed and Bottom-Fed Particulate Beds", Nuclear Technology, Vol. 65, 1984.

[69] Schulenberg, T. and Muller, U. "A Refined Model for the Coolability of Core Debris with Flow Entry from the Bottom", Presented at the 6th Information Exchange Meeting on Debris Coolability, Univ. of California, Los-Angeles, 1984.

[70] Tsai, F.P., "Dryout heat flux in a volumetrically heated porous bed", Ph.D. Dissertation, Univ. of California, Los Angeles, 1987.

[71] Tung, V.X., and Dhir, V.K., "A Hydrodynamic Model for Two-Phase Flow Through Porous Media", Int. J. Multiphase Flow, Vol. 14, No. 1, pp. 47-65, 1988.

[72] Tung, V.X., and Dhir, V.K., "Finite Element Solution of Multi-Dimensional Two-Phase Flow Through Porous Media with Arbitrary Heating Conditions", Int. J. Multiphase Flow, Vol. 16, No. 6, pp. 985-1002, 1990.

[73] Lipinski, R.J., ”A Model for Boiling and Dryout in Particle Beds”, Sandia Labs, SAND 82-9765, NUREG/CR-2646, 1982.

[74] Lipinski, R.J., ”A Coolability Modal for Post Accident Nuclear Reactor Debris”, Nuclear Technology, Vol. 65, pp. 53-66, 1984.

[75] Stubos, A.K., and Buchlin, J.-M., ”Modeling of Vapor Channeling Behavior in Liquid-Saturated Debris Bed”, Transactions of the ASME, Vol. 110, November, 1988.

[76] Stubos, A.K., and Buchlin, J.-M., ”Vapor Channels in Boiling, Unconstricted Particle Beds - Effect on the Dryout Heat Flux”, Int. J. Multiphase Flow, Vol. 20, No. 1, pp. 131-152, 1994.

[77] Stubos, A.K., and Buchlin, J.-M., ”Analysis and Numerical Simulation of the Thermohydraulic Behavior of a Heat Dissipating Debris Bed During Power Transients”, Int. J. Heat Mass Transfer, Vol. 36, No. 5, pp. 1391-1401, 1993.

[78] Sözen, M., and Vafai, K., ”Analysis of the Non-Thermal Equilibrium Condensing Flow of a Gas Through a Packed Bed”, Int. J. Heat Mass Transfer, Vol. 33, No. 6, pp. 1247-1261, 1990.

[79] Kuznetsov, A.V., ”An Investigation of a Wave of Temperature Difference Between Solid and Fluid Phases in a Porous Packed Bed”, Int. J. Heat Mass Transfer, Vol. 37, No. 18, pp. 3030-3033, 1994.

[80] Kuznetsov, A.V., ”Investigation of Multi-Dimensional Effects During Heating a Porous Packed Bed”. 2nd European Thermal-Sciences and 14th UIT National Heat Transfer Conference, 1996.

[81] Konovalikhin, M.J., Yang, Z.L., Amjad, M., and Sehgal, B.R., ”On Dryout Heat Flux of s Particle Debris Bed with a Downcomer”, ICONE-8, Baltimore, USA, April, 2000.

[82] Alsmeyer, H., Spencer, B., and Tromm, W., ”The COMET concept for Cooling of Ex-Vessel Corium Melts”, ICONE-6, USA, San Diego, 1998.

[83] Becker, M., Engström , J., and Macbeth, R.V., ”Enhancement of Core Debris Coolability”, TIT-Report: KTH-NEL-51, 1990.

[84] Nigmatulin, R.I. ”The Base of Mechanics of Heterogeneous Medias”, ”Nauka”, Russia, Moscow, 1978 (in russian).

[85] Kazachkov, I.V. ”On the Mathematical Simulation of Processes of Nonstationary Nonisothermal Filtration in Geothermal Systems”, J. Numerical and Applied Mathematics, vol. 60, Kiev State University, 1986 (in russian).

[86] Samarsky, A.A., et. al.,”Regimes With Peaks in the Problem for Quasilinear Parabolic Equations”, ”Nauka”, Russia, Moscow, 1987 (in russian).

[87] Janenko, N.N., ”The Split Step Method for Solution of the Multidimensional Problems of Mathematical Physics”, ”Nauka”, Russia, Novosibirsk, 1967 (in russian).

[88] Cho, D.H., and Bova, L., ”Formation of Dry Pockets During Water Penetration into a Hot Particle Bed”, Trans. ANS, Vol. 41, 1983.

[89] Ginsberg, T., Klein, J., Klages, J., Schwarz, C.E. and Chen, J.C., ”Transient Core Debris Heat Removal Experiments and Analysis”, presented at the International Meeting on Thermal Nuclear Reactor Safety, Chicago, Illinois, 1982.

[90] Tung, V.X., Dhir, V.K., and Squarer, D., ”Quenching by Top Flooding of a Heat Generating Particulate Bed With Gas Injection at the Bottom”, Proc. of the 6th Information Exchange Meeting on Debris Coolability, 1986.

[91] Hall, P.C., and Hall, C.M., ”Quenching of a Hot Particulate Bed by Bottom Flooding: Preliminary Results and Analysis”, presented at the European Two-Phase Flow Group Meeting, Eindhoven, Holland, 1981.

[92] Tung, V.X., and Dhir, V.K., ”Quenching of a Hot Particulate Bed by a Bottom Flooding”, Proc. ASME-JSME Thermal Engineering Joint Conference Honolulu, Hawai, 1983.

[93] Brooks, R.H., and Corey, A.T., ”Properties of Porous Media Affecting Fluid Flow”, J. of the Irrigation and Draining Division, Vol. 92, No. IR2, June, 1966.

[94] Abe, Y., ”Applicability of Annular Flow Model to Counter-Current Flow in Debris Bed”, J. of Nuclear Science and Technology, Vol. 32, No. 8, pp. 763-772, August, 1995.

[95] Wallis, G.B., ”One-dimensional Two-phase Flow”, McGraw-Hill, Inc., USA, 1969.

[96] Aya, I., and Nariai, H., ”Evaluation of Heat-transfer Coefficient at Direct-contact Condensation of Cold water and Steam”, Nuclear Engineering and Design, 131, pp. 17-24, 1991.